

Louisiana Tech University

Louisiana Tech Digital Commons

Doctoral Dissertations

Graduate School

Spring 5-2023

Clay Nanotube Drug Carrier with Enhanced Membrane/Skin Permeability

Mahdi Saleh

Follow this and additional works at: <https://digitalcommons.latech.edu/dissertations>

**CLAY NANOTUBE DRUG CARRIER WITH ENHANCED
MEMBRANE / SKIN PERMEABILITY**

by

Mahdi Saleh, B.Sc.

A Dissertation Presented in Partial Fulfillment
of the Requirements for the Degree
Doctor of Philosophy

COLLEGE OF ENGINEERING AND SCIENCE
LOUISIANA TECH UNIVERSITY

May 2023

LOUISIANA TECH UNIVERSITY

GRADUATE SCHOOL

March 13, 2023

Date of dissertation defense

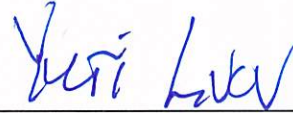
We hereby recommend that the dissertation prepared by

Mahdi Saleh, B.Sc.

entitled **Clay Nanotube Drug Carrier with Enhanced Membrane/Skin
Permeability**

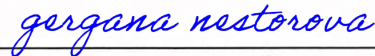
be accepted in partial fulfillment of the requirements for the degree of

Doctor of Philosophy in Molecular Sciences and Nanotechnology



Yuri Lvov

Supervisor of Dissertation Research



Gergana Nestorova

Head of Molecular Sciences and Nanotechnology

Doctoral Committee Members:

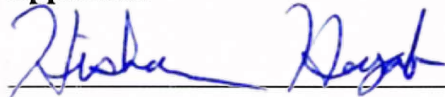
Mark DeCoster

Gergana Nestorova

Shaurav Alam

Randy Null

Approved:



Hisham Hegab

Dean of Engineering & Science

Approved:



Ramu Ramachandran

Dean of the Graduate School

ABSTRACT

Halloysite nanoclay is a natural material which is interesting for biomedical applications. Its unique physiochemical structure that forms the tubular shape originates from rolled sheets of aluminosilicate 15-20 times, such that alumina is inside and silica on the outside of the nanotubes, thus defining inner positive and outer negative charges. The dimensions of these tubules vary from 500-1,000 nm in length, external diameter 50-60nm, and inner lumen 12-15nm. Halloysites are biocompatible, cheap, and available in large quantities which suggests that these tubules can be used as effective nanocarriers. In this work, we exploited halloysite as a “nano-torpedo” for targeted drug delivery through the membranes in two ways. We discovered new “larger” nanotubes of 80 nm diameter and 1.6 μm length and used them for skin protection with in depth halloysite drug delivery. In the second part of the work, the use of traditional “smaller” halloysite as a carrier for drug delivery through the blood-brain barrier was developed, both *in vitro* and *in vivo*. In this work, we made all drug nanoformulations, and collaborate with Dr. DeCoster lab and Dr. Murray lab in cell and mice experiments.

We invented “new” larger halloysite nanotubes and utilized their potential for skin care applications. Analyzing the structure of the halloysite nanotubes provided by NorthStar LLC., we found an increase in dimensions when compared to traditional halloysite. The larger tubes have a length of 1.6 μm and a diameter of 80 nm. Visualization of halloysite dispersibility in water was possible with these larger

tubules confirming favorable aqueous dispersibility and structural organization are comparable traditional smaller halloysite. We suggested that the larger tubes formation mechanism could be similar to smaller halloysite (rolling), but initial aluminosilicate sheets were of larger area, thus forming larger tubes. We theorized that these “new” nanotubes would be more efficient in penetration through strong barriers, like skin, for drug delivery due to their size and increased drug loading capacity. Encapsulating vitamin B-12, a known skin protecting agent inside these nanotubes create a new formulation with sustained B-12 release when admixed to traditional oil-based skin cream. Pig skin was used for initial testing and analysis due to it consisting of a similar epidermis to human skin. Initial results were promising with massaging of such a formulation on skin which provides perpendicular penetration of the halloysite nanotubes.

Additionally, we found that for penetration through cell membranes around the brain, smaller halloysite formulations could be more effective. Current treatments for brain disorders such as epilepsy are not effective due to the selectivity of the blood-brain barrier (BBB) preventing drug delivery. Utilizing traditional small halloysite with dimensions of 500-800 nm in length and external diameter of 50-60 nm and inner lumen 12-15 nm, we conducted *in vitro* experiments of halloysite formulations as a “nano-torpedo” penetrating brain microvascular endothelial cell (BMVECs). Through fluorescent and real time calcium imaging techniques we proved a prolonged gradual drug delivery mechanism by the encapsulation of rhodamine isothiocyanate and ionomycin within the nanotube. With delayed diffusion, the nanotubes effectively delivered the drug to the primary BMVECs without causing any toxic effects or killing them, by binding and penetration in time periods of 1 to 24 h.

Furthermore, constructing a two layer (astrocytes and endothelial) synthetic blood-brain model barrier with a 0.4 μm porous transwell support enabling us to study structures closer to the BBB. The confluence of the bilayer of astrocyte and endothelial cells was examined using a non-inverted microscope after Diff-Quik staining of the cells. The halloysite rhodamine formulations were tested on this barrier by treating the samples to the dual layer of endothelial / astrocyte cells and allowing them to pass through the barrier on their own. Proving its penetration by measuring the fluorescence at the bottom of the membrane after 24 h. The fluorescence signal grew moderately in the first hour but by 24 h it had increased to 85 %.

In the last section of this work, *in vivo* experiments on halloysite delivery to the brains of mice via intranasal administration were conducted in collaboration with Y. Yanamadala. Halloysite formulations with encapsulation of rhodamine isothiocyanate to track halloysite as it moves throughout the brain were developed. We produced the nanoclay loading of diazepam and xylazine which are two commonly used drugs for their anxiolytic and sedation effects. Wild type C57BL/6NHsd were purchased from Jackson Laboratory and these three halloysite formulations were intranasally delivered to mice. Analysis of the olfactory bulb and cortex were accomplished through multiple microscopy techniques and the overall condition of the mice were measured by behavioral studies such as rotarod, novel object recognition, and open field tests over the course of seven days. In this collaborative work we proved not only delivery of halloysite to the brain by passing the blood-brain barrier, but also have shown that its presence in the brain was not harmful to the behavior or well-being of the mice. Therefore, potentially, such halloysite-drug delivery may be used for urgent brain disease treatment with deposition / of this biocompatible nanoclay residues.

APPROVAL FOR SCHOLARLY DISSEMINATION

The author grants to the Prescott Memorial Library of Louisiana Tech University the right to reproduce, by appropriate methods, upon request, any or all portions of this Dissertation. It is understood that “proper request” consists of the agreement, on the part of the requesting party, that said reproduction is for his personal use and that subsequent reproduction will not occur without written approval of the author of this Dissertation. Further, any portions of the Dissertation used in books, papers, and other works must be appropriately referenced to this Dissertation.

Finally, the author of this Dissertation reserves the right to publish freely, in the literature, at any time, any or all portions of this Dissertation.

Author _____

Date _____

DEDICATION

This dissertation is dedicated to my family who have supported me continuously throughout my education.

TABLE OF CONTENTS

ABSTRACT.....	iii
APPROVAL FOR SCHOLARLY DISSEMINATION	vi
DEDICATION	vii
LIST OF FIGURES	xiii
ACKNOWLEDGMENTS	xx
CHAPTER 1 INTRODUCTION	1
CHAPTER 2 LITERATURE REVIEW	6
2.1 Halloysite Nanotube.....	6
2.1.1 Physiochemical Characteristics	6
2.2 Loading and Release Strategies	10
2.2.1 Lumen Loading and Modifications.....	10
2.2.2 Physical Absorption and Electrostatic Enhancement (inside and outside)...	12
2.2.3 Tube’s Surface Modification	13
2.3 Halloysite Antiseptics Applications.....	15
2.4 Halloysite Diagnostic Applications	16
2.4.1 Bioimaging.....	16
2.5 Halloysite Applications in Therapy	18
2.5.1 Drug Therapy	18
2.5.1.1 Anticancer Drugs	18

2.5.1.2 Cardiovascular Drugs.....	21
2.5.1.3 Anti-Inflammatory and Analgesic Drugs.....	22
2.5.1.4 Biopharmaceutical Agents	22
2.5.1.5 Natural Compounds – Vitamins.....	28
2.6 Toxicity and Nanosafety	31
2.7 Blood Brain Barrier.....	32
2.7.1 Structure and Physiology	33
2.7.2 Nanotechnology and the Blood-Brain Barrier	35
2.8 Conclusions.....	35
CHAPTER 3 INSTRUMENTATION	37
3.1 Zeta-Potential Analyzer	37
3.2 Scanning Electron Microscope	38
3.3 Thermogravimetric Analysis	38
3.4 Atomic Force Microscope.....	39
3.5 Nikon A1R Confocal & Super Resolution System.....	40
3.6 Transmission Electron Microscope (TEM) Philips CM 200 FEG.....	41
3.7 Dark-Field Microscopy	42
3.8 Leica DMI 600B Inverted Microscope	43
3.9 Contact Angle Instrument.....	44
3.10 X-ray Diffractometer	45
3.11 Other Supporting Instruments.....	46
CHAPTER 4 SELECTION AND OPTIMIZATION OF THE CLAY NANOTUBE SIZES	47
4.1 “Larger” Halloysite Nanotubes.....	47

4.2 Structural Characterization of Traditional “Smaller” Halloysite Nanotubes.....	52
4.3 Selection of Larger Halloysite for Skin Application	56
4.3.1 Halloysite and Vitamin B-12	57
4.3.2 Vitamin B-12 Encapsulation.....	59
4.3.3 HNT-B12 and Pig Skin Treatment	61
4.4 Conclusions.....	62
CHAPTER 5 TAGGED HALLOYSITE NANOTUBES AS A CARRIER	64
5.1 Tagged Halloysite Nanotubes as a Carrier for Intercellular Delivery in Brain Microvascular Endothelium and Model Two-Cell Brain Blood Barrier (Nano-Torpedo Approach)	64
5.2 Preview	64
5.2.1 Halloysite Loading with Rhodamine Isothiocyanate Dye, and Ionomycin, and Neurotransmitters.....	68
5.2.2 Cell Culture.....	69
5.2.3 Treatment with Rhodamine Isothiocyanate (RITC) Loaded Halloysites	70
5.2.4 Brain Microvascular Endothelial Cells (BMVECs) Stimulation Using Ionomycin Loaded Halloysite.....	71
5.2.5 Development of the in vitro Co-Culture Model on Transmembrane.....	71
5.2.6 Visualization of HNT-RITC Uptake and Diffusion Across the Two-cells Barrier	72
5.2.7 MTT Assay	72
5.2.8 Halloysite Release Profile.....	73
5.2.9 Intracellular Rhodamine Isothiocyanate (RITC) Delivery with Clay Nanotubes	74
5.2.10 Halloysite Loading with Rhodamine Isothiocyanate Dye, and Ionomycin	77

5.2.11 Delivery of Ionomycin – Halloysite Formulations into Endothelial Cells (Ca ²⁺ -Analysis).....	79
5.2.12 Statistical Analysis of Calcium Response to Different Stimuli.....	81
5.2.13 Co-culture Studies of Blood–Brain Barrier	85
5.2.14 Passage of RITC through the Co-culture Model.....	86
5.3 Conclusions.....	88
CHAPTER 6 DIAZEPAM AND XZYLAZINE LOADED CLAY NANOTUBES	89
6.1 Diazepam and Xzylazine Loaded Clay Nanotubes Permeate the Brain Through Intranasal Administration and Shows No Behavioral Changes in Mice	89
6.2 Preview	90
6.2.1 Preparation of HNT’s with RITC, Diazepam, and Xylazin.....	92
6.2.2 Animal Care and Handling	93
6.2.3 Intranasal/Introperitoneal Administration.....	93
6.3 Neuro-Behavioral Tests	94
6.3.1 Rotarod Test.....	94
6.3.2 Modified Neurological Severity Score (mNSS)	95
6.3.3 Open Field (OF).....	95
6.3.4 Novel Object Recognition.....	96
6.3.5 Behavioral Video Analysis (MATLAB).....	97
6.4 Brain Removal and Imaging	98
6.4.1 Perfusion and Extraction of Brain.....	98
6.4.2 Vibratome Sectioning	99
6.4.3 Preparation of Samples for Imaging	99
6.4.4 Imaging	99

6.5 Halloysite Drug Loading and Delivery.....	100
6.5.1 Thermogravimetric Analysis and Release Profile of RITC.....	100
6.5.2 Intranasal and Intraperitoneal Delivery of HNT + RITC to the Olfactory Bulb and Cortex.....	102
6.6 Behavioral Studies	105
6.6.1 Rotarod Score.....	105
6.6.2 Modified Neurological Severity Score Results.....	107
6.7 Discussion.....	108
6.8 Conclusion	110
CHAPTER 7 CONCLUSIONS	112
REFERENCES	115

LIST OF FIGURES

Figure 2-1: Just excavated mineral samples in raw form (left) and selected pure halloysite, halloysite dispersed in water (right)	7
Figure 2-2: AFM (A) display of HNT with z – axis. and TEM (B) image of halloysites (HNTs) [8]	8
Figure 2-3: Schematic representation of HNT’S physiochemical structure. [4]	8
Figure 2-4: Drug (paclitaxel) lumen loading with vacuum method (a); aspirin physical adsorption on the surface of APTES modified HNT’s. [25]	11
Figure 2-5: (A) schematic representation of the HNT etching process to increase lumen loading. (B) Graph displaying the percentage increase of the inner lumen after etching. [28]	11
Figure 2-6: Brilliant green drug loading inside HNTs with benzotriazole–copper. coating reprinted with permission from [16].	13
Figure 2-7: Illustration of the selective modification of halloysite surfaces by ionic surfactants. [4].....	14
Figure 2-8: TEM image of pristine HNTs (A); TEM image of brilliant green antiseptic loaded HNTs (B); SEM image of an end of pristine nanotube with open lumen (C); and SEM image of a dextrin cap on the end of the functionalized nanotube (D) [39].....	15
Figure 2-9: Brilliant green antiseptic loading inside HNTs, release curves in water of the free drug (black) and encapsulated in HNTs (red) and HNTs with stoppers (blue). [16]	16
Figure 2-10: Synthesis of halloysite-CdS composites [4]	18
Figure 2-11: Resazurin assay results demonstrating the LD50 value (50% death level) of BG-loaded HNTs for A549 (A) and Hep3b (B) cells. The two-fold increase of LD 50 for Hep3b cells occurs due to the reduced uptake of HNTs if compared with A549 cells. Inserts show AFM images of distribution of DX-HNTs in cells. [39]	19
Figure 2-12: Synthesis processes of Au-HNTs-DOX@BSA-FA [40].	20

Figure 2-13: Scheme of placing charged proteins selectively outside or inside the clay nanotubes [4].	23
Figure 2-14: HNTs-in-microgel oral systems for protein delivery production (embedded in a microgel) [23].	25
Figure 2-15: Schematic illustration of the preparation and intracellular uptake of HNTs- PEI-siRNA-QDs complex, siRNA release, and target mRNA degradation in cancer cells [59].	26
Figure 2-16: (A) DLS size analysis, (B) zeta potential and (C) thermogravimetric analysis (TGA), (D) AFM images and (E) TEM photos of HNT's and PAMAM-g-HNT'S. [61].	28
Figure 2-17: Illustrations of chemical structure and preparation procedure of HNTs-g- PEG-CDs-Biotin followed by quercetin que adsorption [42].	30
Figure 2-18: Schematic displaying the major cellular building blocks of the Blood Brain Barrier. [9].	34
Figure 3-1: Zeta potential analyzer (ζ - Plus Micro electrophoretic instrument) and its cell (A). Cuvette used for sample insertion into the cell (B)..	37
Figure 3-2: Scanning electron microscope (Hitachi S 4800 FE)	38
Figure 3-3: Thermogravimetric analysis instrument with aluminum pans used to load the test materials (a-b).	39
Figure 3-4: Atomic Force Microscope (Dimension Icon AFM).	40
Figure 3-5: Nikon A1R Confocal and Super Resolution system we used at LSU, Shreveport.	41
Figure 3-6: Transmission Electron Microscope, we made measurement at the Service Center, Arizona State University (Naureen Rahman assisted us).	42
Figure 3-7: Dark-Field Microscope measurements were made for us by Dr. Fakhrullin lab, Kazan University.	43
Figure 3-8: Leica DMI 600B Inverted Microscope (Dr. M. DeCoster lab, Louisiana Tech University).	44
Figure 3-9: Contact angle system QCA (Dataphysics).	45
Figure 3-10: Bruker D8 X-ray diffractometer (XRD) at IfM	46

Figure 4-1: SEM images of larger halloysite clumps (A, B, C) from NorthStar Mine, Utah	48
Figure 4-2: (A-B), TEM images of individual large halloysite displaying their structure and hollow lumen more clearly, made at Service Center Arizona State University.....	48
Figure 4-3: Percentage of halloysite tubes and their respective diameter measured in nm	49
Figure 4-4: Percentage of halloysite tubes and their respective length measured in μm	50
Figure 4-5: Dark-field microscope image of large halloysite sample sent from NorthStar mines. Displaying excellent dispersibility of halloysite nanotubes in water. Made at Kazan University, R. Fakhrullin.	51
Figure 4-6: AFM of dark-field morpho-mechanical tapping mode measurements of multiple halloysite clay nanotubes.....	52
Figure 4-7: SEM images of “small” halloysite and its size distribution confirming its sizes through the bar graphs shown below (A-D).....	53
Figure 4-8: Bar graphs displaying the measured length and external diameter of normal “small” halloysite with average size being and 400-600 μm in length and 50-70nm in diameter.....	54
Figure 4-9: AFM images of “small” halloysite tubes displaying surface features (A-B). Made by our collaborator Rawil Fakhrullin.....	54
Figure 4-10: TEM images of small halloysite from Applied Minerals Inc displaying their size with respective scale bars (Sigma-Aldrich) (A-D). Made at Service Center, Arizona State University.....	55
Figure 4-11: X-ray diffraction pattern from halloysite powder, wavelength 0.154 nm (Cu $K\alpha$ radiation), characteristic halloysite peak is visible at $2\theta = 12.2^\circ$ indicated with an arrow.....	56
Figure 4-12: Scheme of “nano torpedo” halloysite penetrating pig skin and delivering vitamin B-12.....	57
Figure 4-13: Thermogravimetric analysis displaying a negative control of pristine “large” halloysite. Where only the halloysite is present, undergoing a phase transition at 550° C.	60

- Figure 4-14:** Thermogravimetric analysis of large HNT + B12, displaying a 9.5 % total loading percentage with the B-12 decomposed at 350° C and halloysite underwent a phase transition at 550° C...60
- Figure 4-15:** SEM image pig skin treated with 0.25g of HNT + B-12 displaying no nanotubes on the surface after massaging it onto the skin.....61
- Figure 5-1:** Loading clay nanotubes with fluorescent rhodamine (RITC) and ionomycin and treating the endothelium cells with the loaded nanotubes. Ionomycin-HNT upper route with Ca²⁺ imaging monitoring and RITC – lower route accomplished with visualization [75].66
- Figure 5-2:** A co-culture model of brain endothelium and astrocyte membrane developed for testing the penetration and delivery of HNT nanotubes and their payload (RITC) across the blood–brain barrier model [76].....67
- Figure 5-3:** (A) Primary glia treated with puromycin for isolation of brain microvascular endothelial cells (BMVECs) showing killing of all other cell types except the BMVECs. (B) Primary BMVECs characterized by staining against VWF using fluorescence microscopy, and (C) phase image of stained cells. Magnification 200X, scale bar = 200 μm. [75]70
- Figure 5-4:** Release profile of rhodamine isothiocyanate-RITC loaded into HNT taken at 555 nm.....73
- Figure 5-5:** Phase and fluorescence imaging of primary brain endothelial cells treated with RITC only (A, B), and with halloysite clay nanotubes loaded with RITC (D, E) after 30 min exposure. Merged images for the phase and fluorescence settings (C, F). Magnification 200X, scale bar = 200 μm [75]74
- Figure 5-6:** Phase and fluorescence microscopic imaging of primary endothelial cells that were treated with RITC only (A, B), treatment with HNT-RITC formulations (D,E), and treatment with HNT only (G,H) in both phase (right) and fluorescent (middle) settings for 24 h exposure. Merged images for the phase and fluorescence settings (C, F, I). Magnification = 200X, scale bar = 100 μM [75].....76
- Figure 5-7:** Thermogravimetric data for halloysite loaded with ionomycin and glutamic acid (A, B).....78
- Figure 5-8:** Thermogravimetric curves displaying weight change % of pristine HNT, HNT loaded with rhodamine, and HNT loaded with ionomycin.78
- Figure 5-9:** Images captured for BMVECs during Ca²⁺ treatment: (A) before stimulation; (B) peak stimulation by 50 μg/mL of empty halloysite nanotube, and (C) peak stimulation by 50 μg/mL nanotubes loaded with ionomycin. Magnification = 200X [75]81

- Figure 5-10:** Ca^{2+} peak intensity obtained for different stimulation on BMVECs, in the horizontal axis is the image number indicating time periods with total range of 4 s each (1 image no. = 4 s); and in the vertical axis is the normalized values for fluorescence intensity corresponding to calcium activity (A) stimulated by ionomycin (Iono) 1 μM (positive control); (B) stimulated by 50 $\mu\text{g}/\text{mL}$ HNT- ionomycin (sample tested); (C) stimulated by ATP, a well-known Ca^{2+} stimulator (positive control indicating healthy cells), followed by HNT-ionomycin formulation (10 $\mu\text{g}/\text{mL}$) showing the comparison between the Ca^{2+} responses of physiological stimulation (ATP) and HNT- ionomycin formulation for the same cells. (D) Cells stimulated by 10 and 50 $\mu\text{g}/\text{mL}$ of HNT-ionomycin showing comparative results for the cells when stimulated by lower and higher dose of HNT-ionomycin; (E) stimulated by 50 $\mu\text{g}/\text{mL}$ of empty HNTs (negative control). [from our paper 75].....82
- Figure 5-11:** (A) Signal analysis scheme. (B–D) Parameters obtained from each calcium signal averaged over the region of interests ranging from 41 to 140 for each condition in a single experiment and then averaged for three experiments. The error bars represent the standard deviations in between the experiments [from our paper 75]84
- Figure 5-12:** DiffQuik-stained images of a model brain barrier of aco-cultured endothelial astrocytes plated on a porous membrane. (B), (C) (z-stack images with a 0.3 μm step size) of non-inverted microscopy images of the transwell assay with a layer of b astrocytes and c endothelial cells [76].86
- Figure 5-13:** Controls (A) 20 $\mu\text{g}/\text{mL}$ HNT-RITC fluorescence intensity (no cell inserts, direct addition to the bottom well), (B) 20 $\mu\text{g}/\text{mL}$ HNT-RITC added to the support, and (C) membrane support treated with media alone [76].....86
- Figure 5-14:** Results of HNT penetration though the membrane: (A, B) fluorescent intensity of the solution beneath the co-culture brain–barrier model after 4 and 24 h of treatment (C). The membrane cell viability after 24 h of treatment with HNT and copper nanomaterials as a negative control [76].....87
- Figure 6-1:** (A) The traces of a mouse that explored the entire open field. (B) Trace of a stressed mouse that did not explore the field's center and confined to the open field's edges.96
- Figure 6-2:** Are the trace of the mouse during the two novel object recognition tests. (A) Trace of the mouse with two similar sized objects (Obj 1 and Obj 2) in the field. (B) Trace of the mouse with one of the objects replace with similar sized object (novel object, Obj 3).97

Figure 6-3: Thermogravimetric analysis of major phase transitions of drugs that were encapsulated in pristine halloysite nanotubes. The phase transition of halloysite by itself is 500-550 °C whilst the respective (RITC, diazepam, and xylazine) drugs underwent burning between 200 and 400 °C. By calculating the respective weight loss in each sample, the loading percentage for RITC was 10 ± 2 wt% and diazepam at 8 ± 1 wt%. Xylazines weight change was calculated at 15 ± 2 wt%.....101

Figure 6-4: Fluorescence images of the brain slices of the olfactory bulb at time points 4, 12, 24 and 48 hours after intranasal administration of HNT-Rhodamine. Images (A), (D), (G), (J) (first column) are phase contrast images. (B), (E), (H), (K) (second column) are images acquired through DAPI filter and (C), (F), (I), (L) (third column) are acquired through TRITC filter. Images from (A) through (F) were acquired using 10x objective and (G) though (L) were imaged through 40x objective.....103

Figure 6-5: Fluorescence images of the brain slices of the cortex region at time points 4, 12, 24 and 48 hours after intranasal administration of HNT-Rhodamine. Images (A), (D), (G), (J) (first column) are phase contrast images. (B), (E), (H), (K) (second column) are images acquired through DAPI filter and (C), (F), (I), (L) (third column) are acquired through TRITC filter. Images from (A) through (F) were acquired using 10x objective and (G) though (L) were imaged through 40x objective. The scale bar is 100 μ m for images (G-L) and 31.5 μ m for (A-F).....104

Figure 6-6: Florescence images of the mice brains that were acquired 4 hours after treatment. The first column (A), (D), (G), (J) (first column) are phase contrast images while the second column (B), (E), (H), (K) are images acquired through DAPI filter and third column (C), (F), (I), (L) were acquired using TRITC filter. The first-row images are from the brain after intranasal treatment with HNTs only while second row with intranasal RITC treatment only, third row with intranasal HNT-Rhodamine administration and fourth row was HNT-Rhodamine treatment intraperitoneally. The images were acquired using 40x for (A-I) and 10x for (J-L). The scale bar for (J-L) is 31.5 μ m and (A-I) is 100 μ m.....105

Figure 6-7: Normalized data showing time of latency to the fall on day 2, 5 and 7. The mice were treated with vehicle (sham), HNTs only, and HNT-diazepam for 6 days. Mice were divided into three treatment groups: sham (n=6), HNT (n=6), diazepam (n=6) and HNT- diazepam (n=6). Using pairwise comparison and Bonferroni correction, a T-test statistical analysis was performed. The data revealed a statistically significant difference between control and HNT-diazepam by day 7 ($p < 0.5$).....106

Figure 6-8: Modified neurological severity scores on day 2, 5 and 7. The mice were treated with vehicle (sham), HNTs only, diazepam, and HNT-diazepam for 6 days. Mice were divided into four treatment groups: sham (n=6), HNT (n=6), diazepam (n=6) and HNT-diazepam (n=6). Using pairwise comparison and Bonferroni correction, a T-test statistical analysis was performed. The data revealed a statistically significant difference between SHAM, HNT, and HNT-diazepam, but no difference between placebo and HNT (p = 1.0).....108

ACKNOWLEDGMENTS

I would like to thank my mother and father along with my mentors, collaborators, family, and friends who have supported me in my pursuit of completing this work. I am grateful for having Dr. Yuri Lvov as my advisor and mentor. His influence and guidance helped me in many ways to achieve our research goals. I would like to also thank the members of my advisory committee: Dr. Mark DeCoster, Dr. Gergana Nestorova, Dr. Shaurav Alam, and Dr. Randy Null. I had the privilege of collaborating with scientists Dr. Fakhrullin from Kazan University, Deborah Dixon from NorthStar LLC, Ana Cláudia Paiva-Santos from Coimbra University, as well fellow students, Neela Prajapati and Yashwanthi Yanamadala.

CHAPTER 1

INTRODUCTION

Halloysite clay nanotubes were studied earlier as a nanocarrier for drug delivery, however, most results were produced for a sustained release in water. In our work we, for the first time, made efforts to investigate delivery in vivo, concentrating on potential ability for halloysite nanotubes to penetrate through biological membranes and skin to deliver the drug load to targeted organs. For this, such a carrier must penetrate through physical barriers of different nature and thickness, such as cell lipid membranes of 10-20 nm thickness and much stronger skin with thickness of fractions of millimeters [1-4]. We are exploiting the hypothesis of “nanotorpedo” based on drugs encapsulated inside smaller 50 nm diameter and 0.7 μm length halloysite clay tubes and developed this work in larger clay tubes of ca 85 nm diameter and 1.5 μm length, capable to penetrate tough barriers. An efficient cross-section of such carriers is defined by their smaller sizes. These larger clay nanotubes were exploited in collaboration with Northstar Mine LLC from Utah. We found that “smaller” halloysite is better for encapsulated drug delivery in membranes such as the blood-brain barrier while larger halloysite nanotubes worked better for stronger barrier, like pig skin which was a model for human cosmetic applications under development in Northstar Mine LLC. Other than the applied results, comparison of small and large halloysite nanotubes confirmed the scroll model for their formation: the larger rolling area consisting of 0.72 nm of thick aluminosilicate sheets

resulted in twice the length of the tubes with ca 30 % larger both external and internal diameters. Depending on geological conditions these sheets may be precursors for stacked plane kaolin multilayer or rolled tubule multilayers. We obtained unique SEM images of the natural structure for such halloysite tubes from kaolin as direct proof of such formation. Halloysite nanotubes are natural abundantly available nanomaterial and have been proven to be a biocompatible material that is dispersible in water and in medical ointment formulations.

It is safe for *in vivo* oral consumption at 0.1 g per 1 kg of weight and not poisonous for cells at concentration below 1 mg/mL, which is much safer than table salt. Halloysite has been used for animal poisoning treatment (piglets and chicken) in addition to multiple human cosmetic applications, as nanocontainers for facial and body creams, as well as hair coloring. Unfortunately, halloysite is not biodegradable, and for intravenous injections, it may be considered only as a model drug carrier with an enhanced ability to penetrate through membranes and biological barriers, such as skin and the brain blood barrier.

Brain diseases, including brain cancer, Alzheimer's disease, and epilepsy are some of the most common diseases, which are constantly increasing in today's elderly populations [5]. Nanomaterials possess specific qualities such as low levels of toxicity, biocompatibility, reduced size, prolonged blood circulation, that enable them to be exploited as a delivery platform that can transport therapeutic agents to the brain. [6]. We decided to take on the challenge of utilizing halloysite nanotubes as a carrier in a "nano torpedo" approach to deliver different molecules to the blood brain barrier (BBB). This barrier is responsible for protecting the brain from all circulating toxins through a

selectively permeable system [7]. It is believed that small molecules freely move across the BBB, ~98% of all small molecules are not transported across the BBB [8-9]. Due to its nature of protecting the brain it is also blocking the progress of new medicinal approaches for brain disorders. The BBB is composed of endothelial cells that act as a gateway by regulating the passage of substances, to a higher degree than endothelial cells of capillaries anywhere else in the body. Additionally, the barrier contains astrocytes which support the endothelial cells biochemically through regulation of ion balance, cerebral blood flow, and repairing the brain when traumatic injuries occur [9-11].

This dissertation is organized accordingly: Chapter 2, a literature review, where descriptions of the traditional “small” halloysite nanotube structure, surface charge, thermal properties, loading with active chemicals, and typical release kinetics, methods of its loading with drugs, release kinetics and means for its diffusion, justifying its value as a drug carrier allowing for sustained 20-40 hours release time. Special attention is given to the description of data on halloysite drug delivery and biosafety. At the end of this chapter, we briefly described future experiments (Chapters 3-4-5) which are derived from the previous knowledge on halloysite nano clay for drug encapsulations.

Chapter 3 describes instruments which were used. Scanning Electron Microscopy (SEM) and Transmission Electron Microscopy (TEM-performed in Georgia Tech University Service Center), Fluorescent Laser Confocal Microscope which we used in LSU, Shreveport Health Center, Atomic Force Microscope - AFM, Dark-field Optical Microscope, Kazan University, Thermogravimetric Analysis (TGA), Zeta-Potential and Sizer Meter, Nitrogen Porosity Meter, Contact Angle Instrument, as well as optical fluorescent microscopy performed in Dr. DeCoster laboratory.

Chapter 4 is devoted to a new type of “larger” halloysite clay nanotubes which we introduced. These clay tubes are like traditional “smaller” halloysite but have a larger diameter of 80-85 nm and length of 1.3-1.5 μm . Their lumen diameter also increased to 23-25 nm, compared to 15 nm of traditional halloysite used earlier in our laboratory. This inner cavity is easily accessible and allows for a larger drug load. Such enlarged halloysite is more than a micrometer, and therefore, is directly visible with dark-field microscopy, as was demonstrated by our collaborator Prof. Rawil Fakhrullin, Chapter 4, Figure 4-5. Visualization of submicron particles with optical microscope in a remarkable achievement. We loaded these large halloysite with rhodamine and presented it to collaborative company Northstar Mine LLC, UT for study of its in-depth skin penetration by color changes while its cream formulation was rubbed at the pig animal application. All indicates that this halloysite may be a more effective carrier for topical drug delivery with enhanced under-skin penetration. Unfortunately, at this research step we were interrupted because the collaborating company Northstar Mine claimed their preferential proprietary rights for further development.

The most essential, Chapter 5 concentrates on usage of smaller (traditional) 50 nm diameter, 0.7 μm length halloysite for penetration through cell membranes and brain barrier. We studied halloysite loaded with rhodamine, ionomycin, diazepam, and xylazine into endothelial cells. In addition to its penetration through the two-cell layered combination modelling a brain barrier. Furthermore, in Chapter 6, experiments were conducted *in vivo* with mice for intranasal halloysite-encapsulated drug delivery. This research was performed in collaboration with Prof. Mark DeCoster lab (Drs. N. Prajapati

and A. Karan) and Prof. Teresa Murray lab (Dr. Y. Yanamadala), where I made all halloysite formulations and assisted in performed cell and brain preparations.

In Conclusions, we formulated our main results and possible future research directions. Overall, we think that halloysite nanotubes, smaller - for cell membranes or larger ones - for skin, as well as nasal formulations, may be used as targeted sustained drug vehicles with size- selection depending on the target organs, for topical body delivery.

CHAPTER 2

LITERATURE REVIEW

This chapter contains fractions from my published review in *Expert Opinion on Drug Delivery*, 2021 on halloysite for drug delivery. When used it, I referred to it as [4]. I was the only graduate student who used this paper material in the thesis.

2.1 Halloysite Nanotube

2.1.1 Physiochemical Characteristics

Developing new methods in medicine by utilizing nanomaterials for disease prevention, diagnostics, and therapeutic strategies is crucial in today's world due to the current use of artificial materials which are associated with toxicity and hazardous concerns [1-4]. The pursuit for natural green materials to aid in medicinal treatment has been ongoing, among those are halloysite clay nanotubes (HNT). These inorganic tubule kaolinite crystal structures are natural clay which occur from interactions of water with silicate minerals or deposits of volcanic ash within sediments. Figure 2-1 displays halloysite in its raw form and dispersed in water. HNT's are inexpensive, biocompatible, and highly functionalized nanomaterials. The availability of these nanotubes is in the thousands of tons form in Northland (New Zealand) and Dragon Mine (Utah, USA). There are several countries around the globe that can produce these clay tubules such as China, Turkey, and Australia. Clay nanotubes like halloysite have been used for centuries in household and clinical applications as safe bulk material without exploiting its

nanoscale features. We also established contacts with a new company that produces halloysite, NorthStar Mining LLC, which is located close to Dragon Mine but has larger size halloysite nanotubes which we exploited for the first time.



Figure 2-1: Just excavated mineral samples in raw form (left) and selected pure halloysite, halloysite dispersed in water (right)

HNT's are unique due to their physiochemical characteristics, well known due to the high surface area and porosity they possess. They are formed by rolling flat sheets of kaolinite (aluminosilicate) 15–20 times [12], that forms into a distinctive multi-layer hollow tubular structure with a lumen diameter of 15 – 20 nm, an outer diameter of 50–70 nm and a length of 400–800 nm [13]. Figure 2-2 displays the size and shape of HNTs with atomic force microscopy (AFM), transmission electron microscopy (TEM) and scanning electron microscopy (TEM). The tubule has an $\text{Al}_2\text{Si}_2\text{O}_5(\text{OH})_4 \times 2\text{H}_2\text{O}$ [14] composition. HNTs inter layer wall periodicity is 0.72 nm, where Al is exposed in a gibbsite octahedral sheet (Al –OH) at the inner surface and siloxane groups (Si–O– Si) are presented at the external surface [15,1]. Figure 2-3 displays the chemical composition of halloysite. This configuration consists of a positively charged inner lumen, composed mostly of aluminum hydroxide and a negatively charged surface, consisting of silicon

dioxide. The colloidal features of HNTs are comparable to 100 nm diameter silica nanoparticles.

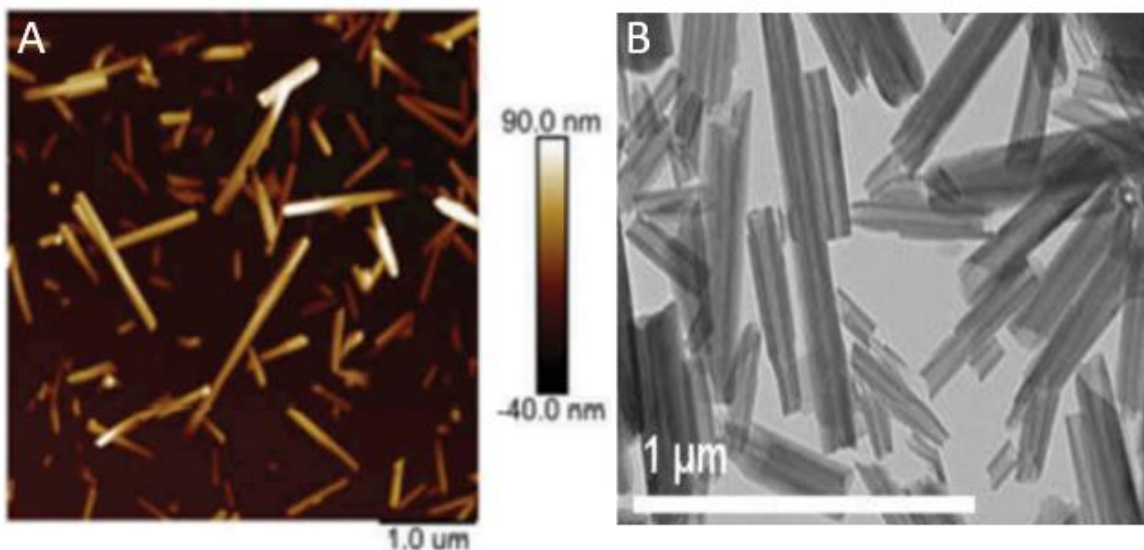


Figure 2-2: AFM (A) display of HNT with z – axis. and TEM (B) image of halloysites (HNTs) [8]

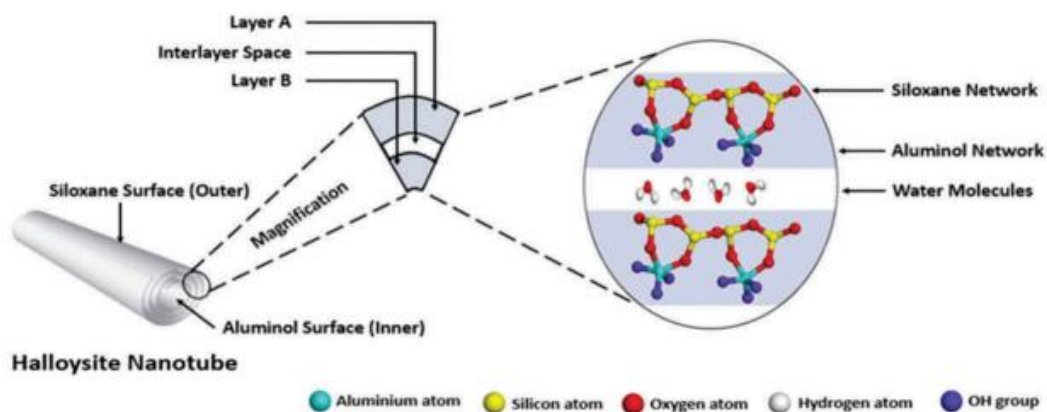


Figure 2-3: Schematic representation of HNT'S physiochemical structure [4]

HNTs are easily dispersible in water, acetone, alcohol, and polar polymers. Having a negative zeta potential ca. -30 mV in a wide pH interval (3 to 8) forming suspensions stable for 2–3h [16]. Opposite inner/outer charges of these clay nanotubes

allow for selective immobilization of charged molecules such as drugs and proteins. The encapsulation of molecules, as well as the attachment of them to the outer surface is driven by electrostatic adsorption. The most interesting for long lasting drug release is the tubes' lumen loading or intercalation between the wall multilayers. The HNTs lumen is rather large (10–20 vol %) and enables the loading of different sized molecules, including proteins and DNA. Additionally, several toxicity studies have been addressed recently, demonstrating the feasibility and high biocompatibility of this nanomaterial. In conclusion, HNTs have emerged as a promising system for drug delivery, due to the benefits of stable colloidal formation in water and various creams. Their biocompatibility and elongated 'nano torpedo' structure endows an easier passage of the cellular membranes without compromising the cell cytoskeleton [17].

HNTs were first used as a carrier material for the sustained delivery of drugs and biological active substances by Price and Lvov [14]. Several experiments have been followed focusing the encapsulation and modified controlled release of substances of clinical interest: drugs, such as dexamethasone, furosemide, nifedipine [17] and resveratrol [18]; biopharmaceutical agents such as enzymes (laccase, glucose oxidase and lipase [13]) and therapeutic nucleic acids; natural compounds, like vitamins [19]; and imaging contrasting agents [12,20,21,22]. HNTs have been employed for the oral and topical administration of drugs [23,24]. Orally, they have already been proven to work as an efficient compression excipient in tablets and capsules formulation [25].

2.2 Loading and Release Strategies

The clay nanotubes enable drug encapsulation by three main mechanisms, including lumen loading assisted by a vacuum method, physical electrostatic adsorption, inside or outside, and intercalation. The improvement of drug loading/release patterns requires a surface modification and formation of caps at the end of the nanotubes.

2.2.1 Lumen Loading and Modifications

Lumen loading may be achieved due to the hydrophilicity of the lumen. This enables the high capillary pressure in polar solvents (up to 200 atm) to move aqueous drug solutions into the tubes [15,16]. In this procedure, HNTs are mixed with close to saturated drug solutions. The suspension is placed in a vacuum jar, which triggers the replacement of the air present inside the sample by the drug. Drug-loaded-HNTs are then separated by centrifugation and dried at 60–70° C in an oven. This process is repeated three times to assure maximum loading. Typically, HNTs loading with drug is 7–9 wt. % [12,14]. Recently, the mechanism beyond this procedure has been explained by thermodynamic evidence. The confined water fraction contained in the halloysite exhibits a faster evaporation rate, leading to the drug molecules encapsulation into the lumen. Such occurrence is favored by vacuum pumping [26]. Figure 2-4 illustrates the encasing of paclitaxel into HNTs from an acetone solution by the lumen loading procedure [25]. This simple method allows a drug release profile of 10–20 h [17,25].

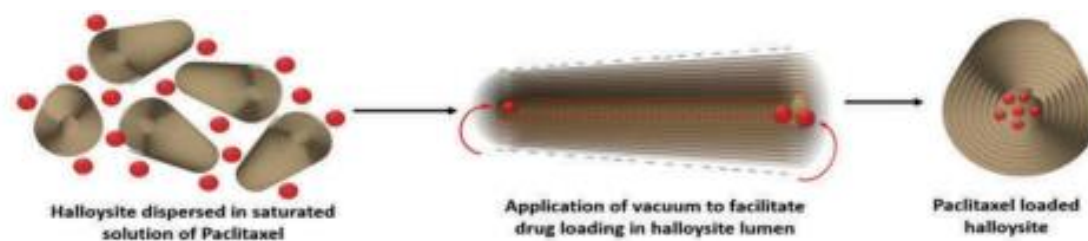


Figure 2-4: Drug (paclitaxel) lumen loading with vacuum method (a); aspirin physical adsorption on the surface of APTES modified HNT's [25]

Furthermore, the alumina-based lumen of pristine HNTs of 10 vol. % may be further increased to 20–30 vol. % by etching, i.e., with acid treatment for several hours. This treatment triples the drug loading capacity, from ca. 10 up to 20–30 wt. %, (Figure 2-5) because of the lumen diameter enlargement from 15 to 25 nm, and, naturally, with a parallel enhancement of the tubes' surface area from ca. 60 m² /g to 250 m² /g [12,27,28].

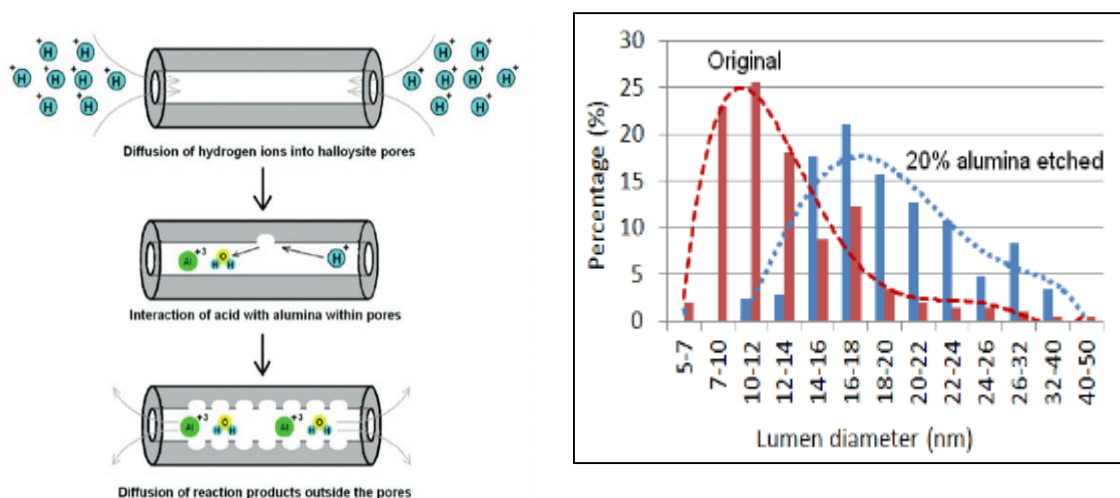


Figure 2-5: (A) schematic representation of the HNT etching process to increase lumen loading. (B) Graph displaying the percentage increase of the inner lumen after etching [28]

In addition, the lumen may be submitted to a hydrophobization procedure to encapsulate low water-soluble drugs from organic solvents. This can be obtained following the adsorption of anionic amphiphilic molecules in the positively charged lumen, conferring the innermost hydrophobic properties without altering the negative charge of the tube's surface. A kind of clay micelle is thereby obtained, preserving nanotubes water dispersibility together with an inner hydrophobic core, that may encapsulate low water-soluble anticancer drugs [29].

2.2.2 Physical Absorption and Electrostatic Enhancement (inside and outside)

The characteristic dual surface chemistry of HNTs, particularly the positively charged alumina lumen together with the negatively charged external silica-based layer allows for selective drug loading. This occurs by the physical adsorption mechanism of negatively charged molecules in the positive lumen as well as positively charged molecules onto the negative surface. Many drugs have been encapsulated through this procedure, including negatively charged DNA and proteins in aqueous media at pH value above their isoelectric point (pI) [13,2]. The bonds between the drug and the HNTs facilitate biofunctionalization and enhance the stability of the nanotube nanoformulations [30]. Conjugation of polymeric materials on the surface of the nanotubes can be carried out. An example of a modification agent is 3-aminopropyl triethoxysilane (APTES), which converts the negatively charged surface of HNTs into positively charged, owing to the amine groups allowing the bonding of biomolecules [30]. This modification also contributes to extending the drug release profile [19,31,32,33,34].

Copper–benzotriazole film coatings at the ends of the nanotubes have been applied to prolong the drug release pattern for 20–100 h [16]. Figure 2-6 illustrates brilliant green loading using copper– benzotriazole HNTs coatings. Tetraethoxysilane (TEOS) and octyltriethoxysilane (OTES) have been used to modify the wettability and the drug release profile of the nanocomposites [35].

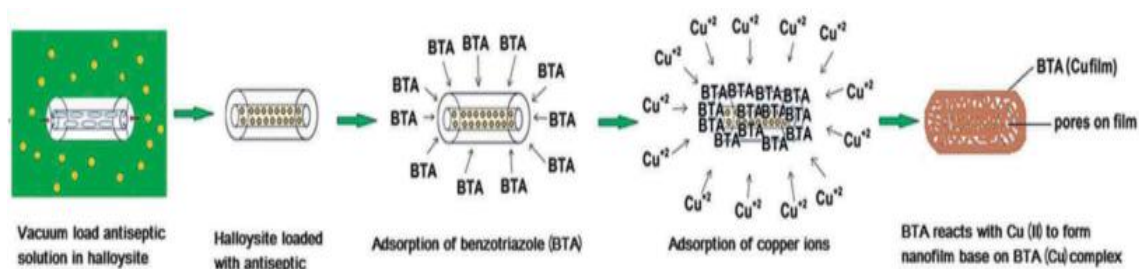


Figure 2-6: Brilliant green drug loading inside HNTs with benzotriazole–copper coating. reprinted with permission from [16]

2.2.3 Tube’s Surface Modification

Layer-by-layer (LbL) self-assembly on the HNTs surface is made by the alternate adsorption of oppositely charged polyanions. The deposition of highly active coatings has extended drug release, resulting in superior therapeutic performance [36,37,38]. In another approach cationic amphiphiles may be adsorbed on negatively charged HNT surface, while anionic amphiphile will go into the positively charged lumens (Figure 2-7).

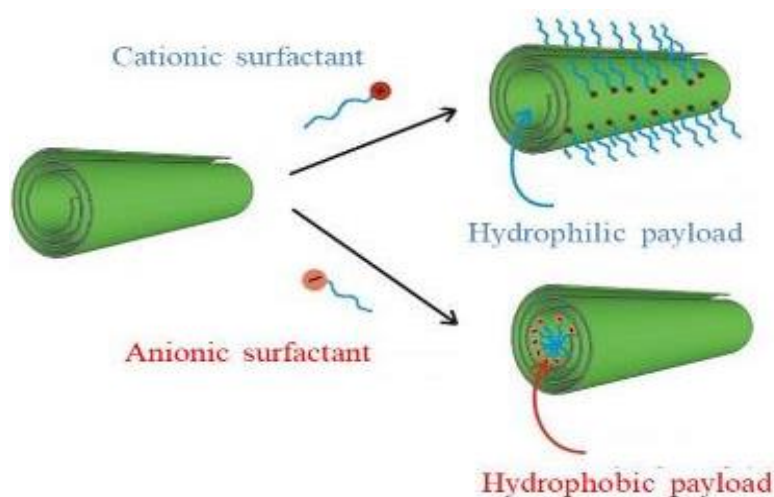


Figure 2-7: Illustration of the selective modification of halloysite surfaces by ionic surfactants [4]

Additional modifications of the surface have been carried out for drug targeting through cellular recognition. HNTs have been modified by dextrin coating. Figure 2-8 (A-D) images a dextrin cap at the end of the nanotube. It is enzyme-responsive and targets drug release to the intracellular medium through the enzymatic degradation of dextrin with glycosyl hydrolases [39]. Folic acid was also used to target the drug release to over-expressed folate-receptor cells [40,41] and biotin [42]. A redox-responsive target capability was also allowed by the presence of a disulfide bond between thiol groups and perthiol- β -cyclodextrin (β -CD-(SH)₇), sensible to glutathione present in high concentration in cancer cells [40]. Other targeting strategies sensible to glutathione is the linkage of cysteamine by a disulfide bond to the external surface of HNTs [43]. Drug-loaded HNTs may be embedded into bulk polymers [14], gels (as nanoparticles-in-microgel oral systems (NiMOS)) [23,44] and electro spun microfibers [33,45,46], which contribute to the stability enhancement of the system and attribute much longer drug

release (up to two weeks). The tubes' wall intercalation procedure is less common when small drug molecules are loaded into the interlayer space of HNTs, e.g., ethylene glycol and urea, which causes the expansion of those layers [2].

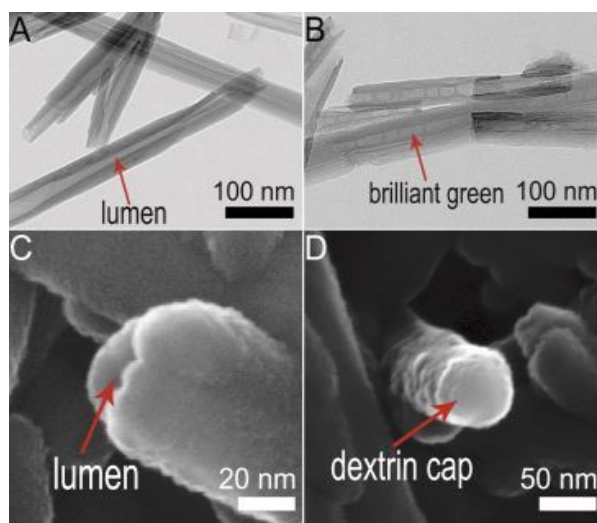


Figure 2-8: TEM image of pristine HNTs (A); TEM image of brilliant green antiseptic loaded HNTs (B); SEM image of an end of pristine nanotube with open lumen (C); and SEM image of a dextrin cap on the end of the functionalized nanotube (D) [39]

2.3 Halloysite Antiseptics Applications

Due to the high zeta potential magnitude, HNTs give stable colloids in water, enabling antiseptics encapsulation for antibacterial sprays. Brilliant green, which usually takes 15 min to be fully dissolved, was loaded into the lumen of HNTs at 15 wt. % and it was sustained released over 6 h (Figure 2-9). Benzotriazole–copper complexation at the tubes' ends enabled an extension of the release profile from 50 to 200 h. This was reflected in higher antibacterial efficiency of the loaded brilliant green, extending its action to 72 h when tested against *Staphylococcus aureus* cultures. An extended release of amoxicillin and iodine was also verified after the loading into HNTs [16]. The long-lasting antiseptics release was also demonstrated for chlorhexidine, povidone iodine, and

iodine. HNTs were also included in electro spun poly-caprolactone scaffolds allowing for 14 days sustained release, with a superior bacterial growth inhibition [46].

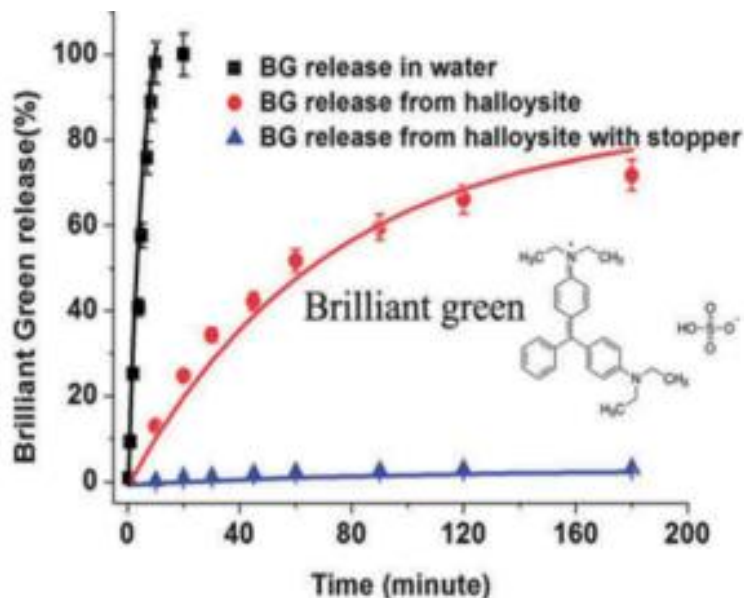


Figure 2-9: Brilliant green antiseptic loading inside HNTs, release curves in water of the free drug (black) and encapsulated in HNTs (red) and HNTs with stoppers (blue) [16]

2.4 Halloysite Diagnostic Applications

Clay nanotubes may be used as template for loading, synthesis, and stabilization of different particles, thus enabling the formation of drug composites with a core-shell nanoarchitecture. Including drug, protein, vitamin formulations and as platforms for imaging contrast agents.

2.4.1 Bioimaging

HNTs were used to stabilize photo luminescent labels: lanthanide complexes (e.g., europium(dibenzoylmethane)³ (Eu (DBM)³)) [47,48]; fluorescent carbon dots [33] and cadmium sulfide quantum dots [49,50]. Overall, the clinical application of the bio labels is constrained by their poor photochemical stability, low water dispersibility and

toxicity [42,47,48,50]. HNTs-based composites make labels more stable and less toxic for clinical applications.

Lanthanide complexes ($\text{Eu}(\text{DBM})_3$) were attached on the surface of polyethyleneimine (PEI)-modified nanotubes via a ligand exchange (4'-(4-bromomethylphenyl)-[2,2':6',2''] terpyridine (MPTP-Br)), forming HNTs-PEI-MPTP-Br-Eu (DBM)₃. This nanocomposite conferred protection against the photobleaching of the luminescent trivalent lanthanide ions, had lasting luminescence emission, a high quantum yield and showed reduced cytotoxicity on human cervical cancer cells (HeLa cell line) [47].

A multifunctional composite with a PEI-modified HNTs was designed to incorporate luminescent lanthanide complexes ($\text{Eu}(\text{DBM})_3$). It proved to have magnetic properties due to the superparamagnetic iron oxide (Fe_3O_4) on the HNTs surface, functioning as a magnetic resonance imaging contrast agent. The in vivo magnetic resonance imaging (MRI) analysis of the nanocomposite showed a reduction of the transverse relaxation signal intensity in the normal tissue, enabling the distinction between cancer and normal cells and demonstrated a reduced toxicity [48].

Carbon dots (CDs) are photoluminescent materials with a diameter of less than 10 nm. HNTs-template was proposed to extend the long-term stability of CDs. The nanocomposite combined therapy and diagnosis, being recognized as a cancer nano theranostic agent [42]. Figure 2-10 illustrates HNT-CdS composites. APTES was used as the grafting agent. This method yielded high surface coverage, effectively reducing the photoluminescence intermittency. Overall, the immobilization of QDs onto the nanotubes prevents their aggregation, confers resistance to the photobleaching and ensures a good

dispersibility in water. HNTs–Azine–Cd_{0.7}Zn_{0.3}S displayed low toxicity in epithelial human prostate cell line (PC-3), constituting a promising cancer intracellular labeling system [50]. Cadmium sulfide (CdS) and cadmium-zinc sulfide (Cd_xZn_{1-x}S) quantum dots (QDs) were immobilized onto the clay nanotube surface to produce safer QDs with blue to green colors and surpass photoluminescence intermittency (‘blinking behavior’).

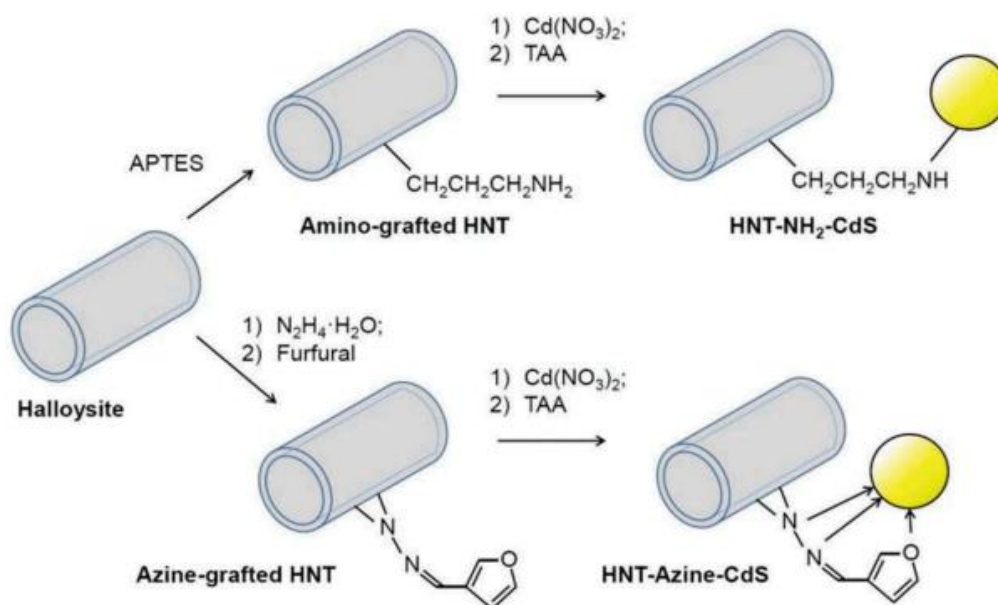


Figure 2-10: Synthesis of halloysite-CdS composites [4]

2.5 Halloysite Applications in Therapy

2.5.1. Drug Therapy

2.5.1.1 *Anticancer Drugs*

HNTs have emerged as a promising system for anti-cancer drug delivery, due to the benefits of stable colloidal formation in water and various creams. Their biocompatibility and elongated ‘torpedo-like structure endows an easier passage of the cellular membranes without compromising the cell cytoskeleton [39]. Brilliant-green lumen loaded HNTs coated with dextrin were shown to promote a stimuli-responsive

intracellular drug release. Dextrin coating was decomposed by the glycosyl hydrolases present in the intracellular media, promoting targeted delivery. Distinct uptake was found between the culture cell lines adenocarcinoma human alveolar basal epithelial cells (A549) cells in comparison to human hepatoma cells (Hep3b) (Figure 2-11) [39].

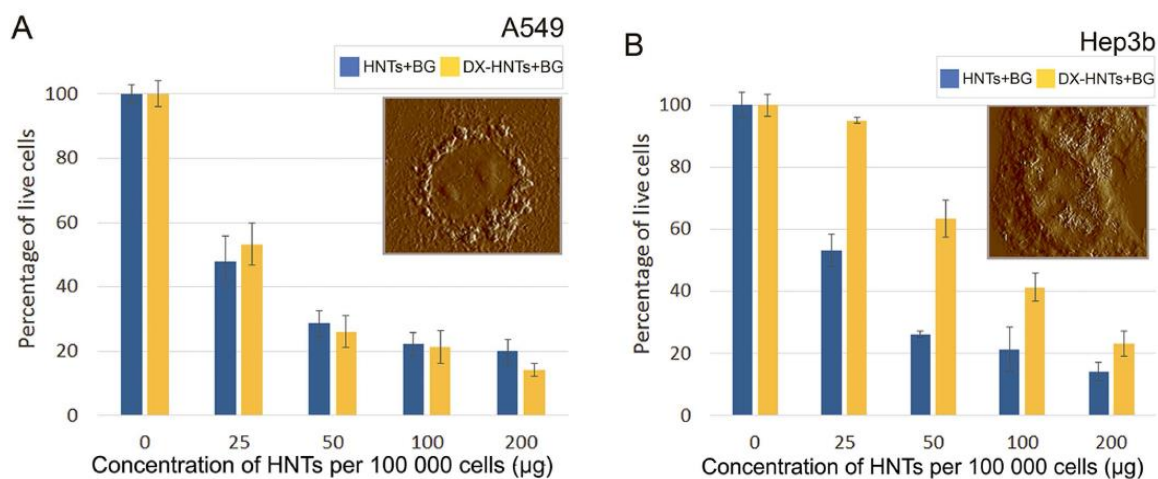


Figure 2-11: Resazurin assay results demonstrating the LD50 value (50% death level) of BG-loaded HNTs for A549 (A) and Hep3b (B) cells. The two-fold increase of LD 50 for Hep3b cells occurs due to the reduced uptake of HNTs if compared with A549 cells. Inserts show AFM images of distribution of DX-HNTs in cells [39]

HNTs were functionalized with PSS to enhance biocompatibility and were applied to encapsulate the US Food and Drug Administration-approved photosensitizer indocyanine green (ICG). The functionalized HNTs-PSS-ICG were associated with giant unilamellar vesicles membranes of human breast cancer cells through Pickering effects and accelerated membrane oxidation. Afterward, the surface modification of HNTs-PSS-ICG with mouse breast cancer MDA-MB-436 cells allowed for a highly efficient in vitro membrane disruption capacity and outstanding in vivo phototherapeutic effects assessed in a breast cancer mice model [51].

Doxorubicin (DOX) is considered the most powerful anticancer drug, however serious side effects are reported following its in vivo administration, requiring new encapsulation delivery systems [52] Gold nanorods were loaded in the lumen, followed by DOX physical adsorption on the surface. The targeting ligand folic acid (FA) was conjugated with bovine serum albumin (BSA), resulting in the Au-HNTs-DOX@BSA-FA nanocomposite (Figure 2-12).

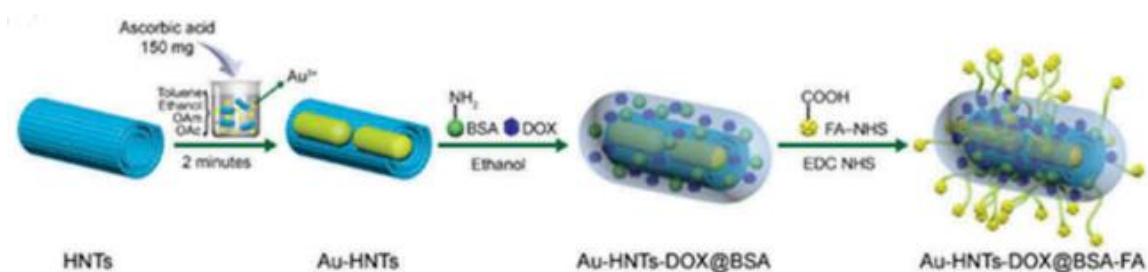


Figure 2-12: Synthesis processes of Au-HNTs-DOX@BSA-FA [40]

The exposition of the functionalized HNTs to near infrared (NIR) laser irradiation triggered a dual effect by combined photo and chemothermal therapies due to a rise in temperature and drug release. The nanocomposites showed good cytocompatibility and hemocompatibility, with no visible drug toxicity in mice. In vivo studies in breast cancer 4T1-bearing mice demonstrated that Au-HNTs-DOX@BSA-FA displayed prominent tumor-targeted efficiency and DOX controlled release pattern, with a prompt photothermal output and the capability to inhibit tumor growth [41]. Soybean phospholipid (LIP) coated nanotubes with DOX were also used to treat gastric cancer. HNTs/DOX/LIP promoted a pH-responsive drug release pattern, with a faster release under acidic environment (pH = 5.4), enabling the targeted drug release. The lifespan of tumor-bearing mice was prolonged in vivo after the administration of HNTs/DOX/LIP

[49]. Folic acid conjugated with chitosan oligosaccharide (COS) assembled with magnetic HNTs were developed as a tumor targeted camptothecin (CPT) nanosystem (CPT@FA-COS/ MHNTs). The pH-dependent drug release pattern proved a triggered release at acidic pH (5.5) rather than neutral and alkaline conditions. A strong cell growth inhibitory effect was encountered against colon cancer cells [53]. Through oral ingestion, HNTs-based tablet formulation was applied through the administration of paclitaxel. Paclitaxel loaded HNTs enabled a pH-independent controlled drug release pattern, but when further modified by a poly (methacrylic acid-co-methyl methacrylate) , the release shifted to basic intestinal conditions. HNTs were identified as a developing compression excipient for tablets formulation [25].

2.5.1.2 Cardiovascular Drugs

Cardiovascular drugs nifedipine and furosemide were encapsulated in HNTs lumen, achieving a sustained drug release profile for 5–10 h [15]. A stimuli-triggered HNTs-based nano system was developed that resulted from the self-polymerization of polydopamine (PDA) on the HNTs surface, followed by their application as fillers in ionically crosslinked alginate gels. The gels were thermally stable and elastic. The HNTs-based gel nanocomposites were applied to encapsulate diltiazem hydrochloride, a calcium channel blocker used for hypertension therapy. In situ drug loading demonstrated superior performance [54]. Nifedipine was also encapsulated into HNTs, which were used to obtain composite tablets constituted by 50 wt. % of the drug loaded HNTs mixed with 45 wt. % of microcrystalline cellulose. Pristine clay nanotubes are excellent tablet excipients, that when composed with nifedipine-loaded HNTs showed a close to zero

order drug release pattern lasting up to 20 h. The system showed an enhanced photostability, suggesting the use of HNTs for oral formulations [55]

2.5.1.3. Anti-Inflammatory and Analgesic Drugs

APTES-modified HNTs were used for the encapsulation of aspirin (acetylsalicylic acid). The internal lumen modification of HNTs with APTES improved the drug loading [31]. A hydrophobic organic-inorganic HNTs-based system was developed to encapsulate and extend the release time of ibuprofen. The nanotube lumen was enlarged to obtain a higher drug loading capacity; and the surface was hydrophobically modified with TEOS to modify the drug release profile. This formulation extends the drug release profile from 40 h (non-modified HNTs) to 100 h [35]. HNTs have also been functionalized with 3-aminopropyltrimethoxysilane (APTS) and a polyamidoamine dendrimer for the encapsulation of ibuprofen and salicylic acid. This hybrid system was effective in the delivery of low molecular weight drugs that contain carboxyl groups [34].

2.5.1.4 Biopharmaceutical Agents

The use of HNTs for intracellular delivery of biopharmaceutical agents, such as nucleic acids, proteins (enzymes and insulin) has taken place. The adsorption of biomacromolecules in the nanotubes confers protection against degradation, enabling a prolonged therapeutic activity and a reduction of doses, toward essentially for anticancer effects [12,13,39]. The biomacromolecules' net charge and the nanotube's inner and outer surface charges dictate the way they are absorbed (Figure 2-13). In the case of proteins, these electrostatic interactions are mainly influenced by the pH of the protein solution [12,13]. The negatively charged HNTs surface area is larger, thus the adsorption of positively charged proteins is a straightforward process.

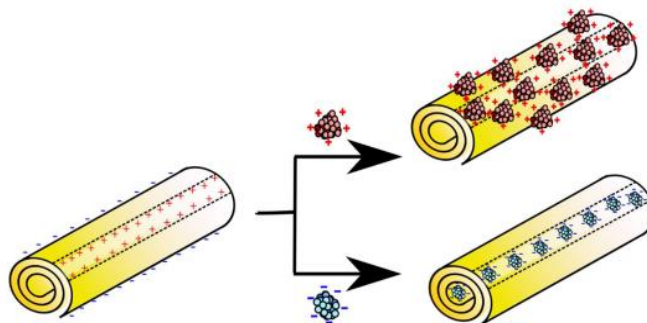


Figure 2-13: Scheme of placing charged proteins selectively outside or inside the clay nanotubes [4]

Negatively charged globular proteins with ca. 2–8 nm diameter were loaded into the positively charged inner lumens (diameter 15–20 nm). Pepsin, urease, peroxidase, lipase, laccase, and GOx are examples of negatively charged enzymes that have been loaded into the lumen of HNT. The adsorption for these enzymes was 6–7 wt. % which is a low value in comparison to the adsorption of positively charged proteins onto the HNTs outer surface, displayed 15–25 wt. %. The release profile of negatively charged enzymes loaded in HNTs showed a faster initial burst followed by a prolonged 10 h release pattern. An advantage of the loading of negatively charged proteins is that more than half of the enzymes permanently remains in the inner cavity of HNTs, creating functional confined enzymatic nanoreactors. Laccase, an oxidase with anti-proliferative properties, was immobilized via electrostatic interactions in HNTs [13]. In a recent study, HNTs immobilization of laccase occurred through a covalent interaction promoted by a crosslinking agent, glutaraldehyde [56]. This nanocomposite constitutes a promising theranostic platform to be applied in cancers overexpressing estrogen receptors, such as cervical or breast cancers [56]. Ribonucleases might also be applied in enzymatic cancer therapy due to their anticancer potential [57].

Binase, a cationic ribonuclease at pH 6–8 (pI = 9.5), was immobilized onto the HNTs to stabilize the enzyme and prolong its release. It was suggested that binase, which shows a cationic and a hydrophobic nature at physiological pH, could be adsorbed on both the outer surface and inner lumen of HNTs. The complex of binase–HNTs showed in vitro anticancer effect toward human colon adenocarcinoma cells (60 % reduction compared to 25 % reduction of cells viability promoted by the exposure to free binase), inhibiting the RAS oncogene downstream signaling pathway [57].

Insulin is a peptide hormone that displays a negative net charge at neutral and alkaline pH, having electrostatic affinity to the HNTs hollow lumen for sufficient loading. The complexes with 2.6 wt. % of insulin loading showed a 20 % release in the first 10 h followed by a prolonged release during 120 h. HNTs-nasal spray may be an alternative for sustain insulin delivery [58]. A different possibility for the oral administration of insulin is the use of NiMOS, which consists of the protein loaded HNTs entrapped in microgels produced by the milling method (Figure 2-14) [23].

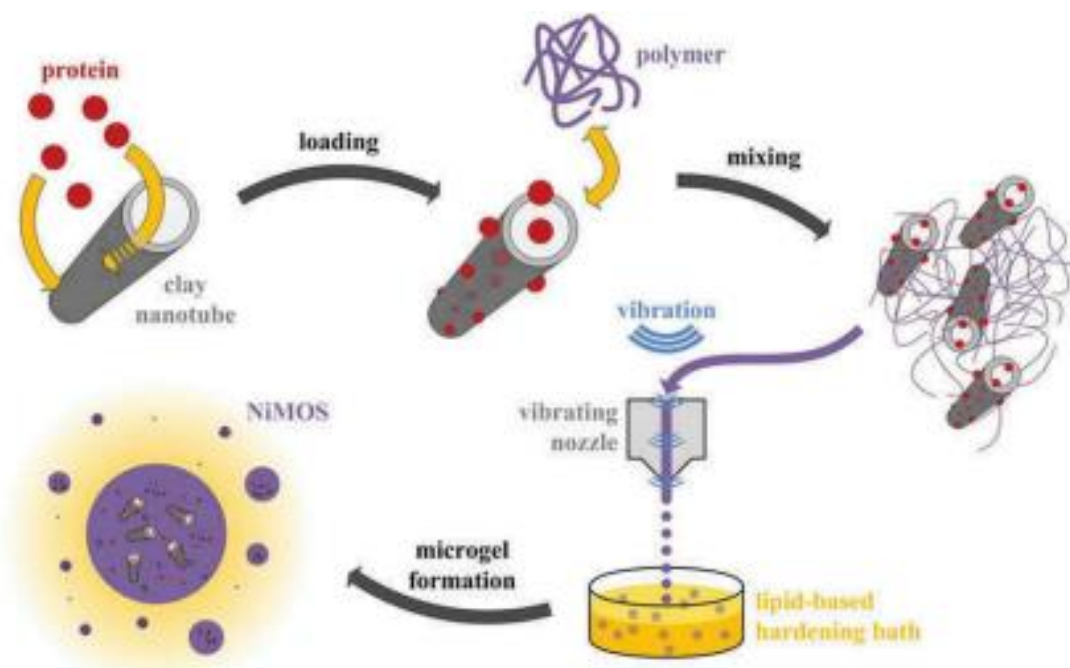


Figure 2-14: HNTs-in-microgel oral systems for protein delivery production (embedded in a microgel) [23].

Therapeutic nucleic acids hold phosphate groups responsible for their anionic nature at physiological pH. Affinity to the aluminol (Al–OH) groups of HNTs lumen may stabilize and protect nucleic acids from degradation by DNases and RNases, enhancing their stability and intracellular uptake [12,30]. The use of ball milling led to the adsorption of anionic DNA onto HNTs surface with zeta potential increase from -30 to -65 mV. These results are due to the neutralization of the internal positive charges with insertion of DNA inside the HNT, and probably partial coating of the tube's outside. The DNA-modified HNTs displayed an improved water dispersibility and longtime colloidal stability [59]. The two strategies used for loading and intracellular delivery of therapeutic nucleic acids that inhibit gene expression, antisense oligodeoxynucleotides and small interfering RNA (siRNA), were based on: (i) the hydrophobization of the HNTs surface with APTES, or (ii) its functionalization with cationic polymers, such as PEI [30,60,61].

LbL (layer-by-layer) - sequential polycation / polyanion method was used for polyethylene amine-PEI coating forming PEI-HNTssiRNA-QDs complexes is shown in Figure 2-15. These complexes showed a high transfection efficiency in human pancreatic cancer cells (PANC-1 cell line) (95.6 %) and stabilized QDs enabling the visualization of the process. The HNTs-based nanocomplexes effectively silenced the gene of interest, inhibiting the survival of cancer cells, displaying their in vitro potential application as cancer gene therapy vectors [60]. To potentiate green fluorescence protein labeled DNA deliver without causing cell injury and inflammation, shortened HNTs with 200 nm length were used. In human cervical epithelial adenocarcinoma cells (293T and HeLa cell lines) short PEI-grafted HNTs (PEI-g-HNTs) exhibited higher DNA transfection efficiency and reduced toxicity as compared with complexes formed by PEI/DNA coacervates [61].

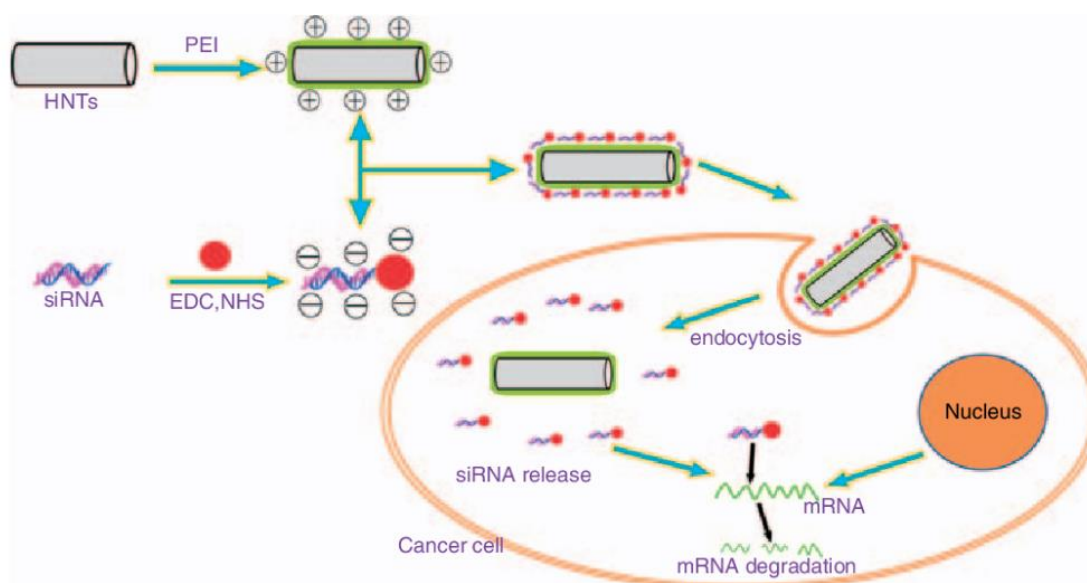


Figure 2-15: Schematic illustration of the preparation and intracellular uptake of HNTs-PEI-siRNA-QDs complex, siRNA release, and target mRNA degradation in cancer cells [59]

Recently, the first in vivo evidence of HNTs used as nano-vectors for gene delivery was given in Long, Wu [62]. Polyamidoamine (PAMAM) dendrimers were grafted onto the surface of HNTs conferring a positive surface charge (+19.8 mV), that enabled the complexation with the vascular endothelial growth factor (VEGF) siRNA (siVEGF). Figure 2-16 displays the structure as well as size, surface charge, and loading analysis of the polyamidoamine modified HNT's. The PAMAM-g-HNTs-siVEGF showed a cellular uptake efficiency of 94.3 % toward human breast cancer MCF-7 cells and reduced by 78.0 % the expression of VEGF messenger RNA (mRNA) inducing the apoptosis of cancer cells. The intra tumoral injection of the PAMAM- g-HNTs-siVEGF suspension (0.7 mg/kg dose) in breast cancer 4T1-bearing BALB/c mice inhibited tumor volume and angiogenesis promoting tumor necrosis [62].

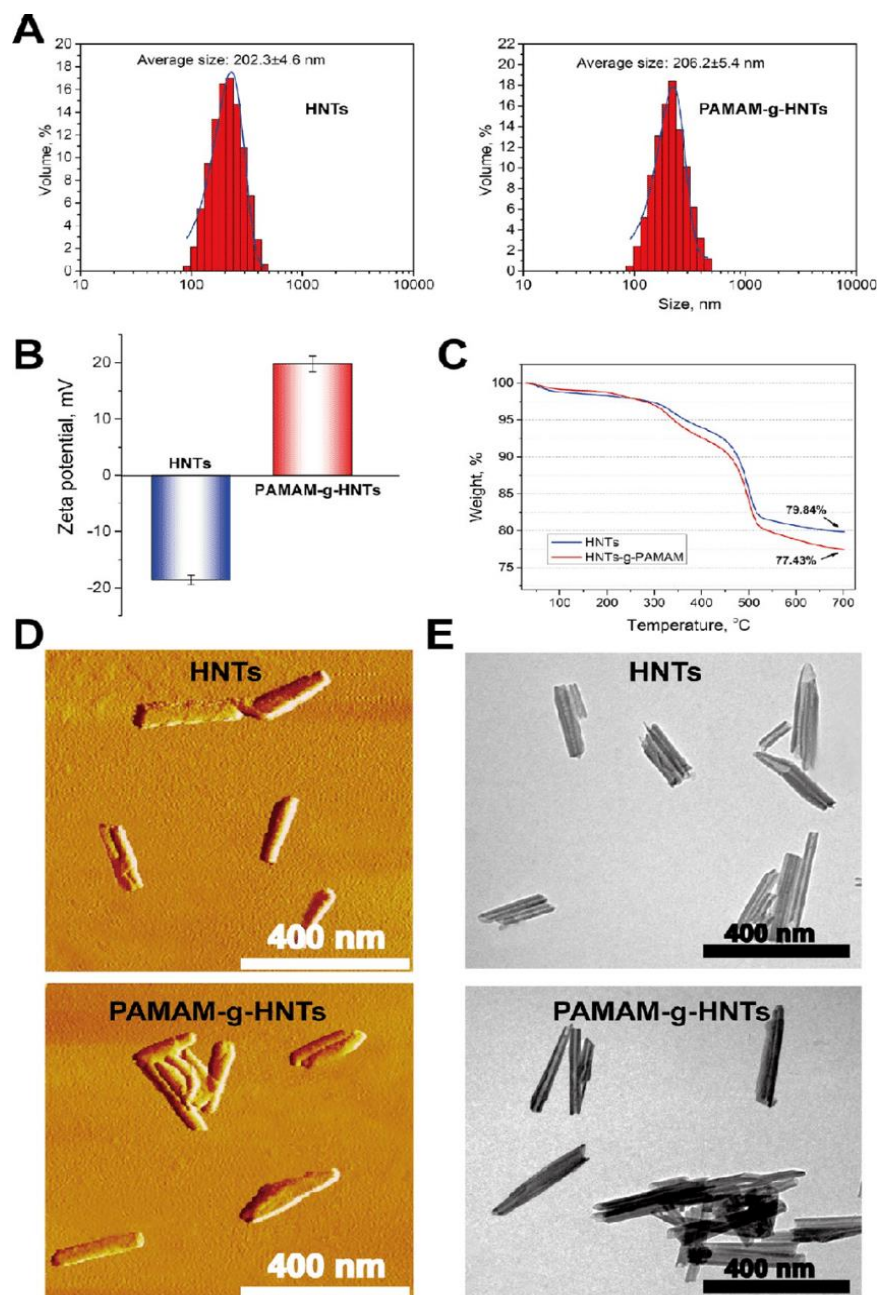


Figure 2-16: (A) DLS size analysis, (B) zeta potential and (C) thermogravimetric analysis (TGA), (D) AFM images and (E) TEM photos of HNT's and PAMAM-g-HNT'S [61]

2.5.1.5 *Natural Compounds – Vitamins*

Curcumin, an actively researched polyphenol, was encapsulated in HNTs whilst the surface being functionalized with poly (N-isopropylacrylamide) (PNIPAAm), a

temperature-responsive material. The colloidal stability and the wettability were triggered by temperature change. Moreover, under gastrointestinal simulated conditions, a targeted enteric drug release was found, preventing the degradation of curcumin in the gastric medium [63]. A dual-stimuli responsive prodrug of curcumin was developed, through the linkage of cysteamine to the outer surface of HNTs, creating a reduction-responsive system. The presence of intracellular glutathione or an acidic environment triggered the curcumin release. A high cytotoxicity was found in two hepatocellular carcinoma cell lines, where the concentration of glutathione is high, as compared to the free drug. This approach is promising toward hepatocellular carcinoma therapy [43].

Curcumin was also encapsulated in HNTs by the synthesis of a NIR-light and hybrid nanosystems. First, curcumin-gold nanoparticles were deposited. The presence of gold conferred NIR-light responsive. The HNTs were then coated with chitosan, which attributed pH-responsive features. Curcumin's release pattern was pH-dependent, triggered in acid media (pH = 5.5) rather than extracellular conditions (pH = 7.4). The formulation anticancer activity was found on MCF-7 cells [64]. The HNTs surface modification with poly (methyl vinyl ether-co-maleic acid) (PMVEMA) promoted interactions with the intestinal Caco-2/HT29-MTX cells/epithelia, increasing the curcumin permeability by 13 times. This was considered as a viable approach for the delivery of curcumin and low soluble drugs by the oral route [65].

Multifunctional quercetin loaded HNTs with targeting and imaging capabilities were also developed. This was achieved by linking covalently 6-arm polyethylene glycol-amine branches (g-PEG) to the surface of HNTs. Photoluminescent features were then introduced by the conjugation of biocompatible carbon dots. Simultaneously, biotin was

conjugated to g-PEG to achieve tumor tissue targeting and higher cellular uptake. Quercetin was then absorbed into the system (Figure 2-17). A sustained and pH-responsive drug release was found. The nanocomposite displayed low toxicity and high biocompatibility, together with an enhanced anticancer activity against HeLa cells [42].

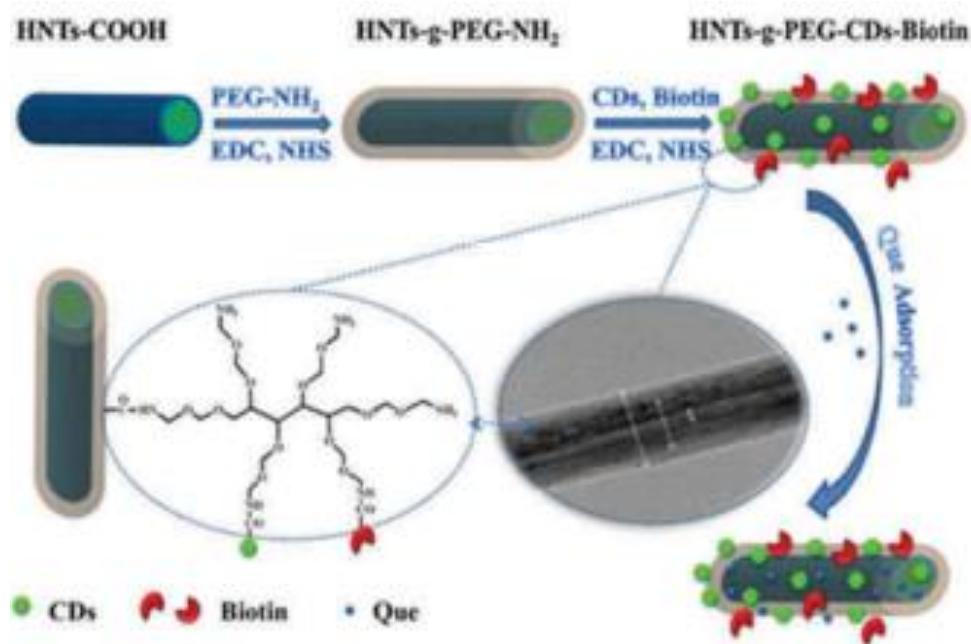


Figure 2-17: Illustrations of chemical structure and preparation procedure of HNTs-g-PEG-CDs-Biotin followed by quercetin que adsorption [42]

HNTs may also be applied for the encapsulation of volatile substances since the loading process does not use high temperatures. Carvacrol, an essential oil endowed with antimicrobial properties was loaded into hydrophobized HNTs to enhance its thermal stability, which enables low-density polyethylene melted compounding. Remarkable antimicrobial properties were reported against *E. coli*, *Listeria innocua* and *Alternaria alternate* [66]. Thyme essential oil was also encapsulated into the lumen of HNTs followed

by end-capping or LbL external coating. A release pattern was identified over many days, and high antibacterial effect was reported against *E. coli* [38].

2.6 Toxicity and Nanosafety

The toxicological profile of this clay nanomaterial has been investigated mostly in *in vitro* and few works – in *in vivo* conditions. A high level of biocompatibility and low cellular toxicity of HNTs have been reported in cervical adenocarcinoma (HeLa) and breast cancer cells (MCF-7). HNTs are nontoxic for concentrations as high as 100 $\mu\text{g/mL}$ [67]. In human umbilical vein endothelial cells (HUVECs) and MCF-7 cells, HNTs at $\leq 200 \mu\text{g/mL}$ displayed biocompatibility, low toxicity, and the capability to be absorbed by cells [68].

Polycations have been extensively employed for HNTs surface modifications. In *in vitro* testing cytocompatibility, uptake, and toxicity showed alterations in cellular nuclei morphology [69]. The blood compatibility of HNTs was also investigated for higher concentrations of HNTs (0.5 mg/mL). Red blood cells change, and aggregation was detected. HNTs can stimulate complement activation, affect coagulation pathways, and alter the thromboelastogram in a non-severe way. When tested in the precursor macrophage cell line (RAW 264.7), HNTs follow a concentration-dependent cellular uptake [70].

HNTs are potential inducers of sub-chronic toxicity in mice after inhalation. A blockade of autophagic processes resulting in p62 accumulation was detected, which led to apoptosis, oxidative stress, and inflammatory responses. Results were reversed when trehalose was orally administered to mice, by reducing the levels of p62, favoring autophagy, and leading to lower HNTs-related toxicity [71]. Additionally, HNT sliver

toxicity was studied in mice at body weights of 5, 50, and 300 mg/kg. The results showed that only the mice treated with higher HNTs concentrations (300 mg/kg) displayed growth inhibition and liver toxicity results, but smaller concentrations were safe. The findings were justified by aluminum accumulation and consequent oxidative damage [71]. Mice were administered intra gastrically with two different concentrations of HNTs at 5 or 50 mg/kg throughout 30 days, to access possibilities of pulmonary toxicity. HNTs accumulation and high aluminum levels in the lungs were found in the mice treated with high nanotube doses [72]

No significant toxic effects were detected on *C. Elegans* micro worms, as attributed to the minimal uptake by intestinal epithelial cells, with negligible transportation to other tissues [73]. In *Paramecium caudatum*, the clay nanoparticles studied (montmorillonite, halloysite, kaolin, and bentonite) induced little or no toxicity, whereas significant toxicity was found for the graphene oxide nanomaterials. In fact, concentrations up to 10 mg/mL of HNTs were considered safe showing no harm for the microhabitat of this protozoan [74]. Further nanotoxicity studies were conducted in zebrafish exhibited no acute toxicity and suggested HNTs as a safe nanomaterial for concentrations as high up to 25 mg/mL with no cardiotoxicity observed in the fish [68]. HNTs are considered relatively safe and biocompatible nanomaterials with a reduced potential for toxicity.

2.7 Blood Brain Barrier

The blood-brain barrier (BBB) is responsible for the protection of the central nervous system organs which consist of the brain and spinal cord. Functionalities of the BBB include its ability to ensure a homeostatic environment in the brain, resulting in the

neural network functioning optimally, regulating the uptake and outflow of nutrients such as glucose and oxygen. Additionally, protection of the brain against pathogenic agents such as bacteria through a complex composition of cellular, vascular, molecular, and ionic factors [9]. It protects the brain in such a way that it presents a challenge when attempting to treat brain diseases. The extreme selectivity of the BBB results in the inability for drugs to pass through effectively or at all, in turn making it more difficult to treat conditions that affect the brain. Although, it is important to note that the barrier is not impermeable. There are certain circumstances in which the barrier can be compromised, allowing substances to pass through more easily. For example, the blood-brain barrier may be compromised in cases of inflammation or injury to the brain. It may also be compromised in certain diseases, such as brain tumors or multiple sclerosis [5-11].

2.7.1 Structure and Physiology

The blood-brain barrier is composed of several different layers consisting of endothelial cells, tight junctions, astrocytes, pericytes, and the basement membrane (Figure 2-18) [7,9]. Endothelial cells line the blood vessels in the brain and make up the BBB through the connection of tight junctions which regulate the traffic of molecules. They have special properties that make them different from endothelial cells in other parts of the body. For example, they have fewer fenestrations and transporters [7,10,11]. This makes the BBB increasingly selective in what it enables to pass through. Astrocytes are a type of glial cell that support and protect the neurons in the brain. Astrocytes have long, branching processes that wrap around blood vessels and help to form the BBB [7,10]. They also help to maintain the proper balance of ions and nutrients in the brain.

Additionally, pericytes are cells that are located around the capillaries in the brain. They help to maintain the structural integrity of the blood vessels and contribute to the formation of the BBB [7]. Lastly, the basement membrane is a thin layer of extracellular matrix (ECM) that surrounds the blood vessels in the brain. The ECM is made up of proteins and other molecules that provide structural support and help to regulate the movement of substances into and out of the brain [7,8].

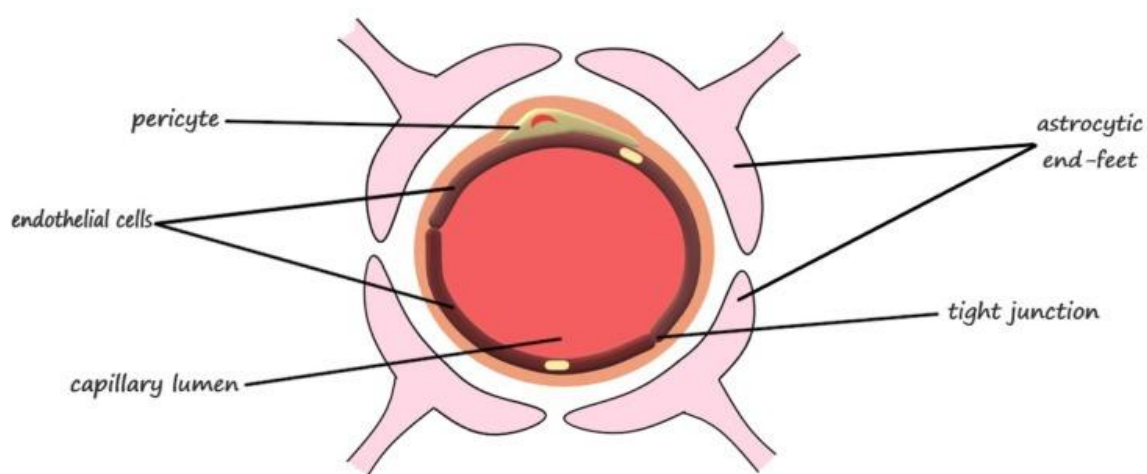


Figure 2-18: Schematic displaying the major cellular building blocks of the Blood Brain Barrier [9]

There are several different ways that substances can cross the BBB. One way is through passive diffusion, which is the movement of substances from an area of higher concentration to an area of lower concentration. This can occur through the tight junctions between the endothelial cells, but is limited to small, lipid-soluble molecules. Additionally, there's a path that is through active transport, which is the movement of substances across the BBB using specific transporters [5,6,7,9]. This can be used to transport nutrients and other essential substances into the brain but is also limited in what it can transport [7,10,11].

2.7.2 Nanotechnology and the Blood-Brain Barrier

The field of nanotechnology is constantly developing innovative techniques to treat brain diseases due to the current limitations of strategies used in present day to pass through the blood-brain barrier. Both gold nanoparticles and carbon nanotubes have displayed their ability to be utilized in imaging, diagnostics, and possible treatment for neurological diseases [9]. Gold nanoparticles coated with polyethylene glycol (PLG) were used to monitor blood vessels in the brain. The resulting images from the mice displayed that the gold particles were successful in capturing the morphology and physiological characteristics of the brain vasculature that is related to brain diseases [9]. Additionally, carbon nanotubes which are made up of graphite sheets have been successful in its ability to cross the BBB and deliver drugs to tumors through multiple in vitro and in vivo experiments [9].

2.8 Conclusions

Halloysite is a natural, biocompatible, inexpensive, and ready-to-use encapsulating nanomaterial with diameter of ca 50 nm and length of 0.5-0.8 μm . Clinically, it promises the development of delivery systems for prophylaxis, diagnosis, and therapy. HNTs are constituted by rolled aluminosilicate sheets that create a structure with a positively charged hollow lumen and a negatively charged outer silica surface allowing for good dispersibility in water, creams, alcohol, acetone, and polar polymers. The empty lumen with 12-15 nm diameter represents an opportunity for drug and proteins encapsulation. This structure enables drugs to be loaded into the lumen by 10–20 wt. %, extending the drug release pattern up to 20-40 h. Acid etching of alumina increases the lumen volume capacity to ca. 30 %. As an example, we may mention:

khellin, oxytetracycline, gentamicin, ciprofloxacin, vancomycin, atorvastatin, metronidazole, dexamethasone, doxorubicin, furosemide, nifedipine, curcumin, resveratrol, and antiseptics - povidone iodine, amoxicillin, brilliant green, salicylic acid, and chlorhexidine [4, 22].

A selective drug immobilization is possible regarding the opposite inner/outer net charge of the tubes' surface. The functional versatility of HNTs includes: LbL self-assembly, amphiphile and silane modifications (TEOS and OTES silane outside coating). Also, these include targeting moieties, such as folic acid or biotin and enzymatically responsive materials (dextrin tube-end-stoppers); or establishing pH-responsive bonds at the tubes' surface (cysteamine disulfide bonds). It enables selective cellular internalization and triggered drug release for anticancer applications. The rod-shape is another distinguished feature of HNT that improves the cellular internalization defined by its smaller cross-section. The pharmaceutical applications available include the encapsulation of anticancer, cardiovascular, anti-inflammatory, and analgesic, drugs, as well as biopharmaceutical agents and natural compounds for therapeutics. Halloysite is considered by US Environmental Protection Agency (EPA) as 4A listed material, thereby seen as natural, nontoxic, and biocompatible.

CHAPTER 3

INSTRUMENTATION

3.1 Zeta-Potential Analyzer

A ζ -Plus Micro electrophoretic instrument (Brookhaven Instruments, Co.) was used to measure the surface charge of halloysite nanotubes. The instrument was calibrated using a standard sample from the manufacturer. For each measurement of the sample, 20 μL of the sample was diluted up to 1.8 mL by DI water. The ζ -potential was measured in ranges of 200 mV to -200 Mv (Figure 3-1).

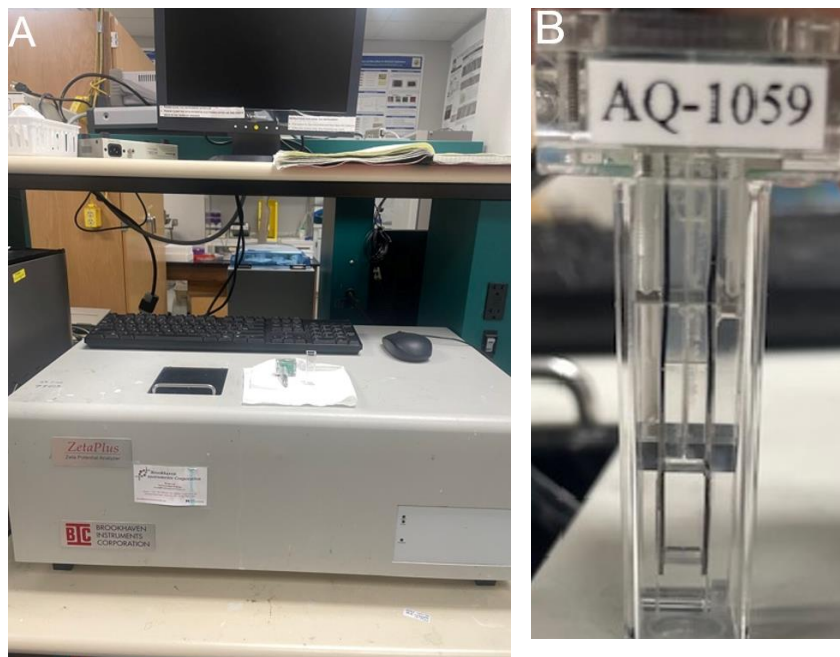


Figure 3-1: Zeta potential analyzer (ζ - Plus Micro electrophoretic instrument) and its cell (A). Cuvette used for sample insertion into the cell (B)

3.2 Scanning Electron Microscope

Scanning Electron Microscope Hitachi S 4800 FE was used for morphology of pristine halloysite nanotubes as well modified halloysite. Samples were suspended in water and dried in oven on a silicon wafer. Samples were then typically sputtered with gold or palladium at ten mA for 60 seconds before imaging to improve conductivity and enhance the image quality (Figure 3-2).



Figure 3-2: Scanning electron microscope (Hitachi S 4800 FE)

3.3 Thermogravimetric Analysis

Thermogravimetric analysis (TGA) was used to determine the loading efficiency of the amount coated of compound on or in halloysite clay nanotubes. Halloysite and its composites with any other compound were heated to a temperature of up to 600° C to determine the quantity of each component in the prepared composites. A heating rate of

60 °C per minute was used for the analysis. The organic content in a composite is only from the loaded/coated compound and thus the weight loss by thermal degradation corresponds to the compound of interest (Figure 3-3).

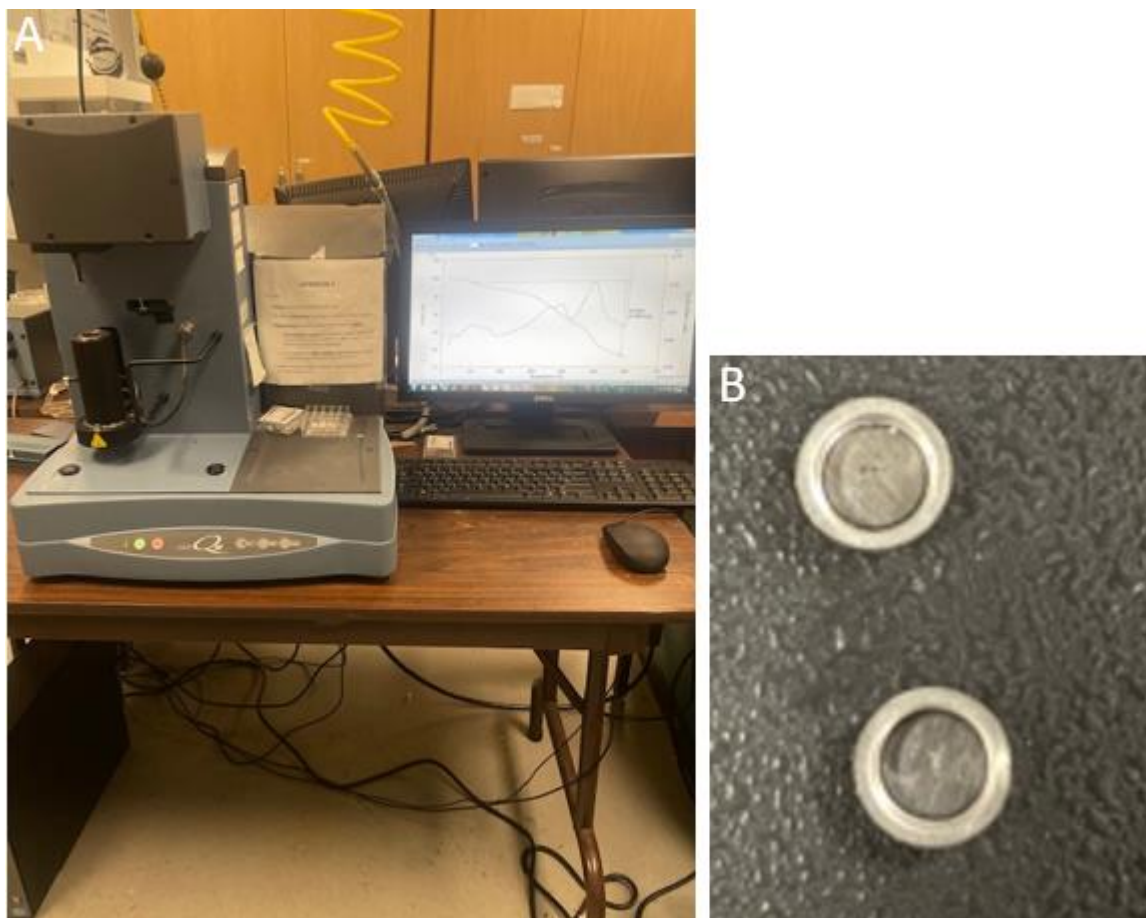


Figure 3-3: Thermogravimetric analysis instrument with aluminum pans used to load the test materials (a-b)

3.4 Atomic Force Microscope

Atomic Force Microscopy (AFM) Dimension FastScan instrument (Bruker) operated by using Bruker Nanoscope software in ScanAsyst™ mode in air using silicon-nitride ScanAsyst Air probes (nominal tip radius 2 nm) was used to visualize the surface topography and charge mapping were observed with atomic force microscopy (AFM)

equipped with Scan Asyst-Air (Bruker) probes (tip radius 2 nm, nominal length 115 μm , spring constant 0.4 nm^{-1}) which analyzed the coating smoothness profiles, nanoclay deposition patterns, and surface potential distribution (Figure 3-4).



Figure 3-4: Atomic Force Microscope (Dimension Icon AFM)

3.5 Nikon A1R Confocal & Super Resolution System

Nikon A1R Confocal & Super Resolution System was used primarily for the model brain barrier experiments, utilizing its Z axis features to determine if halloysites successfully passed through the barrier. Additionally, to analyze the interaction between pig skin samples with halloysite for skin care research. Images were taken at Louisiana State University in Shreveport (Figure 3-5).

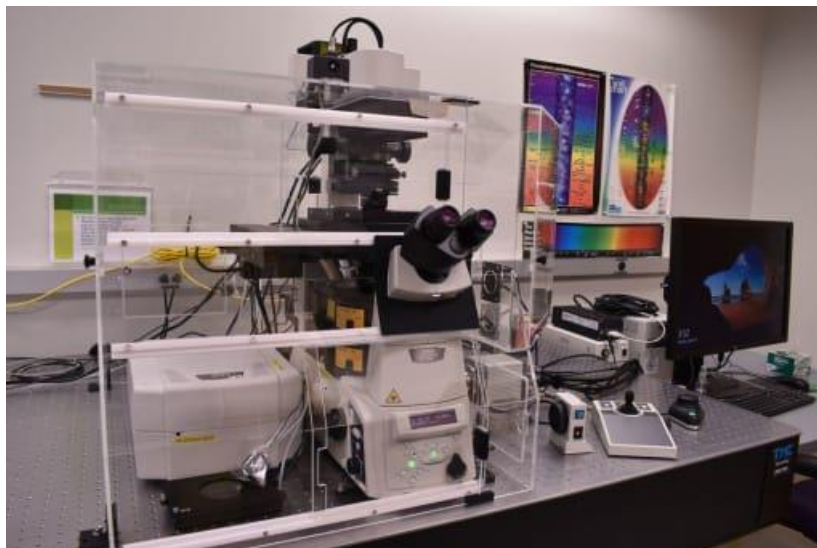


Figure 3-5: Nikon A1R Confocal and Super Resolution system we used at LSU, Shreveport

3.6 Transmission Electron Microscope (TEM) Philips CM 200 FEG

Transmission Electron Microscope (TEM) Philips CM 200 FEG to examine the morphology of halloysite nanotubes. For TEM imaging the samples are dispersed and were dropped on a copper grid, then a negative stain was dropped, followed by removing excess stain by a blotting paper. The sample was room dried and seen under TEM at voltage 80,000-100,000 V. TEM images were obtained using the facilities of Arizona State University (helped with our former student Naureen Rahman) and Georgia Tech University (Figure 3-6).



Figure 3-6: Transmission Electron Microscope, we made measurement at the Service Center, Arizona State University (Naureen Rahman assisted us)

3.7 Dark-Field Microscopy

Dark-field microscopy was performed at our request by Dr. Rawil Fakhrullin, Kazan University. Dark-field microscopy and hyperspectral imaging were performed using a Cyto Viva enhanced dark-field condenser attached to an Olympus BX51 upright microscope equipped with fluorite Olympus oil-immersion (100 \times) objective with tunable numerical aperture and DAGE xL CCD color camera was used to obtain optical microphotographs. Hyperspectral images and reflectance spectra were collected using the same microscope, equipped with a Specim V10E spectrometer and PCO. PixelFly CCD camera. All spectra obtained were processed using the ENVI 4.8 software (Harris Geospatial Solutions) (Figure 3-7).



Figure 3-7: Dark-Field Microscope measurements were made for us by Dr. Fakhrullin lab, Kazan University

3.8 Leica DMI 600B Inverted Microscope

Microscopic images of the cells were recorded under a Leica DMI 6000B (Figure 3-8) inverted microscope. Phase-contrast images of the halloysite and endothelial cell interaction were obtained to identify morphological characteristics of the endothelial cells in the direct contact network which was followed by recording fluorescent images due to the halloysites encapsulation of Rhodamine. For fluorescent imaging, a Leica EL6000 light source was used.



Figure 3-8: Leica DMI 600B Inverted Microscope (Dr. M. DeCoster lab, Louisiana Tech University)

3.9 Contact Angle Instrument

Contact angle system QCA (Dataphysics) (Figure 3-9) were used to measure the contact angle of water on the surface of pellets of halloysite nanotubes. The CCD camera records the shape of the drop residing on the top of the pellet. On a solid surface such as halloysite, the drop shape and the contact angle depended on the solid's surface free energy. The captured image was then analyzed with a drop profile fitting method to determine the contact angle.



Figure 3-9: Contact angle system QCA (Dataphysics)

3.10 X-ray Diffractometer

The Bruker D8 X-ray diffractometer (XRD) (Figure 3-10) is a useful tool for analyzing powder solid crystalline materials. Our IfM system has monochromatic X-ray source with copper anode (Cu $K\alpha$ radiation $\lambda = 0.154$ nm, $V = 30$ kV) for operating in spot focus mode with beam collimators of 0.5 mm diameter. This system is also equipped with a Göbel mirror assembly, Hi-Starr 2D area detector, and a motorized 5-axis sample stage designed in a centric quarter cradle configuration. We employed 500 μm size collimators to allow measurements at relatively small scattering angles of 7 - 10° needed for the first halloysite reflection was resolved. In addition, it has a laser video system for precision alignment of samples and heating stage.

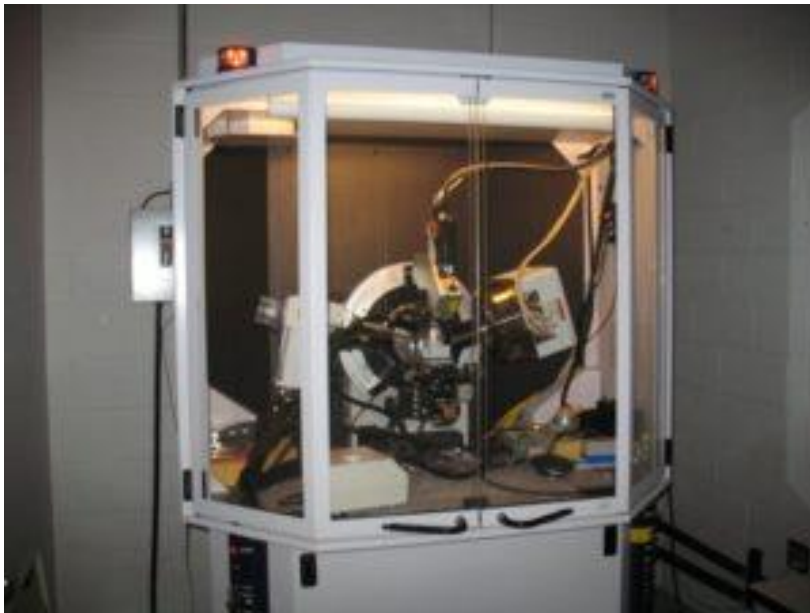


Figure 3-10: Bruker D8 X-ray diffractometer (XRD) at IfM

3.11 Other Supporting Instruments

Branson 1510 ultrasonic water bath (Branson Ultrasonics, U.S.A.) and bench top vortex (VWR, U.S.A.) were used to wash loaded samples as well as disperse aggregated halloysite and halloysite composites. It was also used as a mechanism for enhancing chemical reactions. Centrifuge 5804R (Eppendorf, Germany) with rotor FA-45-30-11 (30 x 2 mL tubes) and 5417C (Eppendorff, Germany) with rotor FA-45-24-11 were used to separate washed material from waste products (supernatant).

CHAPTER 4

SELECTION AND OPTIMIZATION OF THE CLAY NANOTUBE SIZES

4.1 “Larger” Halloysite Nanotubes

Halloysite clay nanotubes are naturally small and have been useful in research through their applications in areas such as ceramics, catalysts and as a carrier in drug delivery. Generally, the size of the halloysite does not vary by a considerable amount in current research. Usually commercially available samples with outer diameter that is 50 nm and a length of 0.7 μm are considered as a current standard. Whilst current halloysite has been exploited, the potential applications if there was halloysite clay with a substantial increase in diameter and length are intriguing. Recently, in conjunction with NorthStar Mines LLC, we have discovered a new halloysite with over micrometer length, characterized it, and determined the high probability of its effectiveness in different areas of drug formulations, specifically for skin care (Figure 4-1, Figure 4-2).

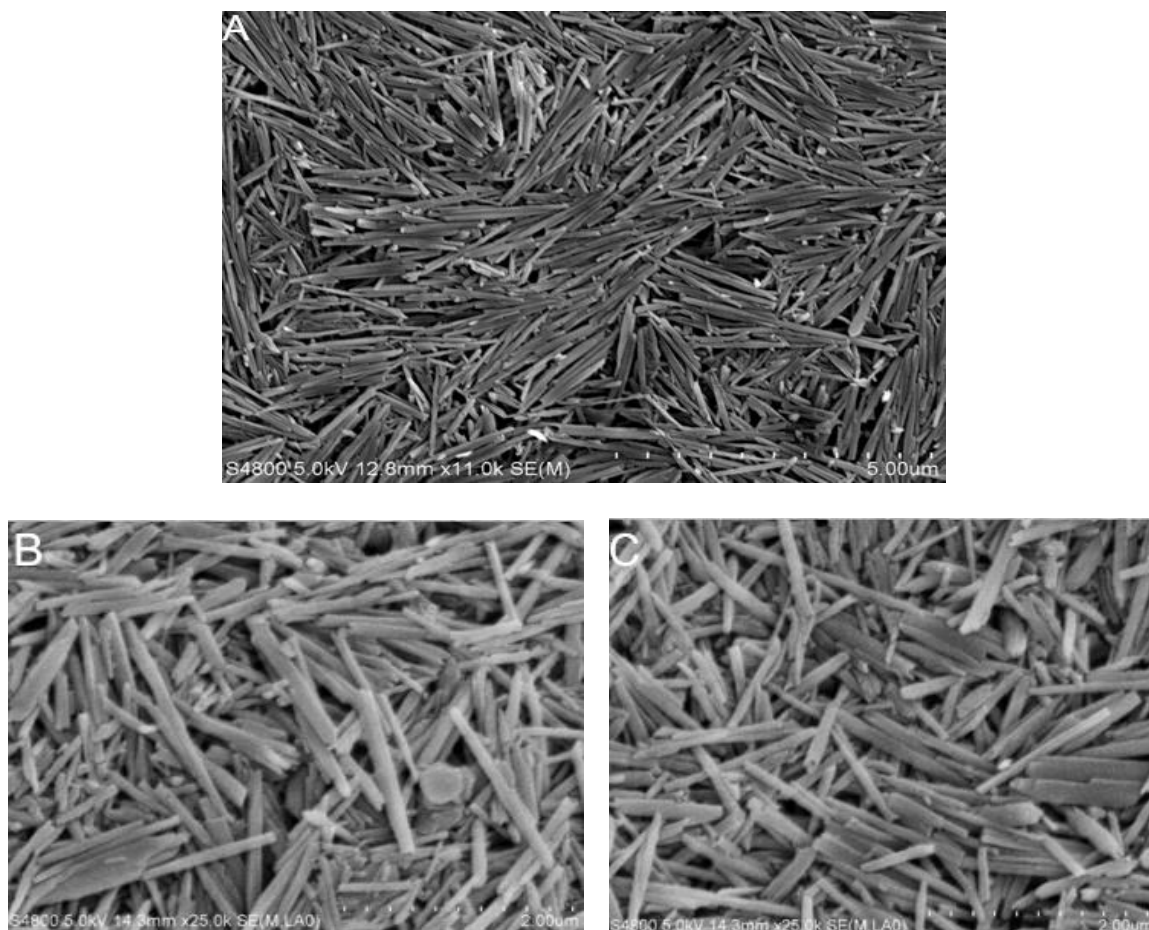


Figure 4-1: SEM images of larger halloysite clumps (A, B, C) from NorthStar Mine, Utah

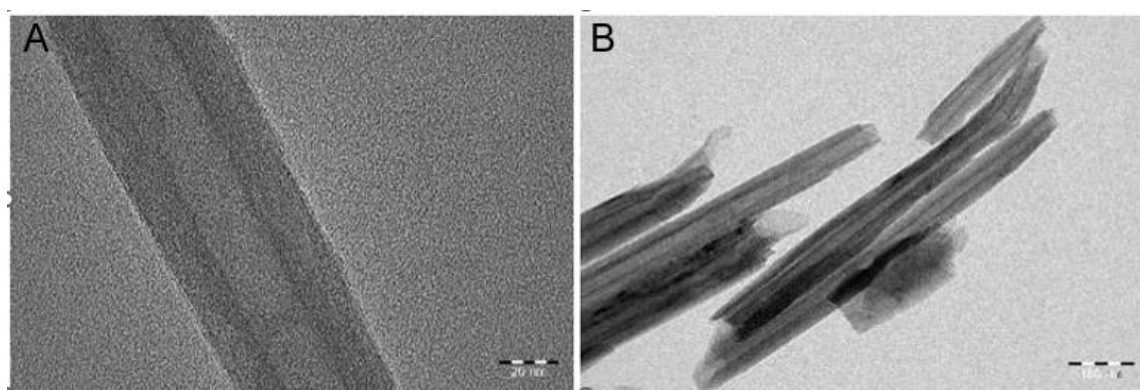


Figure 4-2: (A-B), TEM images of individual large halloysite displaying their structure and hollow lumen more clearly, made at Service Center Arizona State University

The halloysite sample sent to us has been analyzed in depth with multiple instruments to determine the structural characteristics and quality of these nanotubes. First, scanning electron microscopy (SEM) was used to produce images of the tubules, and different regions were selected to gather data about the overall size. Sections of these images were then placed in the ImageJ program to determine the average diameter and length of the halloysite respectively. The average tubular size came out to be 80 ± 10 nm in diameter and a length of 1.5 ± 0.5 μm which is based on the data from Figures 4-1 and Figure 4-2. Afterwards, the contact angle instrument was utilized to measure the wettability of these tubes and resulted in a median of $38 \pm 8^\circ$, indicating that these nanotubes are hydrophilic. Additionally, zeta-potential analyzer was used to determine the surface charge of the tubular structures at -30 ± 5 mV, inferring that the outer shell is positively charged. Thermogravimetric analysis (TGA) was then used to detect the point at which the halloysite burns which can be seen in Figure 4-3 and Figure 4-4 at 550°C . The fact that the electrochemical characteristics are similar, and the size seems to be the only difference opens many avenues for its potential use in the field of research.

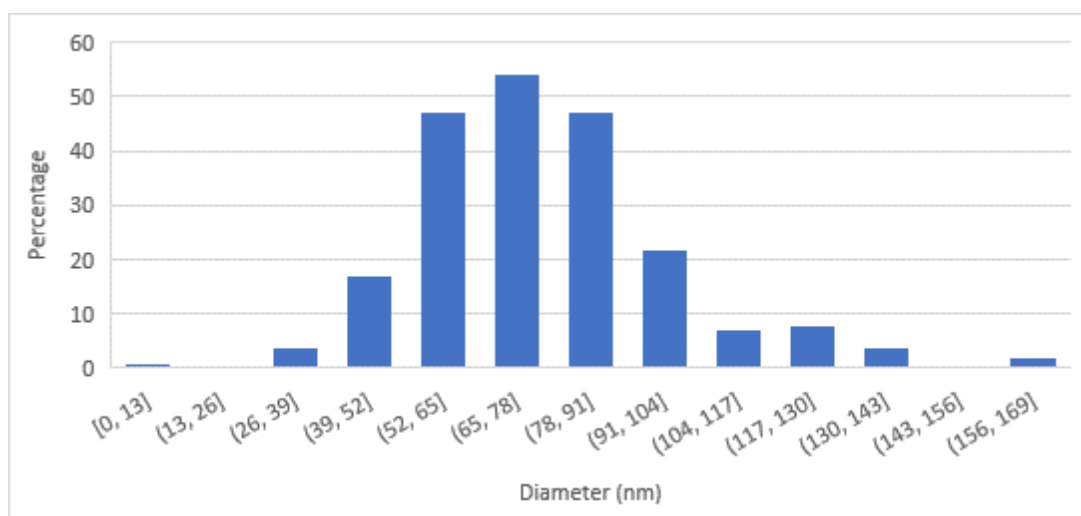


Figure 4-3: Percentage of halloysite tubes and their respective diameter measured in nm

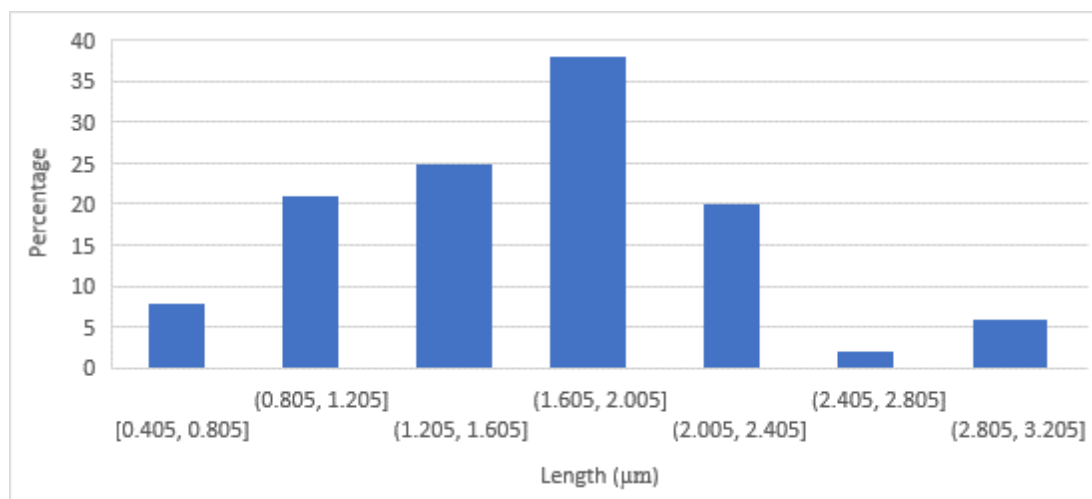


Figure 4-4: Percentage of halloysite tubes and their respective length measured in μm

Microscopy imaging can reveal different characteristics about nanomaterials such as dispersibility, toxicity, and the rate of encapsulation. The ability to see the dispersion rate of these halloysite is a major factor in determining its capability of being exploited as one of the best nanocarriers. To prove this, dark-field microscopy was utilized on these large halloysite in conjunction with atomic force microscopy (AFM) to display that halloysite not only can be evenly dispersed but doing so whilst keeping all its morpho-mechanical properties. The halloysite samples were unmodified and dispersed in distilled water.

These dark field images are of record resolution. One could see nanotubes of diameter 80 nm and length of 1.5 μm . It is a great advantage as compared with traditional “small” halloysite of 50 nm diameter and 0.7 μm length, which was already below the dark-field optical resolution. Luckily, we see a few of the larger horizontally located tubes very clearly and conform sizes obtained from SE, above. Some images look like small dots, obviously they are cross-sectional view of the tubules. Figure 4-5, demonstrate an excellent dispersibility of “large clay nanotubes in water. One cannot see

any aggregate, assuming enhanced permeability of such singular tubes though skin or other barriers.

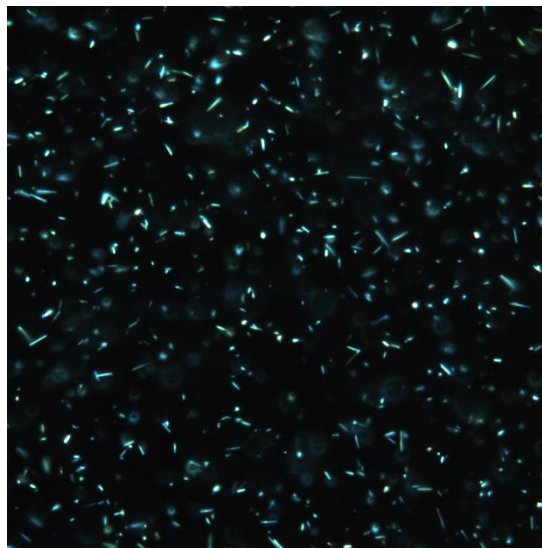


Figure 4-5: Dark-field microscope image of large halloysite sample sent from NorthStar mines. Displaying excellent dispersibility of halloysite nanotubes in water. Made at Kazan University, R. Fakhrullin

In image Figure 4-6, we also see good dispersibility of the tubes, and sufficient similarity. One tube is very long, 3-4 μm , but it is not common. These AFM images confirm sizes obtained from SEM and give some details of aluminosilicate sheets rolling with smaller diameters at the ends.

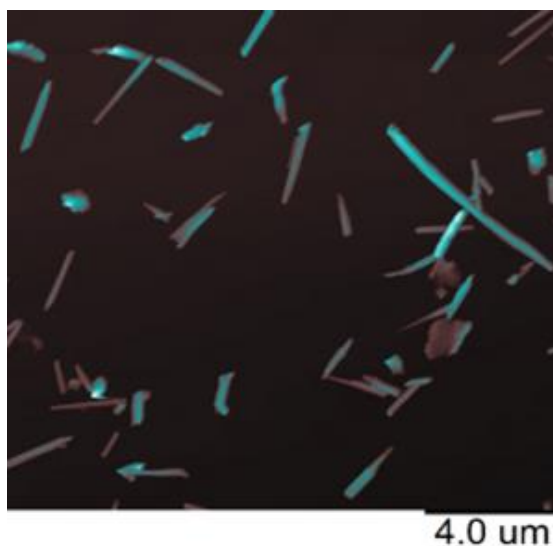


Figure 4-6: AFM of dark-field morpho-mechanical tapping mode measurements of multiple halloysite clay nanotubes

In the next section, 4.2 we will provide a similar structural characterization for traditional “smaller” halloysite and will justify the nanoclay choice for drug delivery through skin and through biological membrane barrier.

4.2 Structural Characterization of Traditional “Smaller” Halloysite Nanotubes

In all previous halloysite experiments, researchers used commercial halloysite mostly purchased from Sigma-Aldrich Co. and produced at Applied Minerals Inc., Utah, USA. Here we provide structural characterization of this halloysite which is of about 50 ± 10 nm diameter, with 15 ± 5 nm lumen and averaged length of $0.7 \mu\text{m}$ (Figure 4-7, Figure 4-8, and Figure 4-9). The purification process of this halloysite includes milling with a ball due to its small nature. Below we provide its images and sizing obtained with TEM and AFM. Figure 4-10 includes images of pristine halloysite which confirms the rolling mechanism of the nanotube formation.

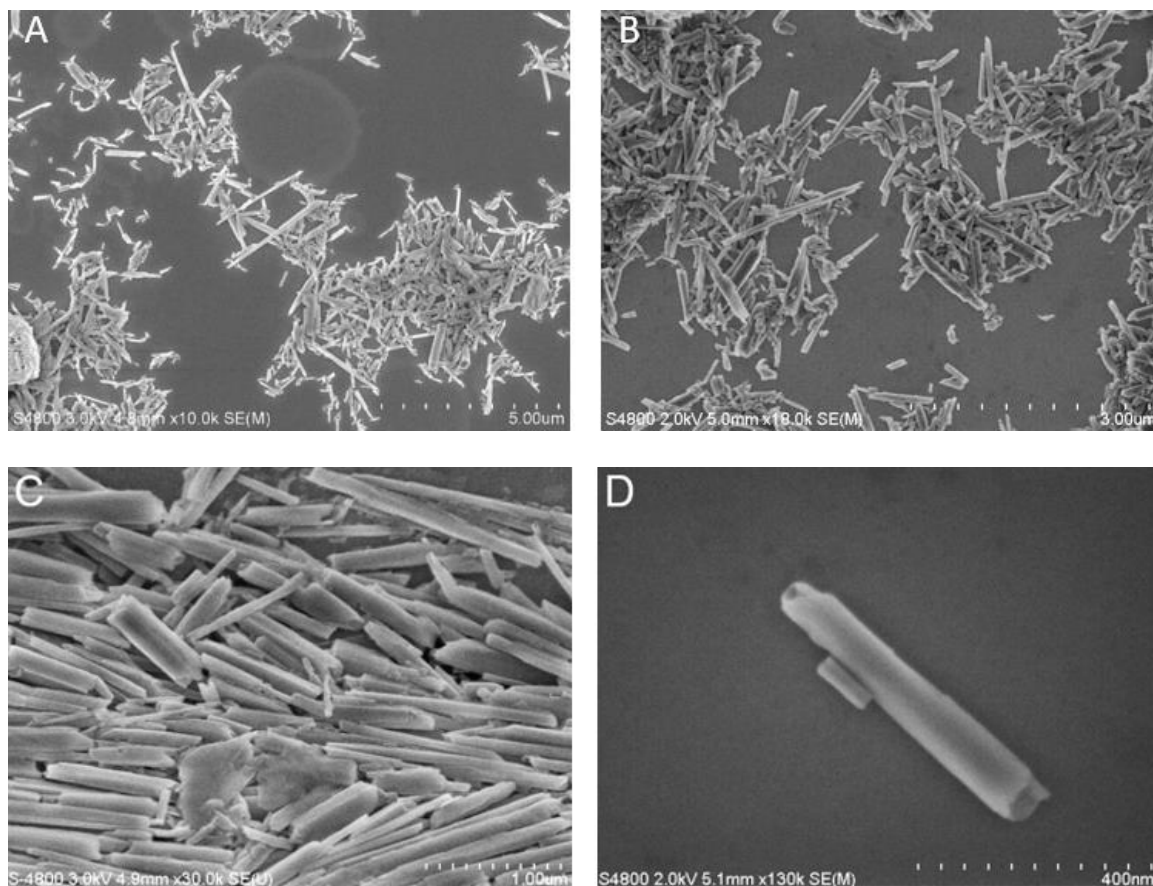


Figure 4-7: SEM images of “small” halloysite and its size distribution confirming its sizes through the bar graphs shown below (A-D)

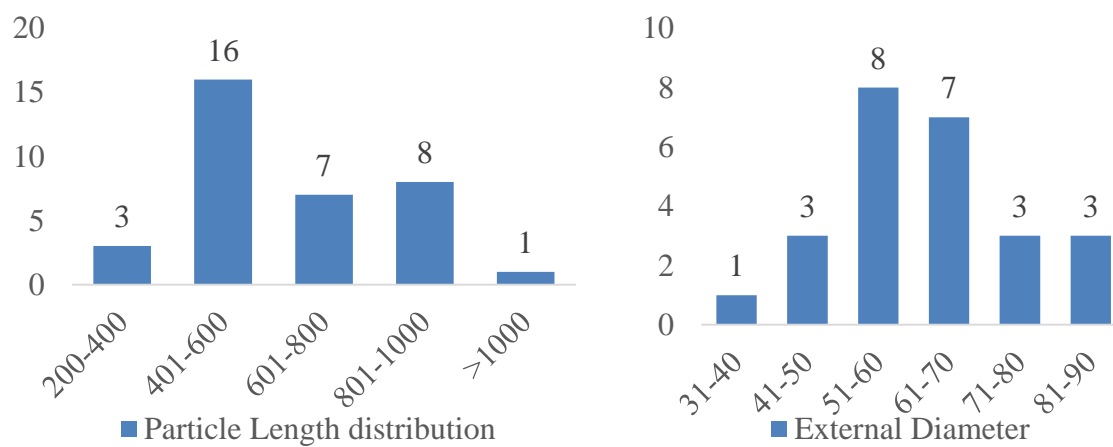


Figure 4-8: Bar graphs displaying the measured length and external diameter of normal “small” halloysite with average size being and 400-600µm in length and 50-70nm in diameter.

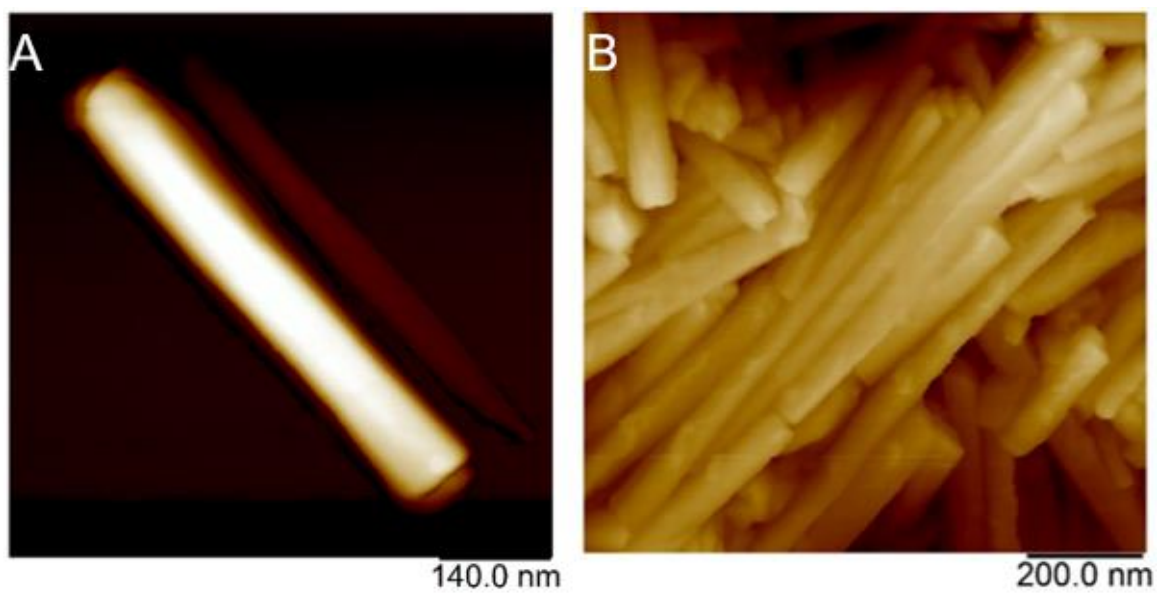


Figure 4-9: AFM images of “small” halloysite tubes displaying surface features (A-B).
Made by our collaborator Rawil Fakhrullin

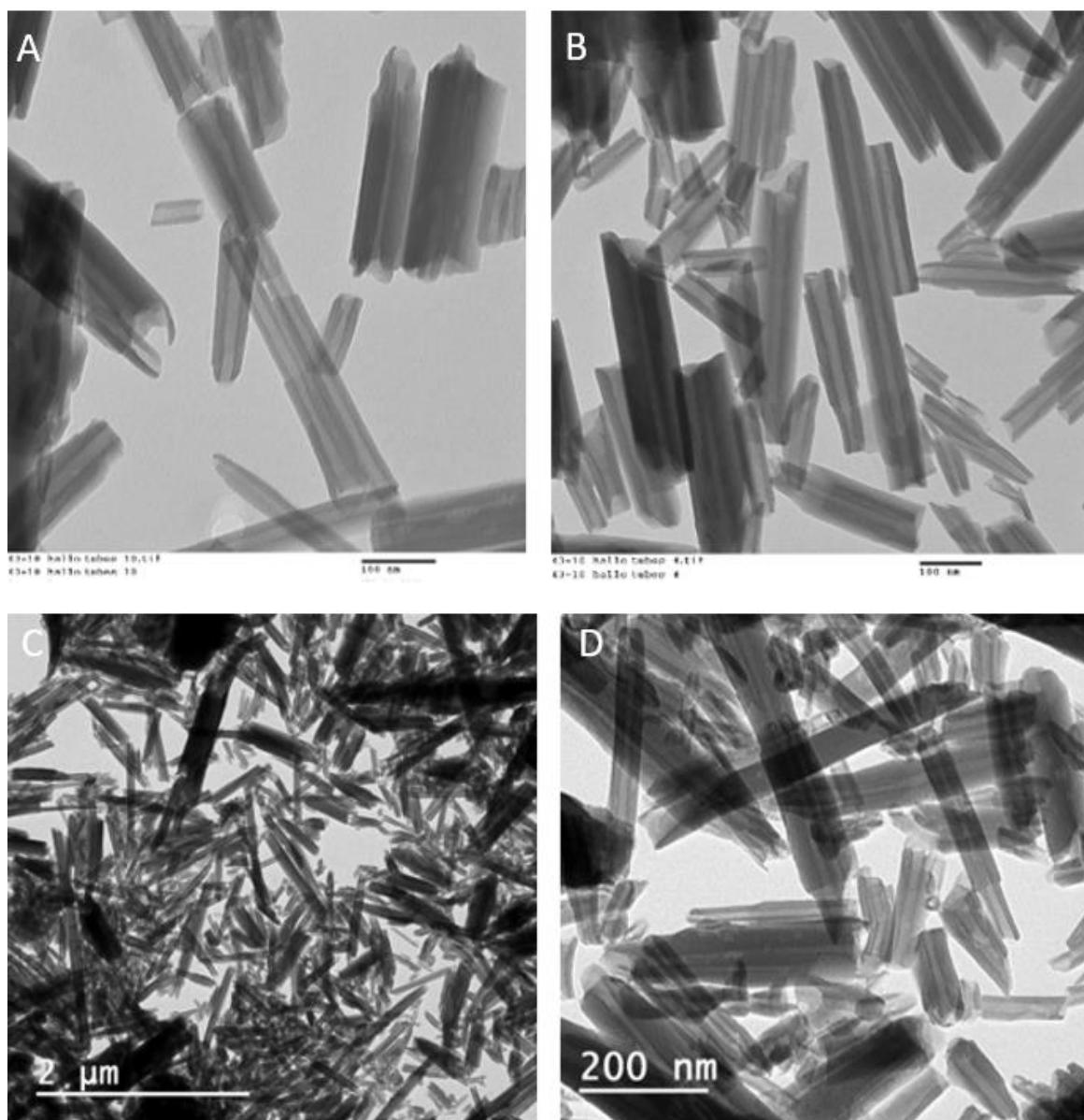


Figure 4-10: TEM images of small halloysite from Applied Minerals Inc displaying their size with respective scale bars (Sigma-Aldrich) (A-D). Made at Service Center, Arizona State University

Its effective hydrodynamic diameter is 460 ± 50 nm (as sizes averaged in all directions: width and length). Naturally, it is smaller than the tube length, and indicates good sample dispersion to single tubes. Contrary to “larger” halloysite (Figure 4-3), these “small” nanotubes were not resolved optically, and could not be seen in water dispersion.

These halloysite nanotubes have a zeta potential of 30 ± 5 mV which signifies its 2-3 hrs. of colloidal stability and its water dispersion at pH 6.5. Its water contact angle is $20 \pm 5^\circ$. A characteristic first X-ray reflection at $= 12.1^\circ$ corresponds to 0.74 nm aluminosilicate sheets packing periodicity in the nanotube walls (Figure 4-11).

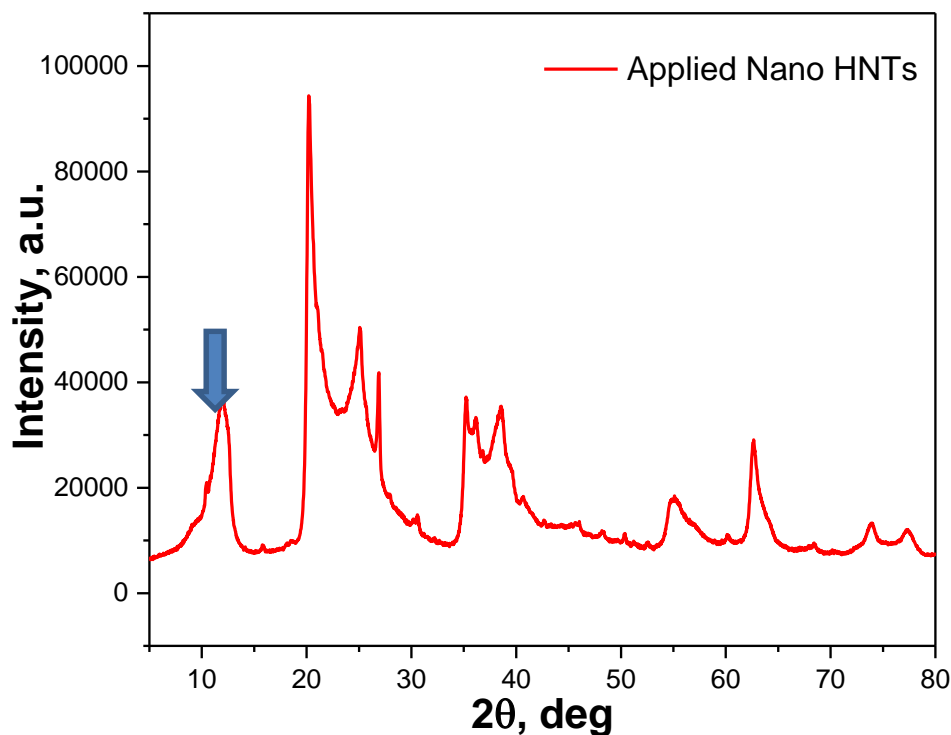


Figure 4-11: X-ray diffraction pattern from halloysite powder, wavelength 0.154 nm (Cu K_α radiation), characteristic halloysite peak is visible at $2\theta = 12.2^\circ$ indicated with an arrow

4.3 Selection of Larger Halloysite for Skin Application

Halloysite is usually used as a nanocarrier for invasive research in areas such as a carrier for cancer treatment. Whilst in less invasive research such as skin applications, these larger nanotubes could potentially be more effective due to their inner diameter being 20-22 nm. Allowing a greater amount of drug to be loaded inside as well as a more effective “torpedo” type of penetration into the skin (Figure 4-12). The goal is to be able to use these

halloysite nanotubes specifically for skin protection through sunscreen applications. Initial tests were done using pig skin due to their similar epidermal structure in relation to humans. The compound of choice is vitamin B-12. B12 is necessary for cell reproduction and can be applied topically for skin benefits due to its ability to reduce inflammation, dryness, and acne. It is sometimes used to treat conditions like psoriasis and eczema.

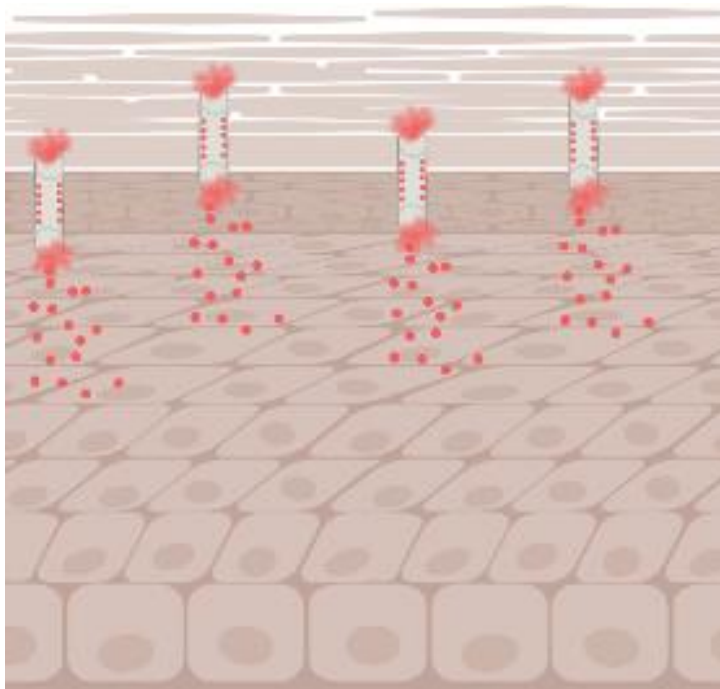


Figure 4-12: Scheme of “nano torpedo” halloysite penetrating pig skin and delivering vitamin B-12.

4.3.1 Halloysite and Vitamin B-12

Halloysite samples were prepared with vitamin B-12 through mixing, washing, and drying. The vitamin tablets were crushed with a mortar and pestle then mixed with pure halloysite powder at a ratio of 2:1 in DI water. This super saturated solution was then sonicated for 10 minutes and stirred at room temp. for 24 hours. The mixture is then washed twice through centrifugation at 4500 RPM for 3 minutes. Finally, the product is

dried for 24hr. using a vacuum desiccator. Loading analysis was done with thermogravimetric analysis (TGA).

Pig Skin Preparation

1. Thaw pig skin and bring to room temperature
2. Using a scalpel, cut ½x ½ inch square of skin
3. Turn on oven/incubator and calibrate to 37⁰C
4. Label baggies with test or control information
5. Set up controls and test materials using the table below

Controls:

- a. C1-Pig Skin – no cream or loaded HNTs, only diluent
- b. C2-Pig Skin – cream and diluents mixture, no loaded HNTs
- c. C3-Pig Skin – no cream, just diluents and loaded HNTs

Test Material: Pig Skin- cream, loaded HNTs in diluents

6. Arrange 24 squares of pig skin spaced evenly in a glass Pyrex Dish as shown above in the table
7. Prepare the Controls
 - a. C1 - Diluent is prepared by dissolving 0.85 g NaCl into 100mL distilled water
 - b. C2- Place 1.75 g cream and 0.25 g diluent into container and mix thoroughly
 - c. C-3 Place X mg of loaded HNTs into X mL of distilled water. Mix thoroughly.
8. Prepare the Test Material/formulation

- a. Dissolve X mg of loaded HNTs into diluents and mix thoroughly.
Add X mL of concentrated HNTs to X g of cream. Mix thoroughly.
9. Apply 0.25 grams of control or test formulation to the appropriate square of pig skin.
10. Using a gloved finger, gently rub the formulations into the skin as would be done with a face cream.
11. Immediately remove C1-C3 and Time 0 test square and place into respective baggies, Place them immediately in the freezer.
12. Place the Pyrex dish into the oven/incubator and begin the heating process.
13. Remove C1-C3 and test square at 30, 60, 90, 120 and 180 minutes. Place squares into their respective baggies and place them into the freezer.
14. When all 24 squares have been processed, ship them on dry ice for further analysis using bright field, phase contrast and fluorescence N21 channel microscopy.

4.3.2 Vitamin B-12 Encapsulation

TGA involves the burning of materials to determine weight change % at the relative temperature for the compounds involved. Based on the graphs shown in Figure 4-13 and Figure 4-14, it can be concurred that pristine halloysite burns at roughly 450-550°C and displays no change in weight for prior temperatures leading up to that point. In Fig4-8B we see a change in weight % at both 350°C and 550°C displaying roughly a 9.5 ± 1 wt % loading for the B-12 inside of the halloysite.

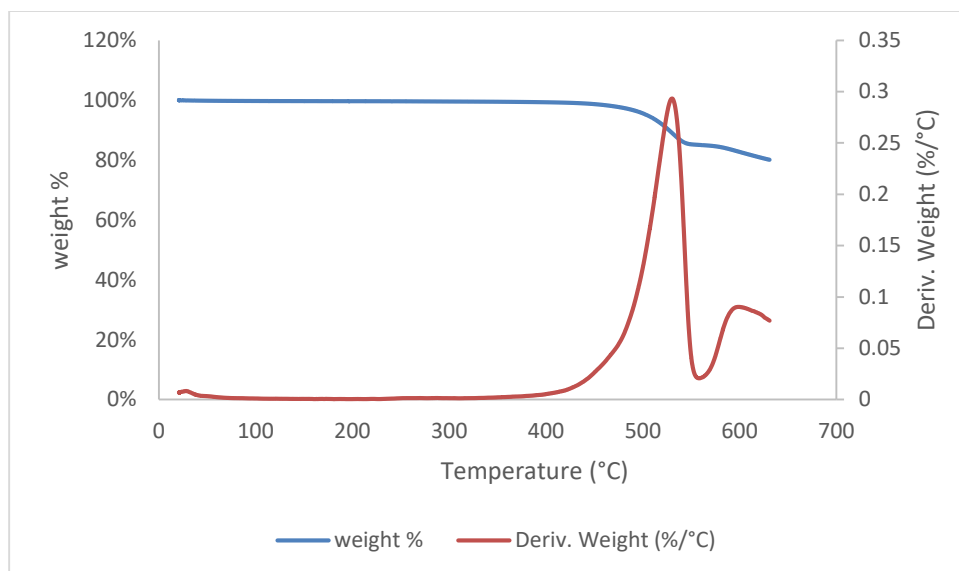


Figure 4-13: Thermogravimetric analysis displaying a negative control of pristine "large" halloysite. Where only the halloysite is present, undergoing a phase transition at 550° C

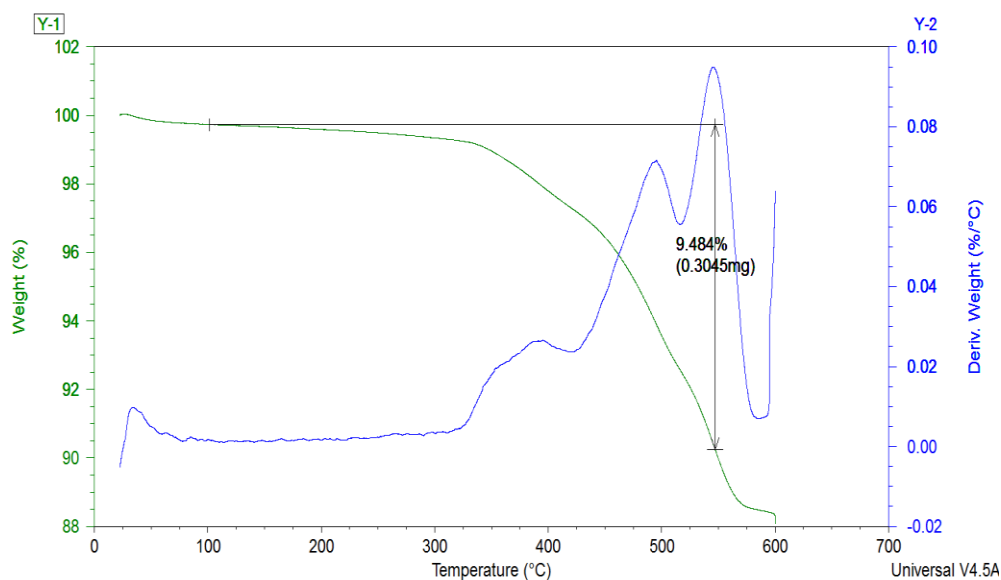


Figure 4-14: Thermogravimetric analysis of large HNT + B12, displaying a 9.5 % total loading percentage with the B-12 decomposed at 350° C and halloysite underwent a phase transition at 550° C.

4.3.3 HNT-B12 and Pig Skin Treatment

Using scanning electron microscopy, I was able to display that there were no halloysite on the surface of the skin after rubbing the halloysite formulation into the skin by massage. (Figure 4-15). Throughout the process of performing the experiments and analyzing data, the results of the actual pig skin remain inconclusive due to a multitude of factors. First, North Star declared proprietary property rights to these halloysite samples. Additionally, the ability to see halloysite penetration into the skin was not possible using the confocal microscope at LSUS nor the fluorescent microscopes here at Louisiana Tech. This was primarily due to an inability to receive access to the required systems and equipment to continue the project.

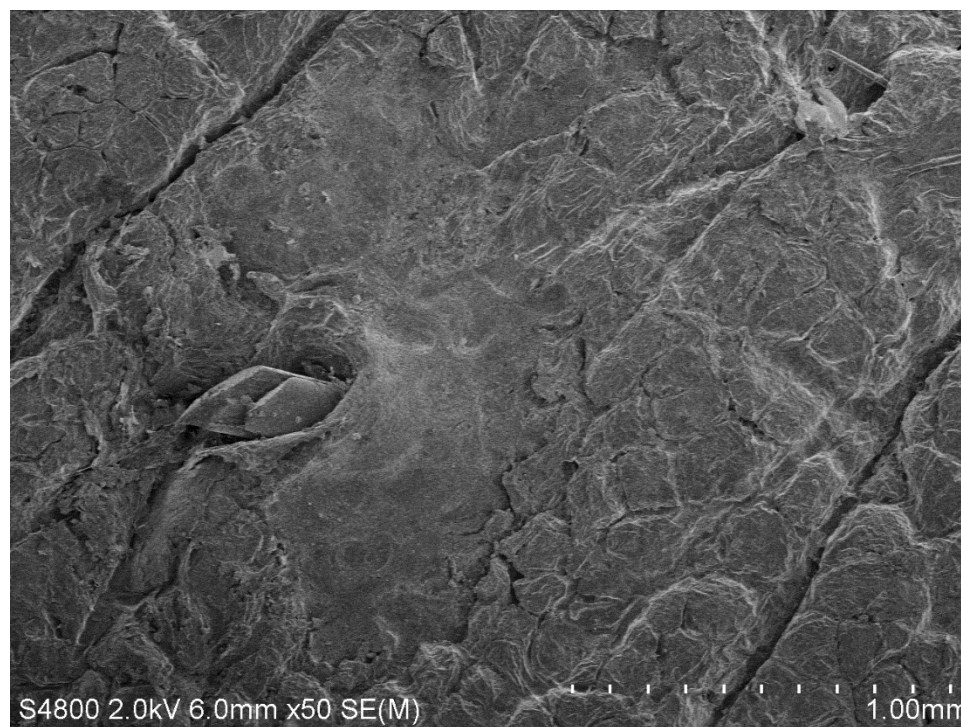


Figure 4-15: SEM image pig skin treated with 0.25g of HNT + B-12 displaying no nanotubes on the surface after massaging it onto the skin

4.4 Conclusions

For decades normal “small” halloysite has been used throughout the experiments of researchers. With this new HNT discovery a new question arises, we theorized if our results would improve if the nanotubes were larger in size. General electrochemical characteristics between both tubes were similar due to a similar composition (TGA, zeta-potential). The two types of halloysite could be visualized and analyzed with commonly used microscopy techniques (SEM, TEM, AFM) except for the newly discovered “larger” halloysite which has never been studied before until now. We could visualize these new tubules using dark-field microscopy which was accomplished by our collaborator Dr. Fakhrullin in Kazan University. This optical image proved the HNTs dispersibility nature and a never-before-seen view of the nanoparticle beautiful shape and separated in DI water. Whereas “smaller” halloysite displayed a diameter of 50 nm and 0.7 μm length and could not be seen in any optical microscopy technique. Halloysite always had the potential to be exploited over a broad range of applications. Due to the discovery of “large” HNT, the possibilities are truly endless. With our expertise, we determined that the “larger” tubes would be more effective for less invasive research. We decided to begin a skin protection experiment through potential sunscreen formulations and vitamin delivery. This was tested through the HNT encapsulation of vitamin B-12, a known skin protection agent. After mixing the tubes with a generic cream it was applied to pig skin to see possible effects of such “nano-torpedo” approach. Unfortunately, this work could no longer continue due to NorthStar Mine LLC claiming proprietary rights to this new halloysite for skin applications.

Therefore, we concentrated on drug delivery through the blood-brain barrier (BBB) in collaboration with LaTech Biomed research: N. Prajapati, Prof. M. DeCoster and Y. Yanamadala, Prof. T. Murray groups. In my next two chapters I will display the advantages of normal “small” halloysite “nano torpedo” type drug delivery in the blood-brain barrier by *vivo* and *in-vivo* experiments.

CHAPTER 5

TAGGED HALLOYSITE NANOTUBES AS A CARRIER

5.1 Tagged Halloysite Nanotubes as a Carrier for Intercellular Delivery in Brain Microvascular Endothelium and Model Two-Cell Brain Blood Barrier (Nano-Torpedo Approach)

We propose the use of “smaller” 0.7 μm length halloysite tubes to penetrate the blood brain barrier (BBB) and effectively deliver the payload over an extended time period. We characterized a delivery mechanism by the nanotube encapsulating rhodamine isothiocyanate dye and then ionomycin drug into brain microvascular endothelial cells. Then a model membrane was developed with set up across 0.4- μm pore polystyrene transwell support covered by sequential seeding endothelial and astrocyte cells to mimic the blood brain barrier, and HNT through-delivery was analyzed. In this work, I did all halloysite formulations and preparation of model BBB membranes and helped in other cell experiment to N. Prajapati and A. Karan from Dr. DeCoster laboratory which resulted in our joint published papers: *Frontiers in Bioengineering Biotechnology*, v.8, 451, 2020 [75] and *Clays & Clay Minerals*, v.69, 603-611, 2021 [76] which partially used in this chapter with proper referencing.

5.2 Preview

Roughly one in six people suffers from various types of neurological disorders across the world, and up to 7 million premature deaths occur each year. Brain diseases affect people’s way of life negatively through seizures which cause irregular behaviors.

Millions of people suffer from epilepsy, making it one of the most common types of brain disorders. The current treatment of epilepsy is poor due to the lack of availability of antiseizure medication and its lack of effectiveness. Current medication has various side effects such as dizziness and difficulties with speech. Utilizing nanotechnological formulations to treat the disorders could lead to a cure for up to 70% of diagnosed patients [77-80]. Dopamine and gamma-amino-n-butyric acid are brain neurotransmitters that are important when researching brain disorders such as epilepsy; ionomycin allows the calcium response in brain membrane cells to be followed.

Brain microvascular endothelial cells (BMVECs) are the key cells in the blood–brain barrier, which is the multicellular membrane between the brain’s blood vessels and a brain tissue. BMVECs constitutes the tight junction proteins which prevent the entry of pathogens and other toxic substances into the brain, but it also prevents most potential drugs against neurological and mental disorders to cross the barrier and readily reach into the brain tissue [81]. In this work, we studied halloysite nanotube penetration into primary rat BMVECs, which are the main cell type that prevent entry of drugs through the blood–brain barrier. We demonstrated with fluorescent rhodamine B isothiocyanate dye that halloysite binds on the cell, penetrates the cell interior, concentrates around the nuclei, and may deliver a drug load. Next, we developed a model for brain cell stimulation using halloysite loaded with ionomycin, a widely used Ca^{2+} ionophore [82-85] to monitor calcium transport across membrane and to stimulate a response from brain cells. Ionomycin-HNT formulations resulted in intracellular delivery, which was monitored by Ca^{2+} changes in the cells, showing gradual and prolonged delivery of ionomycin into the brain endothelial cells. An outline in Figure 5-1 displays the

progressive change in calcium signals throughout the stimulation, proving halloysite formulations have the potential as an efficient carrier for drugs or selected neurotransmitters (glutamate) targeted for brain disorders treatments.

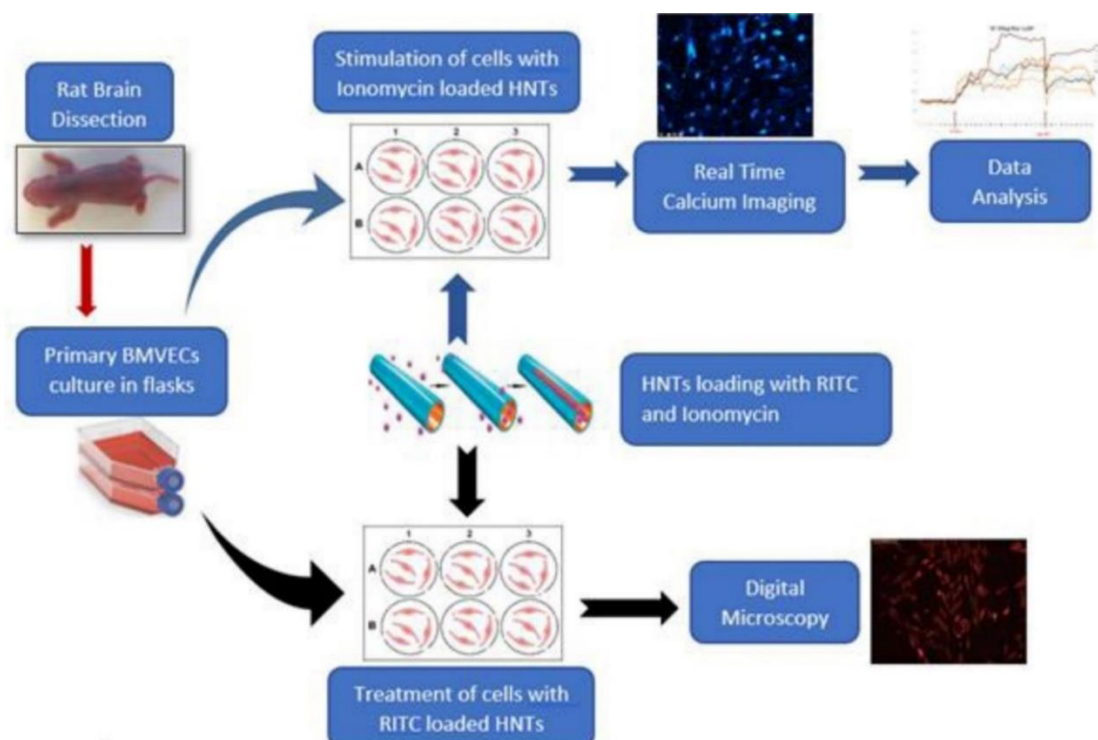


Figure 5-1: Loading clay nanotubes with fluorescent rhodamine (RITC) and ionomycin and treating the endothelium cells with the loaded nanotubes. Ionomycin-HNT upper route with Ca^{2+} imaging monitoring and RITC – lower route accomplished with visualization [75]

In the current work, the penetration of HNT nanotubes into primary rat endothelial cells (BMVECs), the main cell types which prevent the entry of drugs through the blood–brain barrier, were studied [86-89]. In addition, a model was developed showing the interaction of tagged HNT with the endothelial lining by layering the cells on a porous membrane in transwell inserts. This was done using fluorescent rhodamine isothiocyanate dye, where HNT binds on the cell, penetrates the cell interior, concentrates around the nuclei, and may deliver a drug load. The HNT/brilliant green

formulations with intracellular delivery allowed the preferable elimination of human lung carcinoma cells (A-549) as compared with hepatoma cells due to different intracellular penetration [39]. The transwell assay is used widely to study the absorption in the intestine of molecules administered orally [89-93]. The development of an *in vivo* membrane system to mimic *in vitro* and analyze the transport of loaded HNT tubes across the model (endothelial and astrocyte cells) blood–brain barrier was challenging. Transwell inserts were utilized with a porous polycarbonate membrane which acts as a chamber where a confluent layer is formed on top of astrocytes. The membrane nanotube permeability and the ability to visualize the multilayered cells were realized through non-inverted confocal microscopy (Figure 5-2).

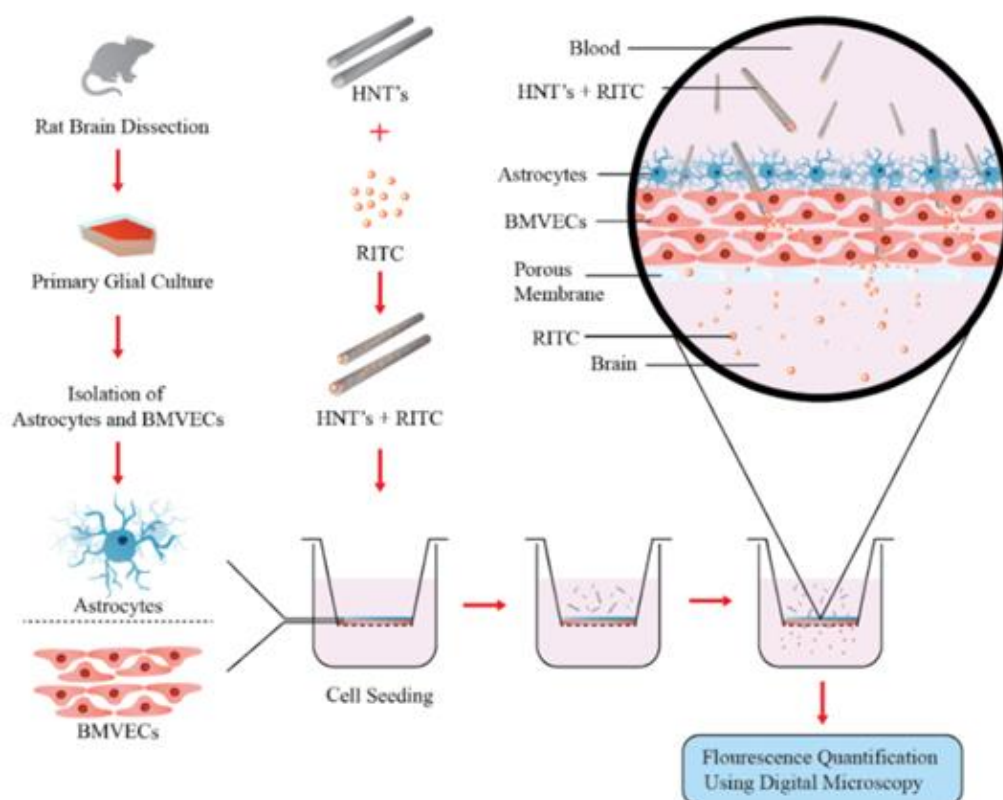


Figure 5-2: A co-culture model of brain endothelium and astrocyte membrane developed for testing the penetration and delivery of HNT nanotubes and their payload (RITC) across the blood–brain barrier model [76]

Halloysite was purchased from Sigma Aldrich, St. Louis, Missouri, USA and used without further purification. Rhodamine B isothiocyanate and ionomycin were also obtained from Sigma Aldrich. For system analysis, scanning and transmission electron microscopes were used (EDAX-SEM, Hitachi-S4800, Tokyo, Japan, and TEM, JEM-2100, JEOL, Japan) as well as thermogravimetric analysis (TGA, Thermal Advantage Q50, New Castle, Delaware, USA), UVVis spectrophotometry (Agilent 8453, Santa Clara, California, USA), fluorescent and laser confocal optical microscopy (Leica DMI 6000 B inverted microscope and Nikon A1R Confocal and Super Resolution System, Allendale, New Jersey, USA). A ZetaPlus Instrument (Brookhaven Instruments, Holtsville, New York, USA) was used to determine the system's surface charge. endothelial growth medium (Cell Applications Inc., San Diego, CA, USA), containing 6% rat endothelial growth factor, to obtain pure endothelial (BMVECs) culture [78,79]. The astrocytes were purified by subculturing the glial cells in Ham's F-12K medium with 5% FBS and 5% horse serum and washing off the overlying microglial cells regularly before subculturing. The purity of each culture was determined by staining the cells against their specific markers, glial fibrillary staining against astrocytes, and Von Willebrand factor staining against endothelial cells [81].

5.2.1 Halloysite Loading with Rhodamine Isothiocyanate Dye, and Ionomycin, and Neurotransmitters

Halloysite samples were prepared by loading rhodamine B isothiocyanate (RITC) and ionomycin through stirring, centrifugation, and sonication at various ratios including 10 mg halloysite/1 mL DI water per 0.5, 1, and 2 mg of RITC. The solutions were then sonicated and vortexed for 1 min, then mixed on a stir plate for 24 h at room temperature. The mixture was washed once by centrifugation at 2500 RPM for 2.5 min and then dried

at 70°C for 24 h. When loading ionomycin, 20 mg of pristine halloysite clay nanotubes were stirred with 1 mM ionomycin for 24 h. The mixture was then washed with sterile water by centrifugation 2500 RPM for 3 min one time. The solution was then freeze dried for 20 min and placed in a vacuum for 24 h to remove the excess solution. Samples were then characterized by the zeta potential analyzer, which displays the surface charge and thermogravimetric analysis, allowing us to calculate the loading percentage. The procedure for neurotransmitter is accomplished by taking 50 mg of etched or pristine halloysite with 50 mg of glutamic acid separately in 5 mL of DI water, creating a super saturated solution through sonication for 5 min and stirring for 24 h at room temperature. The last step is for the suspension to dry in the oven for 24 h at 70°C. After loading the halloysite samples were characterized through zeta potential analyzer and thermogravimetric analysis to determine a surface charge and measure the percentage of material loaded.

5.2.2 Cell Culture

Primary brain microvascular endothelial cells (BMVECs) were obtained directly from the rat brain cortex. Rat pups, 1 or 2 days old were euthanized to obtain the rat brain cortex. The cortex obtained by dissection of the pup's skull is cleared out of meninges under the microscope. The cortical tissue thus obtained was then treated with trypsin and triturated, with the process repeated at least three times to break the brain tissue into cells. After each trituration, cells were incubated at room temperature under sterile conditions for about 10 min and supernatant was collected in a 15 mL tube. The collected supernatant was then centrifuged to obtain a pellet of mixed culture of brain cells. BMVECs were isolated from this primary culture by treating them with 5.5 μ M of

puromycin dihydrochloride to kill all other cell types except the endothelial cells as shown in Figure 5-3. Endothelial cells are encoded with a puromycin N-acetyl transferase gene (PAC gene), which confer resistance to the action of puromycin [94,95]. Thus, isolated BMVECs were then cultured in vitro at 5% CO₂ and 37°C in rat endothelial growth medium (Sigma Aldrich). The cells were characterized by staining them against Von Willebrand Factor (VWF), Figure 2B, an essential blood clotting protein specific to endothelial cells [96].

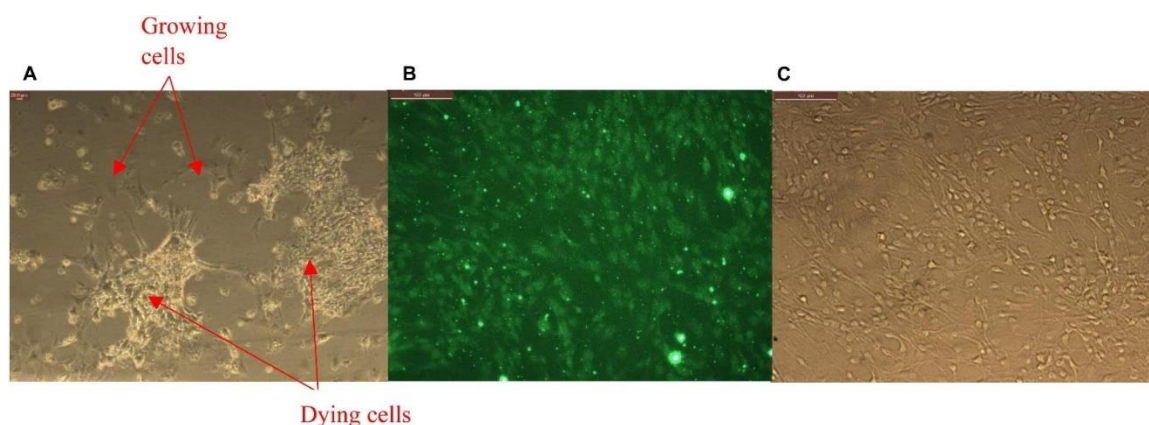


Figure 5-3: (A) Primary glia treated with puromycin for isolation of brain microvascular endothelial cells (BMVECs) showing killing of all other cell types except the BMVECs. (B) Primary BMVECs characterized by staining against VWF using fluorescence microscopy, and (C) phase image of stained cells. Magnification 200X, scale bar = 200 µm. [75]

5.2.3 Treatment with Rhodamine Isothiocyanate (RITC) Loaded Halloysites

Brain microvascular endothelial cells between primary passages of 3 and 7 were used for the experiments. Cells were plated in 48 well cell culture plates at 10K per well density and treated with RITC loaded halloysite, halloysite alone (negative control) and RITC alone (positive control) at 50–70% confluency. Cells were treated with 10 µg/mL of halloysite alone (negative control) and 10 µg/mL of halloysite loaded with RITC [for

all nanoclay samples loaded with different concentration of RITC (1:5 and 1:10)]. The concentration of RITC alone was chosen to correspond to the loaded halloysite formulations. A release profile of the RITC loaded halloysites was conducted Using 10 mL of endothelial media, 3.3 mg of HNT-rhodamine was taken and stirred at 250 rpm for 24 h. Readings were taken after 1, 4, 8, and 24 h.

5.2.4 Brain Microvascular Endothelial Cells (BMVECs) Stimulation Using Ionomycin Loaded Halloysite

Primary BMVECs were plated at the density of 10K per well in 48 well plates. At the confluency of 70 to 80% each well-containing the cells were loaded with 500 μ L of Fluo-3 AM loading solution, i.e., Lockes' solution with Fluo-3 AM dye (1:500) and pluronic acid (1:1000) [97]. The cells were treated with this solution for 1 h at 37°C, in a 5% CO₂ incubator and then – with 500 μ L of recovery solution for 1 h. The recovered cells were then stimulated with halloysite loaded with ionomycin (10 and 50 μ g/mL), halloysite alone (50 μ g/mL), ATP 100 μ M, and ionomycin 1 μ M at different instances depending on the experiment. Real time intracellular calcium (Ca²⁺) change due to ionomycin transport across the system was recorded by capturing images every 4 s with InCyt Im1 software on the imaging system. The images were then used for Ca²⁺ signal analysis, which utilizes change in fluorescence intensity as the function of time as a measure for quantifying calcium changes in cells.

5.2.5 Development of the in vitro Co-Culture Model on Transmembrane

Astrocytes were plated at a density of 20,000 cells per well onto the cell-culture inserts (Thermo Fisher Scientific) with a porous polycarbonate (PC) membrane of 0.4- μ m pore diameter and grown at 37°C in 5% CO₂ in humidified incubators. At 50–70% confluency, endothelial BMVEC cells were seeded on top of the astrocytes at 20,000

cells per well to ensure the bilayer organization. The development of a confluent bilayer of endothelial and astrocyte cells was determined by using confocal microscopy.

5.2.6 Visualization of HNT-RITC Uptake and Diffusion Across the Two-cells Barrier

A concentration of 20 $\mu\text{g}/\text{mL}$ of HNT-RITC formulation was added to the cell inserts without cells (media alone), to cell inserts with a monolayer of endothelial cells, and to inserts with a bilayer of endothelial and astrocyte cells developed on the porous membrane. The concentration was tested in two separate passages of cells in triplicated wells. HNT-RITC formulations were added on top of the cell bilayer. Images of the solution beneath the cell culture inserts were taken using a Leica DMI 6000 B inverted microscope (LEICA Leica DMI 600 B, Allendale, New Jersey, USA) at intervals of 4 and 24 h, after the addition of the material. The images were checked for penetration of the nanotubes and fluorescence intensity due to diffusion of RITC from HNT across the membrane to the solution in bottom wells. The fluorescence intensity for the images at the two time points was quantified using MATLAB to compare the diffusion across the barrier with the control wells (inserts) without cells.

5.2.7 MTT Assay

An MTT (3-(4,5-dimethylthiazol-2-yl)-2,5-diphenyl tetrazolium bromide) assay was performed to compute cell metabolism as a measure of cytotoxicity, as described previously [98]. Cells were cultured in 48-well culture plate at 37°C and 5% CO₂ in humidified incubators. The cells were then treated with various concentrations of HNT-RITC when their confluency reached 60–70%. The control wells received media with no materials. After 24 h of treatment, MTT (1.25 mg/mL in RPMI media) was added to the cells and incubated for 1 h at 37°C. The absorbance of the resulting formazan crystals

dissolved in 90% isopropyl alcohol was read at 570 nm. Cytotoxicity was computed by comparing the absorbance of HNT-RITC-treated wells with the control wells.

5.2.8 Halloysite Release Profile

The loaded HNT samples that were used to treat the endothelial cells were tested for RITC release kinetics (Figure 5-4 and Figure 5-5). This displays the rate at which the dye is released over a period of 24 h. The results showed that rhodamine is released in an initial burst of ~25% within the first 1 h, which is an expected characteristic when utilizing nanocontainers. This caused no stress to the endothelial cells. During a further period, the advantages of HNT tubes began to become apparent, i.e., by releasing the dye slowly over a period of 24 h at a steady rate (releasing the remaining 75% over the next 23 h). The delivery process avoids major spikes that could stress or kill the cells. The nanotubes penetrated cell nuclei during both time point experiments at 30min and 24h experiment in Figure 5-4 and Figure 5-5. The red dots which represent the loaded HNT were confined within the cells; although they are extremely dim in these pictures, the visualization of drug release begins.

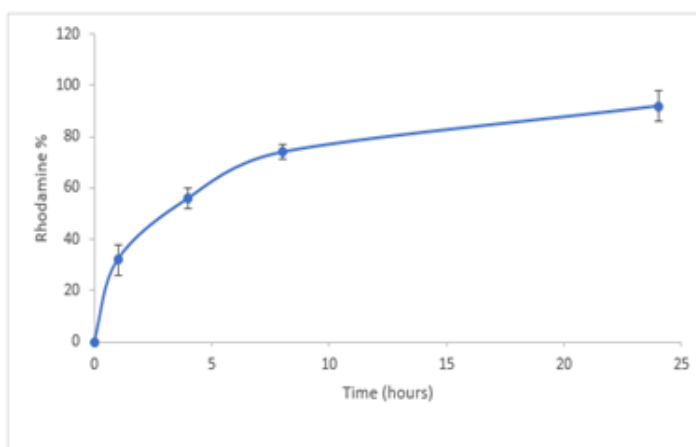


Figure 5-4: Release profile of rhodamine isothiocyanate-RITC loaded into HNT taken at 555 nm

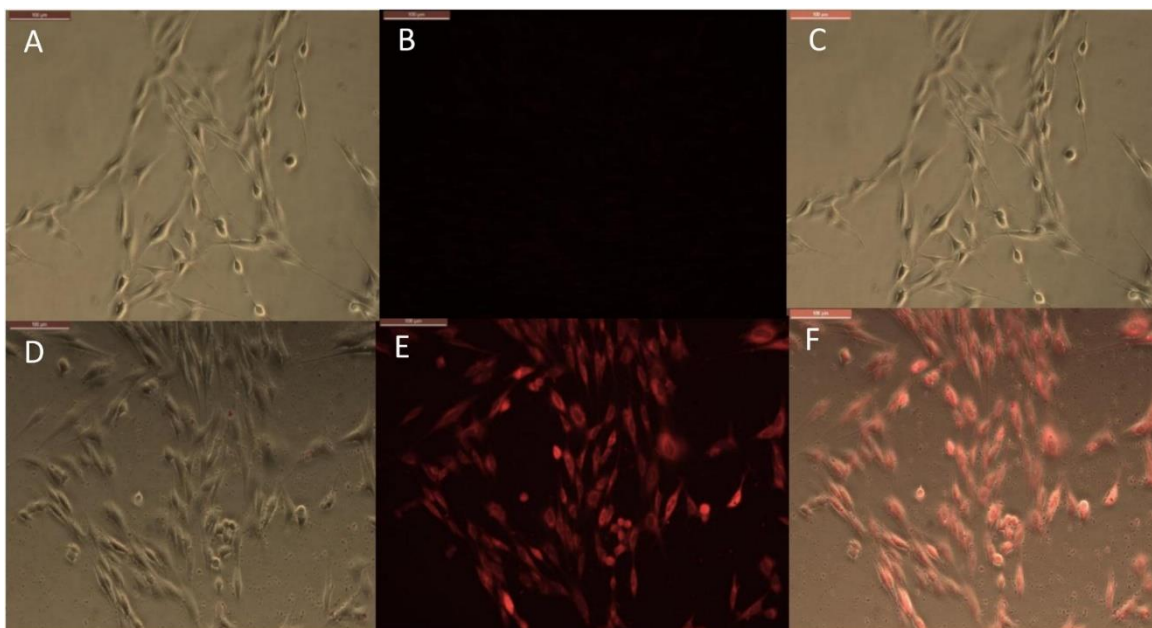


Figure 5-5: Phase and fluorescence imaging of primary brain endothelial cells treated with RITC only (A, B), and with halloysite clay nanotubes loaded with RITC (D, E) after 30 min exposure. Merged images for the phase and fluorescence settings (C, F). Magnification 200X, scale bar = 200 μm [75]

5.2.9 Intracellular Rhodamine Isothiocyanate (RITC) Delivery with Clay Nanotubes

An observation of halloysite binding and penetration into the endothelial cells was visualized as red fluorescence concentrated within the cells, Figure 5-4. The addition of only RITC dye did not color the cells interior within 30 min of treatment; while the dye loaded halloysite bound or penetrated the cells and started releasing the dye inside the cells, coloring them red. Within a 4-h time frame RITC and RITC-HNT both showed cells with more fluorescence compared to the same samples in the 30 min exposure time. Furthermore, RITC-HNT formulations displayed greater fluorescence compared to RITC only, proving the dye delivery into the cells.

The timeframe of these images is 30 min after delivery of both samples (RITC and HNT + RITC) to the cells, with a concentration of 10 $\mu\text{g}/\text{mL}$ for HNT + RITC and 2

$\mu\text{g/mL}$ of RITC alone. The loading of RITC in HNTs was 20 wt.%, thus making the same amount of RITC added to the samples. The small bright dots found in the bottom images of Figure 5-5E, are the aggregated halloysite tubes that contain RITC. HNT-RITC aggregation is displayed mostly along the cellular membrane and inside the endothelial cells as indicated by nuclear exclusion.

Therefore, halloysite nanotubes are highly capable of encapsulating, transporting, and slowly releasing the dye (or drugs as we will show with an example of ionomycin) over a few hours. It is important to note that we did not modify the surface of the halloysite with any type of polymer or silane coating. Figure 5-5B displays RITC alone added at the same concentration showing a much dimmer visualization of the cell's responsiveness to this non-encapsulated dye.

Results for the 24-h treatment were similar with more profound fluorescence in both conditions but RITC loaded halloysite delivered more dye into the cells at every period as compared to just the dye alone, Figure 5-6B. Images at a time point of 24 h displayed the nanotubes distribution more evenly over the cell interior, still contained within the cell body Figure 5-6E. One could see that RITC-HNT concentrated in some smaller spots of ca 1 μm diameter, which may be the nuclear surrounding, as it was found for MCF-7 cells treated with halloysite [67]. Throughout the trials, we detected a nuclear exclusion, extended length of fluorescence, and that the tubes did not stress or kill the cells. The clay nanotubes are displayed as small dots in Figure 5-6E and are brighter than the dye spread inside the cells. The merged image (Figure 5-6F) of phase and fluorescence settings (Figure 5-6D, E) for cells treated with HNT-RITC gives a clear picture of the localized nanotubes with red dye in the cell cytoplasm with distinct nuclear

exclusion, which displays greater binding and aggregation of the tubes on the cell surface in 24 h compared to the 30 min treatment. After cell fixation (4 days), we see that cells treated with dye only was washed away with only minimal fluorescence remaining on the cells. While the HNT-RITC treated cells still showed significant fluorescence indicating a prolonged delivery of the dye from the clay nanotubes. Figure 5-4 G, H show that the cells treated with halloysite nanotubes alone (negative controls) do not show any fluorescence by themselves.

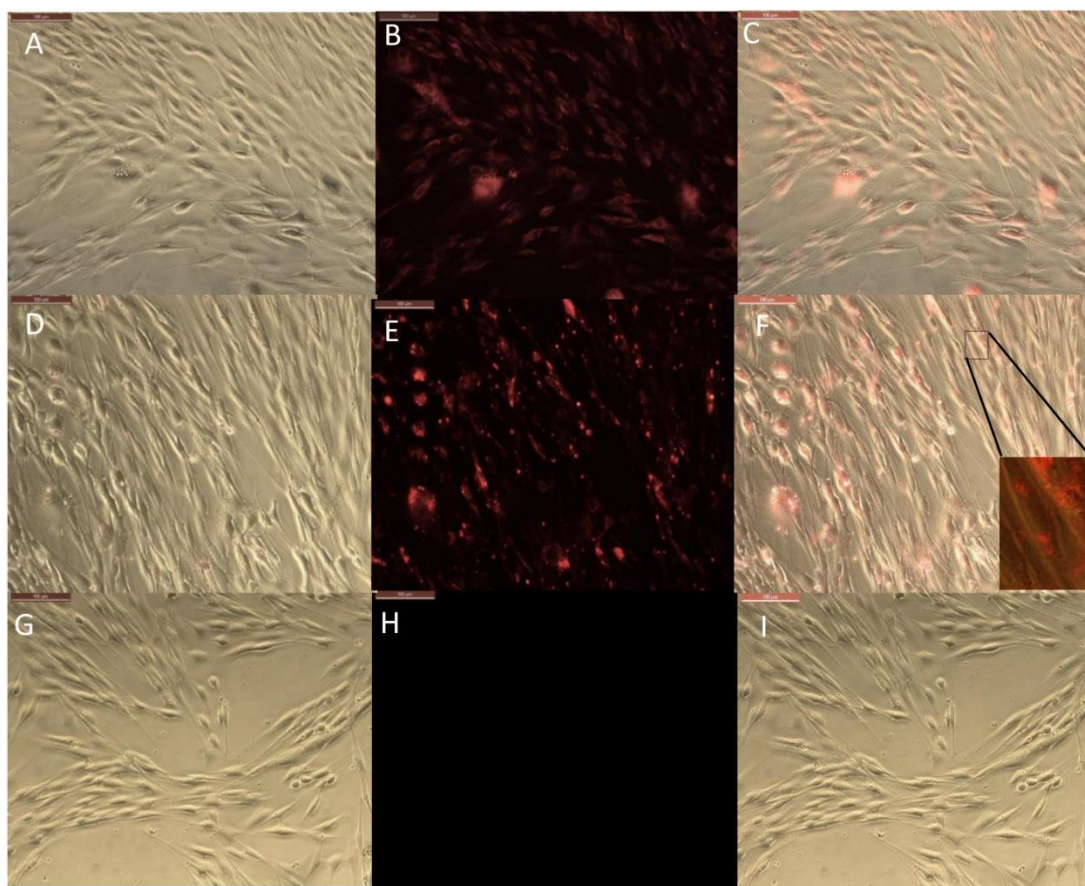


Figure 5-6: Phase and fluorescence microscopic imaging of primary endothelial cells that were treated with RITC only (A, B), treatment with HNT-RITC formulations (D,E), and treatment with HNT only (G,H) in both phase (right) and fluorescent (middle) settings for 24 h exposure. Merged images for the phase and fluorescence settings (C, F, I). Magnification = 200X, scale bar = 100 μ M [75]

The fluorescence images (middle) highlight nanotubes or dye localization in the outer region of the cell networks, while the merged images (left) illustrate a clear picture of materials (nanotubes and dye) localization inside or on the cell surface.

5.2.10 Halloysite Loading with Rhodamine Isothiocyanate Dye, and Ionomycin

Thermogravimetric analysis (TGA) was used to determine the sample's weight change during the component burning (Figure 5-7 and Figure 5-8) and demonstrated that the material or substance was loaded inside the nanotubes and gave an approximate percentage of the amount loaded. The TGA analysis (Thermal Advantage Q50, New Castle, Delaware, USA) was done using pristine hnt with a major phase transition at 490°C, with some nanotubes loaded with RITC, and others loaded with ionomycin. The difference in mass decrease during heating between pristine and loaded hnt gave an estimated RITC loading of 5 ± 1 wt.%. A similar analysis for ionomycin drug loading into the nanotubes gave values of 14 ± 1 wt.%, indicating some external drug attachment. Glutamic acid has a negative charge and being loaded into the tube's lumens demonstrated weight percent change of 3.4 ± 0.2 wt%. The results showed that, compared to pristine hnt, an ionomycin loading of ~8 wt.% was achieved. (Figure 5-6).

negative drug molecules into the positive lumen of nanotubes. The pristine halloysite had a zeta-potential value of -30 ± 2 mV and after the drug loading, it became -45 ± 1 and -48 ± 2 mV correspondingly for ionomycin, glutamic acid, and rhodamine. These formulations provided an enhanced colloidal stability that took 3–4 h for settling for pure halloysite and 8–10 h in the loaded samples. The precipitation time for aqueous unloaded and loaded halloysite ranged from minutes to days, in correspondence to the respective zeta-potential that were measured. Therefore, the ability to load neurotransmitters into clay nanotubes is achievable but further testing on the surface area and inner lumen with the substances needs to be performed to know their exact location along with in vitro testing.

These results demonstrate that one can sufficiently load selected brain drugs into halloysite nanotubes and deliver them into the cells in a manner like the procedure of loading RITC. Furthermore, we will concentrate on the analysis of ionomycin delivery because we have a well-elaborated method to characterize the drug release kinetics with Ca^{2+} analysis.

5.2.11 Delivery of Ionomycin – Halloysite Formulations into Endothelial Cells (Ca^{2+} -Analysis)

In real time calcium imaging, we observed that the cells response to ionomycin had a spiked increase in Ca^{2+} which decayed quickly due to clearance by cells as shown in baseline (Figure 5-6A). When we used halloysite alone, there was only a small response (Figure 5-6B). When ionomycin was encapsulated with halloysite, we achieved a higher response of Ca^{2+} for the same concentration (1 μM) loaded that was also used for the control resulting in a gradual rise in Ca^{2+} which remained higher for a longer time until it was diluted by the addition of any other stimuli. This increase of Ca^{2+} indicates

the gradual and prolonged transport of ionomycin through halloysite across the cell membrane (Figure 5-6B, C). Each experiment was ended with ionomycin stimulation to ensure that the stimulus did not kill the cell under observation. To ensure that the cells were healthy and responding normally to other physiological stimuli, cells were tested with ATP, a well-known stimulator for BMVECs. Ionomycin is a well-known antibiotic and has been also known to induce cancer cell death and proliferation. Results showing sustained delivery of ionomycin might suggest a potential application of these formulations for cancer treatment [99-101].

All cells were stimulated with ionomycin at the end of experiment (B-E), except (A) which was stimulated by HNT-ionomycin of 50 $\mu\text{g}/\text{mL}$. This demonstrated that the cells were still responsive to Ca^{2+} changes, ensuring no cell death, and avoiding occurrence of false signals during the experiments.

Ca^{2+} peak analysis presented in Figure 5-8 allows us to come to following conclusions: stimulation by ionomycin (positive control) shows an instant peak of Ca^{2+} that decays quickly compared to HNT-ionomycin nano capsules (50 and 10 $\mu\text{g}/\text{mL}$) which shows a gradual influx of Ca^{2+} and higher delivery of ionomycin in the cells for both concentration (Figure 5-9A, B). Cells that responded to ATP showed a significant peak that is normally observed for physiological conditions (Figure 5-9C). Stimulus by halloysite alone produces a slight Ca^{2+} response, which was much less compared to HNT-ionomycin formulations with the cells showing no visible toxicity as well as remaining active afterward.

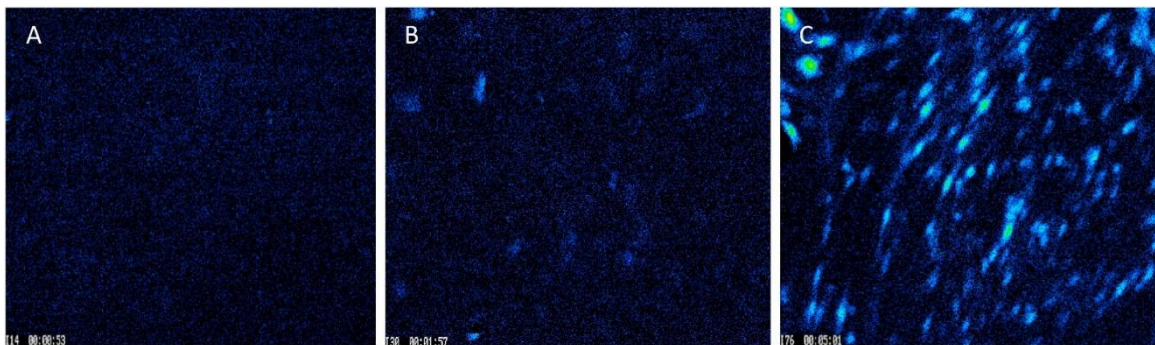


Figure 5-9: Images captured for BMVECs during Ca^{2+} treatment: (A) before stimulation; (B) peak stimulation by 50 $\mu\text{g}/\text{mL}$ of empty halloysite nanotube, and (C) peak stimulation by 50 $\mu\text{g}/\text{mL}$ nanotubes loaded with ionomycin. Magnification = 200X [75]

5.2.12 Statistical Analysis of Calcium Response to Different Stimuli

The graphs in Figure 5-10 show signals obtained for only 5 cells for each condition for simplification and clear representation of the data. The number of cells captured per frame for a condition being tested in an experiment acted as a region of interest, and it ranged from 41 to 140 cells. After obtaining the calcium signals for different stimulations, the Ca^{2+} fluorescence intensity data as a function of time are used to extract the percentage of peak Ca^{2+} response above the baseline (Figure 5-10B) and the cells that responded to the stimuli (Figure 5-10C). The time taken for the stimuli to reach the peak response (Figure 5-10D) was also extracted. The bar graphs are obtained by averaging the values over the region of interest from each condition used for the experiment. At least five conditions were tested here, three times. Overall, the number of cells analyzed was 1,232 for all wells and conditions reported for calcium imaging.

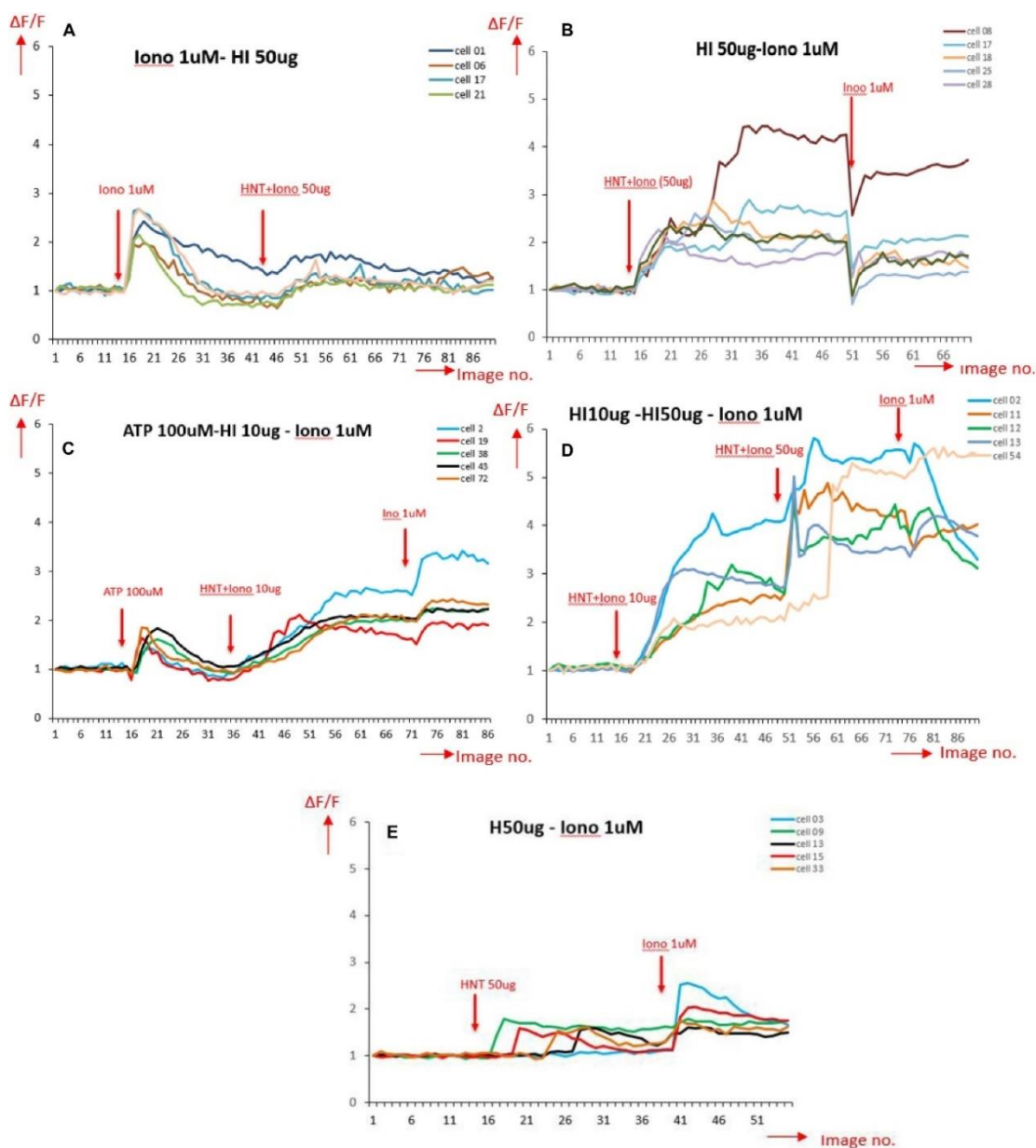


Figure 5-10: Ca^{2+} peak intensity obtained for different stimulation on BMVECs, in the horizontal axis is the image number indicating time periods with total range of 4 s each (1 image no. = 4 s); and in the vertical axis is the normalized values for fluorescence intensity corresponding to calcium activity (A) stimulated by ionomycin (Iono) 1 μM (positive control); (B) stimulated by 50 $\mu\text{g}/\text{mL}$ HNT- ionomycin (sample tested); (C) stimulated by ATP, a well-known Ca^{2+} stimulator (positive control indicating healthy cells), followed by HNT-ionomycin formulation (10 $\mu\text{g}/\text{mL}$) showing the comparison between the Ca^{2+} responses of physiological stimulation (ATP) and HNT-ionomycin formulation for the same cells. (D) Cells stimulated by 10 and 50 $\mu\text{g}/\text{mL}$ of HNT-ionomycin showing comparative results for the cells when stimulated by lower and higher dose of HNT-ionomycin; (E) stimulated by 50 $\mu\text{g}/\text{mL}$ of empty HNTs (negative control). [from our paper 75]

One can see that the calcium peak response above baseline gave us an idea of how high the calcium response to a stimulus is. The results (Figure 5-10B) show that the increase in peak calcium response above the baseline was 120% for HNT-ionomycin (50 $\mu\text{g}/\text{mL}$), and it was greater than for ionomycin alone (positive control) at $82 \pm 2\%$.

The halloysite (negative controls) showed a slight Ca^{2+} response, which was insignificant at 16% compared to the high response of 94% for the same concentration of the HNT-ionomycin samples. The results that the nanotubes alone can also produce much smaller 16% peak Ca^{2+} response suggest us that there is some form of advantageous cellular interaction and communication between the nanoclay and endothelial cell networks which is served by the signaling molecule, calcium. For ATP stimulation the signal was 40%. The peak response to ATP showed that the cells were healthy and at normal physiological condition.

Each experiment had different numbers of cells giving rise to different regions of interest. Figure 5-11C represents the percentage of cells that responded to the given stimulus in an experiment. One can see that a higher number of cells responded to the HNT – ionomycin formulation with 97% for concentration of 10 $\mu\text{g}/\text{mL}$ and at 92 % for 50 $\mu\text{g}/\text{mL}$, while it was 65 % for 50 $\mu\text{g}/\text{mL}$ halloysite alone, 72% for 1 μM ionomycin, and 76 % for 100 μM ATP. This result indicates that all the parameters discussed here are supported by a high response of cells, but the data specifically displays a higher value in the loaded samples compared to the other conditions tested.

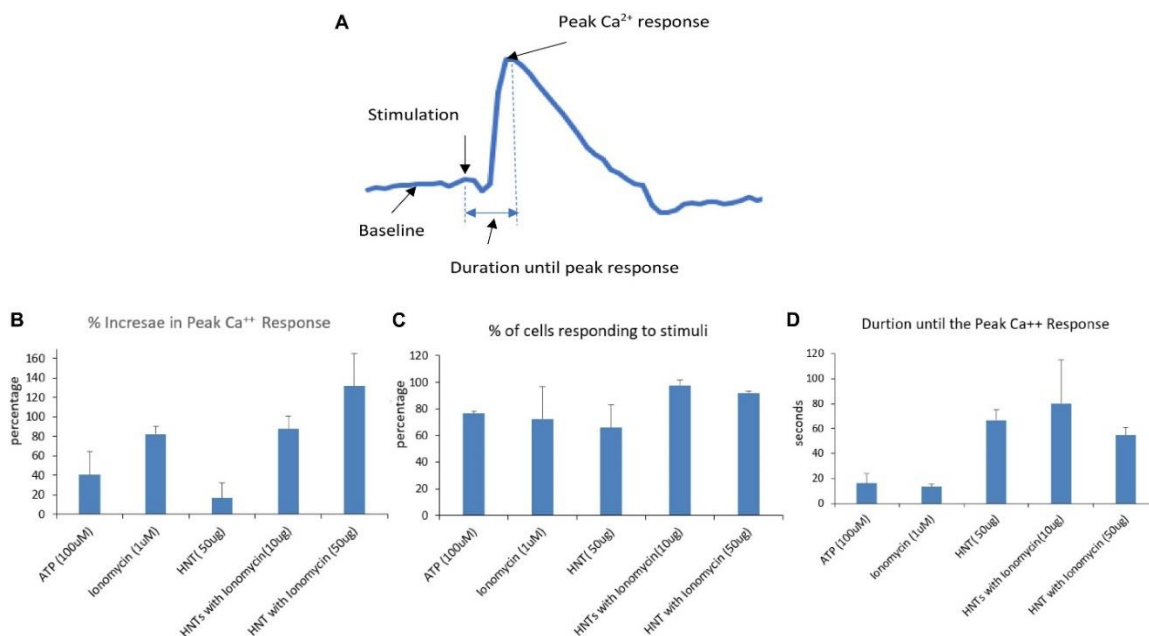


Figure 5-11: (A) Signal analysis scheme. (B–D) Parameters obtained from each calcium signal averaged over the region of interests ranging from 41 to 140 for each condition in a single experiment and then averaged for three experiments. The error bars represent the standard deviations in between the experiments [from our paper 75]

Figure 5-11D represents the time taken for the cells to produce the peak calcium response. It tells us how delayed or instant peak response was, indicating the delivery properties of halloysite clay nanotubes. The duration of release until peak calcium response after the stimulation was found to be 80 s for the nanoclay loaded with ionomycin at 10 $\mu\text{g}/\text{mL}$, 54 s for halloysite loaded with ionomycin at 50 $\mu\text{g}/\text{mL}$ and 66 s for 50 $\mu\text{g}/\text{mL}$ halloysite alone. This result along with results of Figure 5-11B, C explains that using a low concentration 10 $\mu\text{g}/\text{mL}$ HNT-ionomycin formulation is enough to get enhanced delivery of ionomycin for a prolonged time as compared to using just ionomycin itself. Using a higher concentration (50 $\mu\text{g}/\text{mL}$) can increase this response further but delay is better achieved with the use of lower concentrations.

In contrast, the duration was very short for ionomycin 1 μM at 13 s and ATP at 16s. The duration was found higher for the halloysite loaded and unloaded samples as compared to ionomycin and ATP in their soluble forms. This indicates that there is delayed diffusion from the nanotubes due to the soluble ionomycin and ATP release being much faster.

All the results discussed in Figure 5-9, 5-10, and 5-11 indicate that the halloysite loaded with ionomycin showed delayed and gradual release of ionomycin into the cells, that once it reaches the peak response it continues to diffuse for a prolonged time which is expected to be up to 24 h as was observed for the nanotubes loaded with RITC Figure 5-3, and Figure 5-4; 24 h treatment of BMVECs with ionomycin concentration of 1 μM used throughout the experiment didn't show any cytotoxicity to the cells.

5.2.13 Co-culture Studies of Blood–Brain Barrier

The confluence of the bilayer of astrocyte and endothelial cells was examined using a non-inverted microscope after Diff-Quik staining of the cells (Figure 5-12A). When a continuous monolayer was ensured, the additional cells were examined using non-inverted confocal microscopy to indicate the two cells assay (Figure 5-12B, C– both astrocyte and endothelial), based on the cell dimensions that have been seen on two distinct planes (0.3 μm step in the z-axis). The co-culture model of endothelial and astrocyte cells was, thus, produced. This represented a simulated brain barrier microenvironment where these two cell types (endothelial which are brain cells that make up the vascular structure and astrocytes, one of the main structural cells), are present in the complex layer holding the glial cells and neurons together.

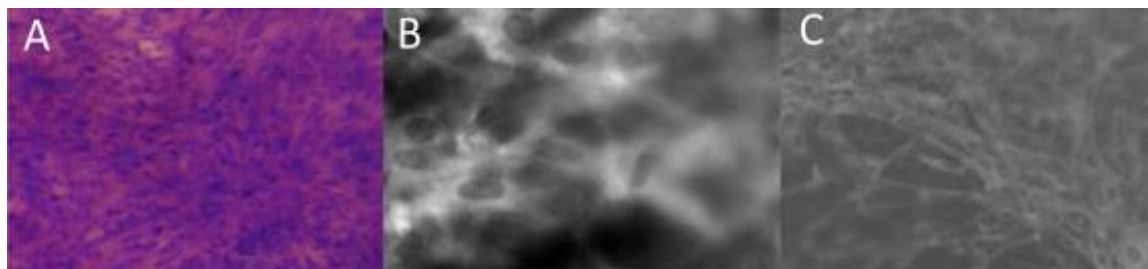


Figure 5-12: DiffQuik-stained images of a model brain barrier of aco-cultured endothelial astrocytes plated on a porous membrane. (B), (C) (z-stack images with a 0.3 μm step size) of non-inverted microscopy images of the transwell assay with a layer of b astrocytes and c endothelial cells [76]

5.2.14 Passage of RITC through the Co-culture Model

The bilayer as well as images of solution beneath the cell inserts after the treatment with ‘nano-torpedo’ clay formulations are shown in Figure 5-13, part of which displays the dispersion of RITC-loaded HNT without the cell membrane. The intensity of rhodamine that is released by HNT after passing through the transmembrane for 4 h is shown in Figure 5-13B. A negative control where the media alone is present, i.e., no HNT or rhodamine, is shown in Figure 5-13C no fluorescence signal was observed. Understanding the function of the transmembrane which allows the gradual passage of the rhodamine and partial passage of HNT in some cases, was one of the main purposes of the present study.

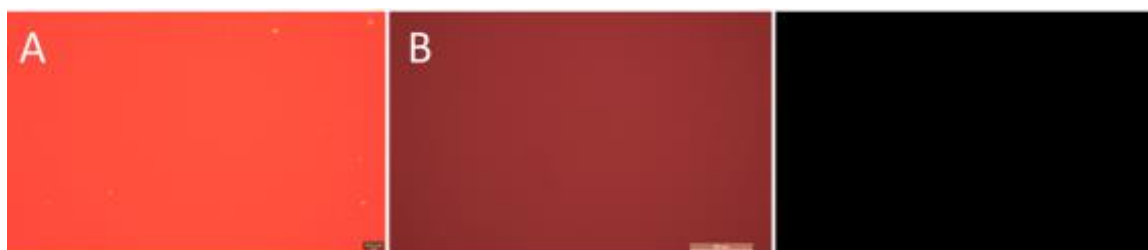


Figure 5-13: Controls (A) 20 $\mu\text{g}/\text{mL}$ HNT-RITC fluorescence intensity (no cell inserts, direct addition to the bottom well), (B) 20 $\mu\text{g}/\text{mL}$ HNT-RITC added to the support, and (C) membrane support treated with media alone [76]

The treatment conditions were as follows: 20 $\mu\text{g}/\text{mL}$ HNT-RITC formulations were placed on top of the well with the designed bi-cell membrane for an analysis of a time-dependent passage of a rhodamine nano-torpedo through the co-culture barrier model membrane over a period of 24 h. The RITC fluorescence intensity under the membrane increased significantly from the 4-h to the 24-h treatment time, indicating penetration by the HNT carrier. The fluorescence signal grew moderately in the first hour but by 24 h it had increased to 85%. Some decrease in the fluorescence intensity at the 4-h time point occurred because the co-culture cell membrane absorbed some of the upcoming rhodamine but further passing enhanced the signal growth beneath the model barrier (Figure 5-14A, B). The HNT nanotubes being utilized in drug delivery were probably as efficient as this because of the predominantly vertical penetration through the cell membrane. An MTT assay was performed 24 h after treatment of the cells plated at 10,000 per mL when they reached 60% confluency to assess cell metabolism as the measure of cytotoxicity (Figure 5-14C).



Figure 5-14: Results of HNT penetration through the membrane: (A, B) fluorescent intensity of the solution beneath the co-culture brain-barrier model after 4 and 24 h of treatment (C). The membrane cell viability after 24 h of treatment with HNT and copper nanoparticles as a negative control [76]

The results indicated that the empty HNT nanotubes did not affect the cell metabolism in BMVECs and, hence, showed no significant sign of toxicity as the cellular metabolism was observed to be within 1–2% for the treatment of 10, 25, and 50 $\mu\text{g}/\text{mL}$ of HNT compared to control cells treated with media alone. Positive control of toxicity with 6 $\mu\text{g}/\text{mL}$ of copper nanotubes (CuNPs) added demonstrated inhibition of the cell metabolism by 27% within 24 h.

5.3 Conclusions

Halloysite nanotubes (HNT) deployed as tiny ‘torpedoes’ were used to penetrate the model brain microvascular endothelial cell membrane and released their rhodamine (dye) and ionomycin (drug) payload effectively in vitro over an extended period of time. This approach showed that HNT interacted with the barrier cells, not only binding to them but also penetrating inside to the vicinity of the nuclei without causing cell stressed. The release of the loaded rhodamine isothiocyanate and ionomycin (3 and 8 wt.%) from the nanotubes was extended for >24 h.

The development of a blood–brain barrier model, which consists of a 0.4 μm porous polystyrene transwell support covered by sequential seeding of endothelial and astrocyte cells was realized. Layering of endothelial and astrocyte cells on top of each other created a model of the brain barrier which was tested for penetration by the nanotubes. The nanotubes were found to have penetrated partially the cell membrane while releasing the drug payload past this barrier. HNT nanotubes capable of passing the model barrier have potential as drug carriers to aid in the treatment against brain disease.

CHAPTER 6

DIAZEPAM AND XZYLAZINE LOADED CLAY NANOTUBES

6.1 Diazepam and Xzylazine Loaded Clay Nanotubes Permeate the Brain Through Intranasal Administration and Shows No Behavioral Changes in Mice

The blood-brain barrier (BBB) continues to be a major barrier to the permeation of therapeutics into the brain, limiting the availability of viable compounds for the treatment of neurological deficits. There is a dire need to address this challenge with new candidates that could potentially carry the vital molecules to the brain. This study showed that HNTs possess the ability to permeate the brain when administered intranasally, and the accumulation of these molecules has not resulted in significant behavioral changes in the mice. This work was performed in collaboration with Dr. T. Murray lab grad student Y. Yanamadala. In this collaboration, I made all nanoclay formulations and assisted in some of animal experiments. The paper on these results is now finalized and will be submitted for publication: Y. Yanamadala, T. Murrey, M. Saleh, Y. Lvov, *Intern. J. Molec. Sciences*, special issue: “Novel Bio-inorganic Materials,” will be submitted by March 2023, “Diazepam loaded clay nanotubes permeate the brain through intranasal administration and shows no behavioral changes in mice.”

6.2 Preview

The administration of medications to the brain is still hindered by the physiochemical features of the blood-brain barrier (BBB), which either entirely prevent the permeability of certain drugs, modify the therapeutic efficacy of the drug, or allow just sub-therapeutic doses [102], altering drugs at BBB. Although the BBB presents a hurdle for the transport of therapeutic molecules, it is of equal importance to preserve the barrier's integrity since it plays a crucial function in maintaining homeostasis and protecting the brain from toxic substances and infections [102-104]. The emergence of new technology has facilitated the creation of new medication delivery systems and the enhancement of current approaches. With the expanding number of CNS diseases, however, there is still an opportunity for creating new strategic carriers that could successfully transport therapeutic compounds to the brain. According to global figures from 2021, the prevalence of brain problems has surpassed cardiovascular diseases and cancers [103]. In addition to pathological conditions such as epilepsy, TBI, Alzheimer's, and Parkinson's, among others, increased substance abuse disorders, environmental pollutants (lead, asbestos, etc.), and COVID-related mental conditions all contribute to the rise in CNS problems that must be effectively addressed. Explosive development of nanoparticles such as HNTs as carriers has revealed exciting potential for the investigation of brain penetrating capabilities and drug delivery to the brain.

The therapeutic outcome of the medication is dependent on the route of administration. It is optimal to choose the administration of a medicine based on its physiochemical features and interactions [105]. Choice of route also depends on the amount of drug to be supplied, its solubility, pH, and the place of administration [106]. In

addition, head posture, surgical interventions, distribution mechanism, delivery methods and volume affect the deposition of the drug in the nasal passages [107]. To transfer the medicine to the brain, intranasal administration has numerous advantages that overcome most disadvantages associated with parental, oral, transmucosal, and direct injections. Intranasal (IN) administration is a noninvasive route that absorbs medicine from the nasal cavity via the trigeminal and olfactory pathways and delivers it straight to the brain parenchyma [108]. IN has numerous advantages, including self-administration (in humans) and ease of administration, noninvasiveness, BBB-passage, and quick onset effect. However, some of the medications may induce nasal discomfort, and poor availability of large-molecule drugs [109]. Recent research has demonstrated that tiny peptide medicines and nano molecules can be absorbed via nasal delivery.

In this study, we administered HNTs or HNTs loaded with drug intranasally to C57BL/6NHsd wild-type mice for six days and evaluated their behavioral changes using a variety of behavioral analysis techniques, including the rotarod, neurological severity score, novel object recognition, and open field tests. The tests of HNT-treated mice were compared with those of SHAM mice to determine whether there were any differences. All these assessments aid in identifying any stress, anxiety, memory deficits, sensory-motor cognition abnormalities, or other behavioral abnormalities that may result from the delivery of HNTs. After 4 hrs, 12 hrs, 24 hrs, 48 hrs, 3 days, and 7 days of treatment with Rhodamine-loaded HNTs, the brains of mice were removed and examined under a fluorescent microscope to assess the brain permeation capabilities. In addition, to test the drug-carrying capabilities of HNTs to the brain, diazepam-loaded HNTs or Xylazine

loaded HNTs were administered to mice for six days as a control to evaluate the behavioral changes following treatment.

6.2.1 Preparation of HNT's with RITC, Diazepam, and Xylazine

These nano-formulations were conducted using sample #19 halloysite from Applied Minerals. Pristine halloysite was first measured with the appropriate amount of Rhodamine in mgs. Ratios of 1:1 and 1:2 were prepared of halloysite to the dye. Once both initial measurements were concluded, samples were mixed in DI water through ultra-sonication for 10 minutes. Sonication allows the halloysite to disperse properly initiating the process of creating the super saturated solution that we desire for maximum dye encapsulation. It is important to note that no external surface modification i.e., polymer coating was used in these formulations. After sonication, the solution is stirred on a magnetic stir plate for 24h. at 20–22 °C. Now that the saturated solution is complete, using centrifugation we separate our product in addition to washing it to remove any excess dye that could be attached to the outer shell of the tubule. Centrifugation is completed by 3 repetitions at 4000 RPM for 3 minutes. The sample is finally dried at 70°C for 24 h. before analysis begins.

Encapsulation these two sedative drugs was also completed without any modification to the tubular structure of the nanomaterial. Initially, the diazepam loading procedure was completed, resulting in 1:2 and 1:3 ratios of halloysite to drug. which began by crushing the drug tablets with a mortar pestle into a fine powder like the look of the halloysite powder in its pure form. Producing a super saturated solution with the use of DI water through sonication for 10min and mixing at 20–22 °C for 24h. The solution was then separated and washed through centrifugation 3 times at 4000 RPM for 3

minutes. The loading procedure was replicated for xylazine except that the tubules were mixed with its injectable form to encapsulate it. The drying process to ensure the drugs were properly loaded inside the lumen of the nanotubes was completed using a desiccator vacuum for 24 hours.

6.2.2 Animal Care and Handling

Animal handling, care and the experimental procedures were conducted owing to the guidelines and in conformity with Louisiana Tech University Institutional Animal Care and Use Committee-approved protocols. Wild type C57BL/6NHsd were purchased from Jackson Laboratory and bred according to the need. Animals were maintained in a constant environment with 12 hrs dark/light cycle and cared for by providing food and water ad libitum. Randomly 3 female mice and 3 male mice between age groups 8-16 weeks and weight between 8-27 gms were chosen and assigned to each of the following groups. 1) Sham treatment with vehicle water, 2) Treatment with HNTs 3) Treatment with HNTs loaded with diazepam 4) Diazepam treatment 5) HNTs loaded with Xylazine 6) Xylazine treatment.

6.2.3 Intranasal/Intraperitoneal Administration

The mice were separated into individual cages and weighed. The mouse was sedated with 2% isoflurane in 500ml/min airflow via anesthetic chamber (Somnosuite digital vaporizer system (Kent Scientific Corporation, Torrington, Connecticut, United States)). After anesthesia, mice were delivered 6 μ l of 2 mg/ml HNTs into one nostril while in a supine position at 70 degrees, followed by three more treatments administered into alternate nostrils with a minute between each treatment. In addition, 3 mg/ml (dose determined by preliminary testing) of HNT-loaded diazepam (HNT-diazepam) or 3

mg/ml of HNT-loaded with xylazine (HNT-Xylazine) or 2 mg/ml of diazepam or 2 mg/ml of xylazine was administered for six days in a similar manner to HNT administration to mice receiving this treatment. For drug BBB permeability 2 mg/ml HNTs loaded with Rhodamine (HNT-RITC) or 1 mg/ml Rhodamine were administered. During the therapy, the mouse was sedated using a nose cone containing 1% isoflurane. After receiving treatment, the mouse was returned to its cage and observed for at least 10 minutes for seizures or abnormalities. The treatments were continued at the same time point for an additional five days.

To determine the permeability of HNTs to the brain after intraperitoneal administration, mice were given 10% w/v of 2mg/ml HNTs and sacked 4 hours later. The mouse was separated, weighed, and sedated in accordance with the above procedures. Once the mouse was completely sedated, it was positioned supine and given an intraperitoneal dose before being returned to its cage. The mouse was observed for 10 minutes after treatment for seizures or abnormalities.

6.3 Neuro-Behavioral Tests

A variety of tests were conducted to assess the sensory, motor coordination, stress, anxiety, and behavioral alterations in the mice.

6.3.1 Rotarod Test

Rotarod test begins three days (-3) prior to the administration of the HNTs. After two days of training on the rotarod (Panlab Model # 76-0770, Harvard Apparatus) (Hiromi) device, the results were recorded on the third day (-1). On -1, 2, 5, and 7 days, the time the mouse spends on the rod and its rpm were recorded. Before each test, the mice were acclimated to the environment for at least 10 minutes to lessen stress, and the

rotarod lanes were thoroughly cleaned between each mouse test. Each day, three consecutive trials for each mouse were conducted with a 10-minute rest between trials two and three. The average of the two best trials was documented. This test assesses the locomotor function, coordination, and learning capacities of mice. To minimize variability, the scores were standardized relative to the baseline (-1).

6.3.2 Modified Neurological Severity Score (mNSS)

In this study, mice were assessed on days 2, 5 and 7 on a scale from 0 to 8 for any possible neurological alterations. The following eight behaviors were evaluated: hindlimb flexion, startled response, seeking behavior, capacity of mice to walk on elevated bars 3 cm, 2 cm, and 1 cm broad and 30 cm long (1 minute from the center), and ability to balance on a 0.5cm thick circular rod and 0.5cm width square beam (at least for 30 seconds). mNSS was used to assess aberrant motor and muscular conditions, balancing ability, reflexes, visual, proprioceptive, and tactile sensory functions (schaar). Each failure task resulted in one point, so an eight-point score indicates severe neurological failure.

6.3.3 Open Field (OF)

Open field tests were conducted to determine the anxiety levels and locomotor abilities of the test mouse as it explored the 30 cm x 30 cm x 25 cm white wooden box in a controlled environment. The white box provides a contrast for video analysis and offers large open spaces, resulting in mice anxiety due to social isolation and exposure to novel environment. Prior to each test, each mouse was acclimatized to the room for at least ten minutes, and the wooden box was cleaned with alcohol to remove any scents or infections that could have been caused by the mice that had been tested earlier. After

placing the mouse in the center of the wooden box, a five-minute recording was captured using a FIJI-programmed camera stationed above the box (Figure 6-1).

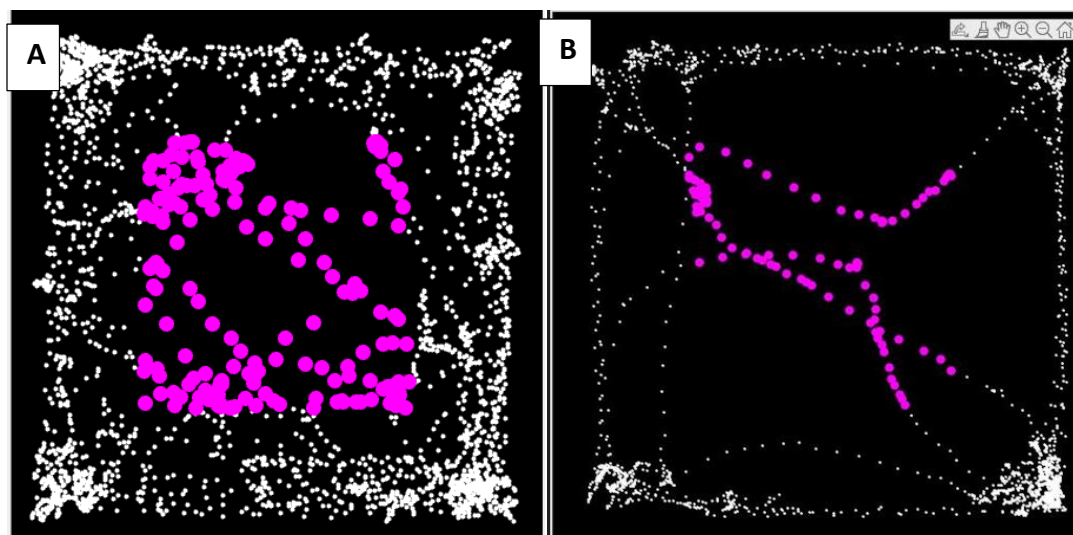


Figure 6-1: (A) The traces of a mouse that explored the entire open field. (B) Trace of a stressed mouse that did not explore the field's center and confined to the open field's edges

6.3.4 Novel Object Recognition

NOR is a low-stress test used to assess mice's memory deficiencies. This test depends on the mice's natural inclination to investigate novel objects (Lueptow). This test was often conducted following the open field test to provide the necessary acclimatization period. If the test was not completed after OF, the mice will be habituated to their new surroundings for five minutes. The mouse was placed in the center of the box, which contained two objects of identical size at each adjacent corner. The videos were captured for five minutes, then re-recorded for five more minutes during which one object was replaced with a new object of identical size but different shape. Both videos were evaluated to determine the mice's ability to memorize the novel object in relation to the amount of time spent in its vicinity. To limit external stimulation, preventive steps

were implemented (Figure 6-2A,B). Discrimination index (DI) = (time spent with novel object x 100)/ (time spent with identical object + time spent with novel object).

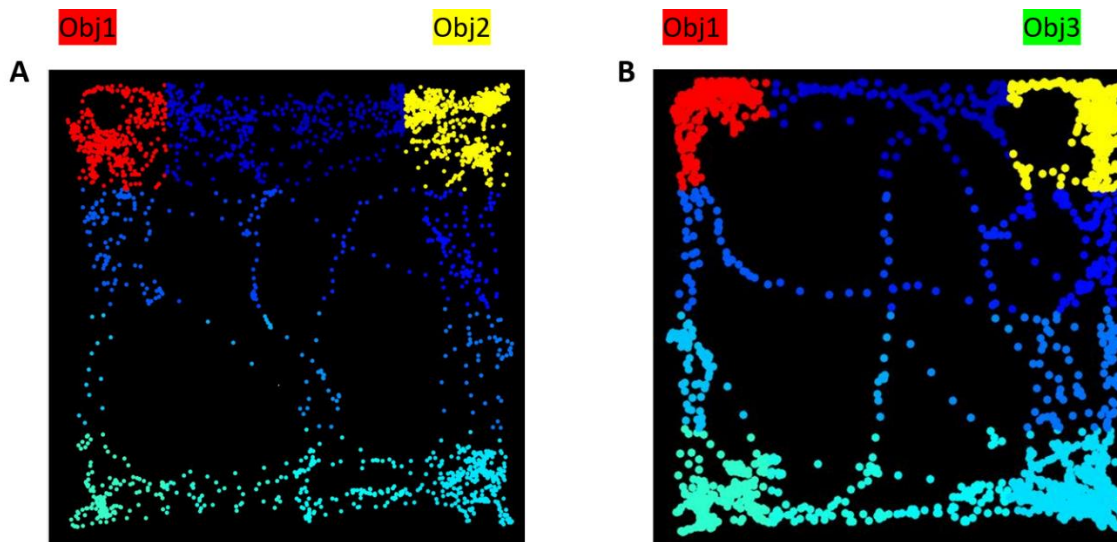


Figure 6-2: Are the trace of the mouse during the two novel object recognition tests. (A) Trace of the mouse with two similar sized objects (Obj 1 and Obj 2) in the field. (B) Trace of the mouse with one of the objects replace with similar sized object (novel object, Obj 3)

6.3.5 Behavioral Video Analysis (MATLAB)

After being modified with image J software, the behavioral videos were analyzed using MATLAB software. Videos were initially converted to AVI (Audio Video Interleave) files at 10 fps, after which they were edited to remove audio and uncompressed to grayscale. These uncompressed recordings were precisely reduced to 5 minutes, or 300 seconds, and the final frame was modified to remove the mouse so it could be used as the video's background to eliminate background noise. The necessary adjustments, such as altering the angles to fit the square, were made, and then these files were converted to multi-TIFF files, which were then read by MATLAB plugins.

6.4 Brain Removal and Imaging

6.4.1 Perfusion and Extraction of Brain

After seven days of behavioral testing, the mice were sacrificed, and their brains were removed for further examination. Mice were sacrificed at 4, 12, 24, 48 hours, 3 days, and 7 days after treatment to assess the permeability of Rhodamine-loaded HNTs. The mouse was removed from the cages, weighed, and transferred to the anesthetic chamber for sedation with 2% isoflurane and 500 ml/min air flow (Somnosuite digital vaporizer system, Kent Scientific Corporation, Torrington, Connecticut, United States). Once the mouse had been completely anesthetized and placed in a supine position, 10% w/v of ketamine (10mg/kg)/xylazine (1mg/kg in saline) was administered intraperitoneally. The mouse will be returned to its original cage, which will prevent it from fighting back anesthesia. After 15 minutes, a 10% booster dose may be delivered if the mouse is not sufficiently sedated, as determined by pinching the toes and observing the eye reflexes.

Once the mouse was completely sedated, its forelimbs and tail were taped to the surgery table while it was laid in supine position to expose its stomach. An incision was made to expose the thoracic cavity and heart, and then the aorta was punctured to facilitate blood drainage. Once the blood begins to drain, the left ventricle of the mouse was perfused with 25 ml of 1x ice-cold PBS and 25 ml of 4% ice-cold formalin. Utilizing a peristaltic perfusion pump, the liquid was pumped to the ventricle. Once the liver was cleansed, the mouse was decapitated, and the brain was removed using the appropriate surgical tools. The brain was then fixed in 4% formalin for eight hours, after which 30% sucrose was added until saturation at 4°C.

6.4.2 Vibratome Sectioning

Using the oscillating tissue slicer vibratome EMS-500 (Electron Microscopy Sciences, Hatfield, PA) Fig, the fully saturated brains are sectioned for HNT visualization and distribution. The brains were wiped with a sanitized paper towel to remove any excess sucrose solution, and the brain stem was removed to create a flat base. Later, the brain was encased in a 2% solution of low-melting agarose. Later, the encased brains were adhered to the mounting block by trimming excess agarose. Once a steady base was achieved, 60 μm sections were cut. Throughout the process of slicing, the brain is submerged in an ice-cold buffer solution. The slices were transferred with care to a 48-well plate containing PBS solution and stored in the dark until the preparation of slides.

6.4.3 Preparation of Samples for Imaging

The tissue sections were stained with DAPI for 10 minutes at 4°C on a shaker, followed by optical clearing with varying glycerol concentrations. The sections were soaked for 10 minutes in 30%, 50%, 70%, and 90% concentrations of glycerol, respectively. After saturating the sections, they were mounted on slides containing anti-fade mounting media. The sections were arranged from rostral to caudal order, including the olfactory bulb and different regions of the cortex. A cover slip was placed on to the slide with care to avoid trapping of air bubbles that would interfere with imaging. After removing excess media, the cover slip was sealed with nail polish, and the slides were stored in the dark storage box until imaging.

6.4.4 Imaging

The Olympus IX51 was used to capture phase contrast, DAPI, and RITC images of the sections while maintaining the same settings between the images and sections.

Multiple regions of the same section were imaged, and several measures were taken to prevent bleaching of the section during imaging, including reducing the light intensity, imaging time, and acquiring RITC images initially, followed by DAPI and bright light.

6.5 Halloysite Drug Loading and Delivery

6.5.1 Thermogravimetric Analysis and Release Profile of RITC

Thermogravimetric analysis is utilized in this process to determine the existence of the desired product to be encapsulated or attached to the surface of the tubules. This graph displays major phase changes at different temperatures signified by their change in weight %. The loss in weight % compared to the weight of the composite (HNT) is calculated by the TGA program to provide us with the final % of the drug that is present (Figure 6-3). The temperature on the x-axis begins at 100°C as everything before that is usually water. It is known that pristine halloysite has a major phase transition at 500-550 °C. Due to that the graph does not display any information past 600 °C because it will not result in any desired information. It is concurred that there were respective burning points at 200-400 °C for the RITC, diazepam, and xylazine. That these drugs were indeed present in the halloysite tubules. Estimated RITC loading was calculated at 10 ± 2 wt% and 8 ± 1 wt% for diazepam. However, xylazine had a 15 ± 2 wt% which could be due to some external drug attachment to the surface of the nanotube.

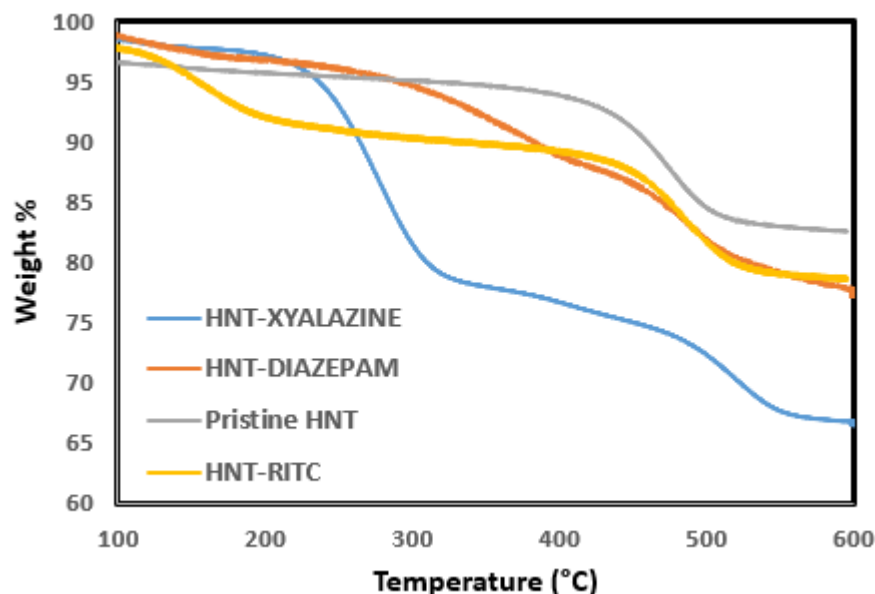


Figure 6-3: Thermogravimetric analysis of major phase transitions of drugs that were encapsulated in pristine halloysite nanotubes. The phase transition of halloysite by itself is 500-550 °C whilst the respective (RITC, diazepam, and xylazine) drugs underwent burning between 200 and 400 °C. By calculating the respective weight loss in each sample, the loading percentage for RITC was 10 ± 2 wt% and diazepam at 8 ± 1 wt%. Xylazines weight change was calculated at 15 ± 2 wt%

To determine the optimal concentration for both intranasal and intraperitoneal administration, HNTs-Rhodamine in water was administered to mice at various concentrations beginning at 0.5 mg/ml. Even at low concentrations of 1mg/ml, fluorescence has been observed throughout the brain, as per the preliminary data (not included). However, 3 mg/ml has demonstrated superior brain absorption and fluorescence. Consequently, this concentration was utilized in the study. The mice received the dosages specified in the methods section. Later, brains were extracted at various time points to visualize the rhodamine's uptake and distribution. The collected brains were sectioned into 60 μ m thick slices, stained with DAPI, and imaged with phase contrast, fluorescence filters using fluorescence microscopy.

6.5.2 Intranasal and Intraperitoneal Delivery of HNT + RITC to the Olfactory Bulb and Cortex

To determine the optimal concentration for both intranasal and intraperitoneal administration, HNTs-Rhodamine in water was administered to mice at various concentrations beginning at 0.5 mg/ml. Even at low concentrations of 1mg/ml, fluorescence has been observed throughout the brain, as per the preliminary data (not included). However, 3 mg/ml has demonstrated superior brain absorption and fluorescence. Consequently, this concentration was utilized in the study. The mice received the dosages specified in the methods section. Later, brains were extracted at various time points to visualize the rhodamine's uptake and distribution. The collected brains were sectioned into 60 μm thick slices, stained with DAPI, and imaged with phase contrast, fluorescence filters using fluorescence microscopy.

Punctate staining throughout the brain is visible in images taken after 4 hours of intranasal administration. Mice given HNTs only showed no fluorescence when examined with the TRITC filter at any time point. However, RITC only treated animals exhibited relatively insignificant fluorescence compared to controls. Fluorescence in the olfactory bulb was comparatively higher than the cortex in mice given treatment for 4 and 12 hours, respectively. Intriguingly, the fluorescence was more consistent across the brain at 24 and 48 hours (72 hours not included since the fluorescence was not visible at the same intensity as other time points, but after slightly revising the settings, it was visible). But after seven days, there was no trace of fluorescence anywhere in the brain (Figure 6-4, Figure 6-5, and Figure 6-6).

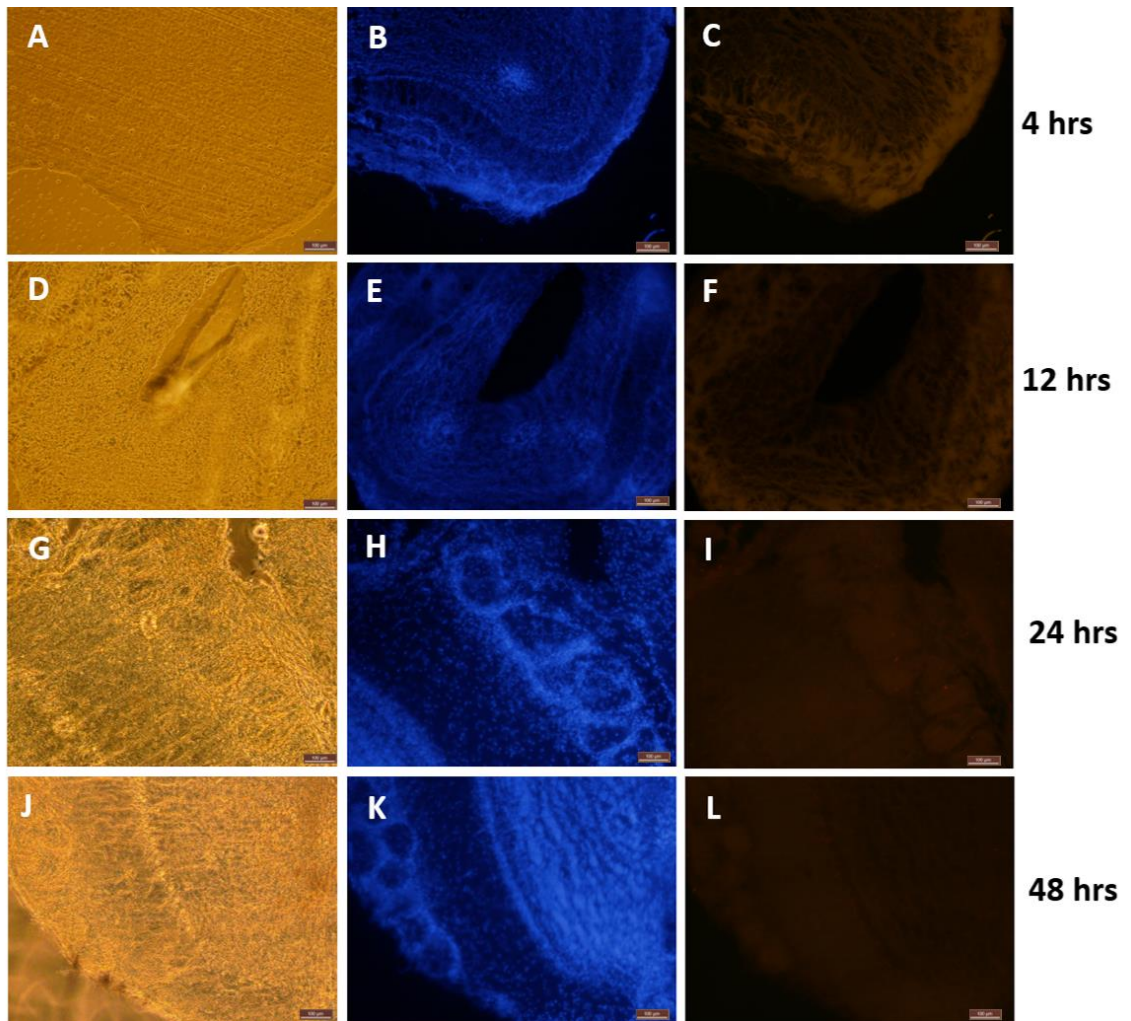


Figure 6-4: Fluorescence images of the brain slices of the olfactory bulb at time points 4, 12, 24 and 48 hours after intranasal administration of HNT-Rhodamine. Images (A), (D), (G), (J) (first column) are phase contrast images. (B), (E), (H), (K) (second column) are images acquired through DAPI filter and (C), (F), (I), (L) (third column) are acquired through TRITC filter. Images from (A) through (F) were acquired using 10x objective and (G) through (L) were imaged through 40x objective

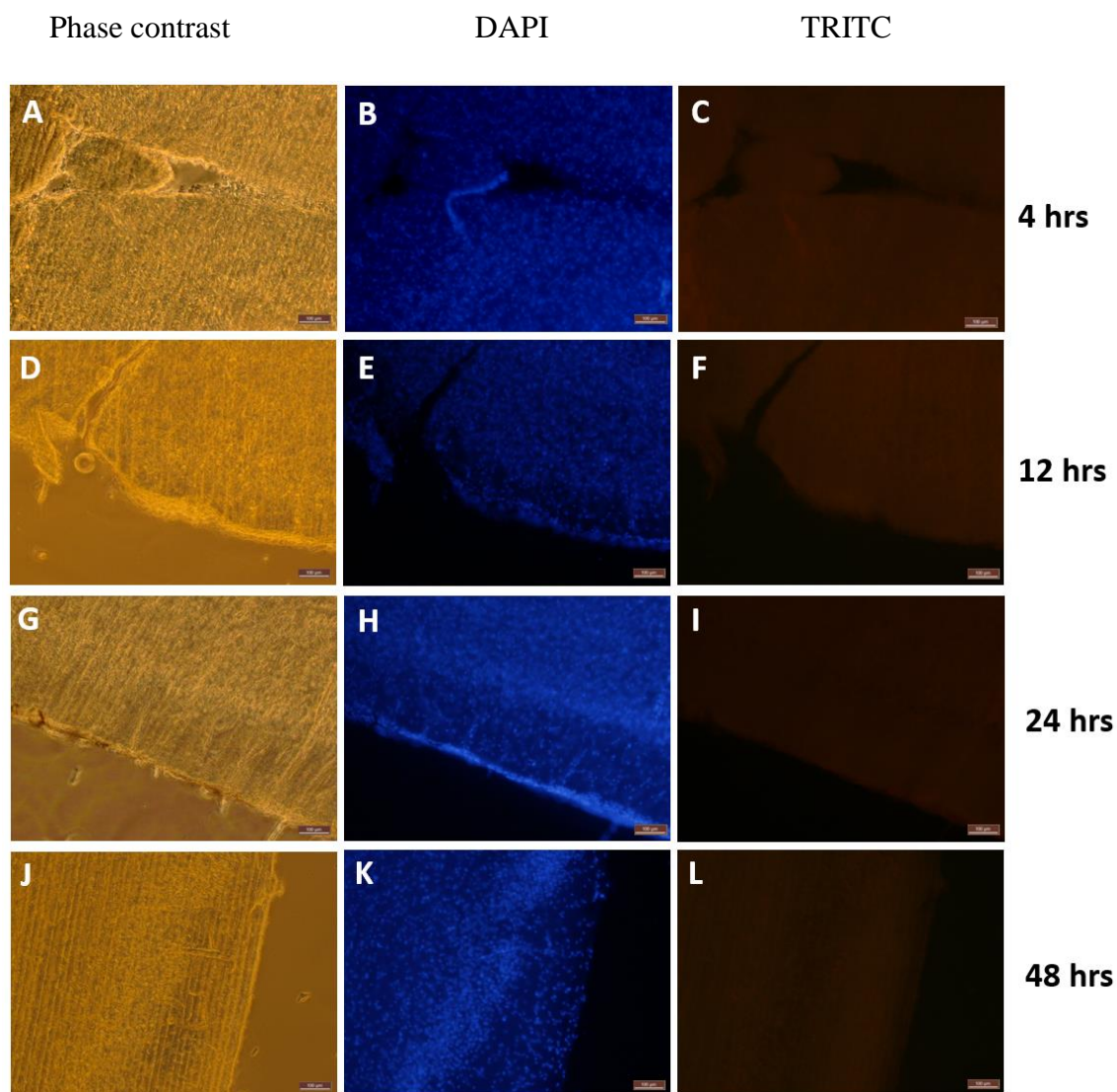


Figure 6-5: Fluorescence images of the brain slices of the cortex region at time points 4, 12, 24 and 48 hours after intranasal administration of HNT-Rhodamine. Images (A), (D), (G), (J) (first column) are phase contrast images. (B), (E), (H), (K) (second column) are images acquired through DAPI filter and (C), (F), (I), (L) (third column) are acquired through TRITC filter. Images from (A) through (F) were acquired using 10x objective and (G) through (L) were imaged through 40x objective. The scale bar is 100 μm for images (G-L) and 31.5 μm for (A-F)

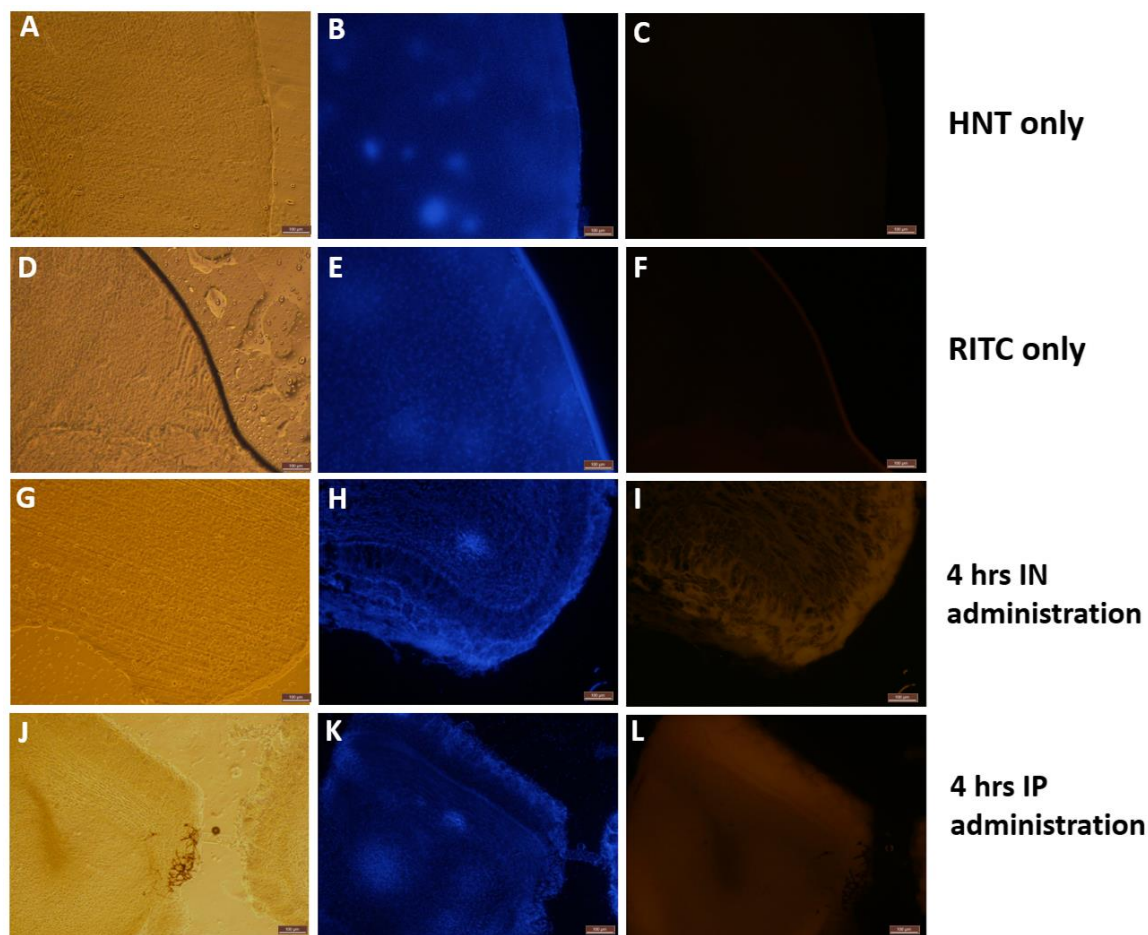


Figure 6-6: Florescence images of the mice brains that were acquired 4 hours after treatment. The first column (A), (D), (G), (J) (first column) are phase contrast images while the second column (B), (E), (H), (K) are images acquired through DAPI filter and third column (C), (F), (I), (L) were acquired using TRITC filter. The first-row images are from the brain after intranasal treatment with HNTs only while second row with intranasal RITC treatment only, third row with intranasal HNT-Rhodamine administration and fourth row was HNT-Rhodamine treatment intraperitoneally. The images were acquired using 40x for (A-I) and 10x for (J-L). The scale bar for (J-L) is $31.5\mu\text{m}$ and (A-I) is $100\mu\text{m}$

6.6 Behavioral Studies

6.6.1 Rotarod Score

Learning and motor cognition abilities were tested during the rotarod test. The greater the neurological damage the latency to fall will be shorter indicating reduced learning and motor cognition in the animal. To reduce variability, the scores from days 2,

5, and 7 were normalized with those from the previous day of treatment. Statistical analysis was conducted using SPSS software. Following data analysis with the T-test and Bonferroni correction, the normalized time of latency to fall was depicted (Figure 6-7).

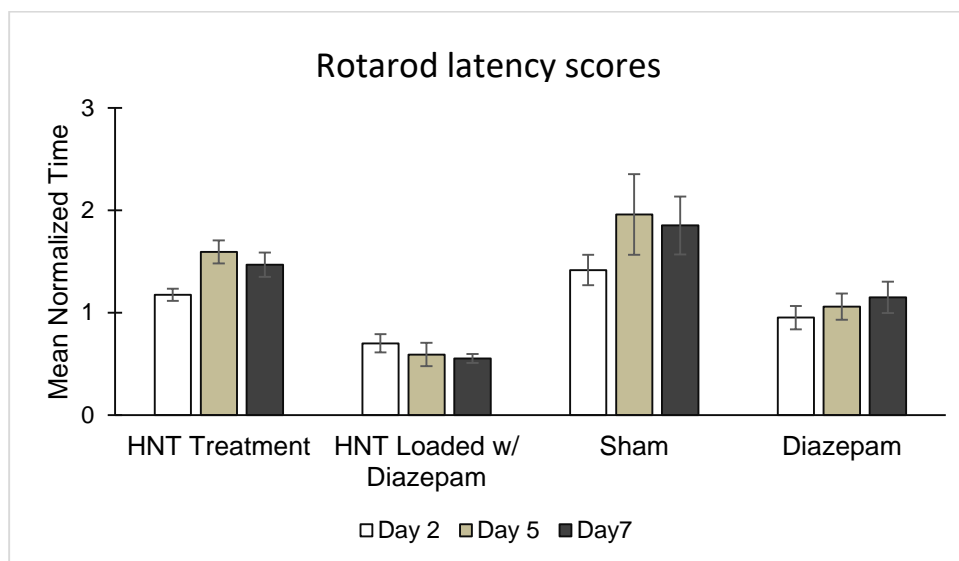


Figure 6-7: Normalized data showing time of latency to the fall on day 2, 5 and 7. The mice were treated with vehicle (sham), HNTs only, and HNT-diazepam for 6 days. Mice were divided into three treatment groups: sham (n=6), HNT (n=6), diazepam (n=6) and HNT-diazepam (n=6). Using pairwise comparison and Bonferroni correction, a T-test statistical analysis was performed. The data revealed a statistically significant difference between control and HNT-diazepam by day 7 ($p < 0.5$)

There is a strong trend, beginning on day 2, that mice receiving HNT handle the rotarod as well as the control mice. On days five and seven, the HNTs-Diazepam-treated animals displayed low trends in comparison to both HNT-only mice and control mice. It's clear from these data that Diazepam treated, and HNT-Diazepam mice are generally underperforming compared to both Sham mice and HNT-only treated mice. However, HNT- Diazepam treated mice has shown further reduced latency scores compared to that of diazepam only treated mice group. From the second day on, the HNT mice perform

similarly to the control mice. This may indicate that diazepam loaded HNTs delivered the drug to the brain.

In contrast to other groups, mice treated with HNT-xylazine and xylazine only treated mice were not trained on rotarod on days -3, -2, and -1 prior to treatment. The HNT-xylazine-treated mice group that had been trained prior to treatment appeared depressed, but once placed on rotarod, they performed normally. Therefore, we examined whether animals treated with HNT-xylazine learned similarly to mice given xylazine alone or mice in the control group. We have observed that HNT-xylazine treated mice group had trouble learning the new skill compared to the xylazine only treated group.

6.6.2 Modified Neurological Severity Score Results

The neurological severity assessment tests were conducted along with the rotarod test on the same days. The purpose of this test was to identify any neurological deficits in mice following treatment. The data revealed that mice treated with HNTs did not vary from control mice, however animals treated with HNT-diazepam had higher scores than the other three groups. Most of the mice that failed the test were unable to balance on thin rods due to diazepam-induced drowsiness.

On day two, all three treatment groups are leaning toward similarity, whereas the HNT-diazepam-treated mice group has a higher neurological severity score (NSS). As hypothesized, the HNT-diazepam-treated mice became increasingly distinct from the other three treatment groups. However, we anticipated that as HNTs-diazepam accumulated in the brain, the NSS scores would grow more. This decrease in NSS score may be due to the mice becoming accustomed to (learning) the tests and performing better on subsequent test days (Figure 6-8).

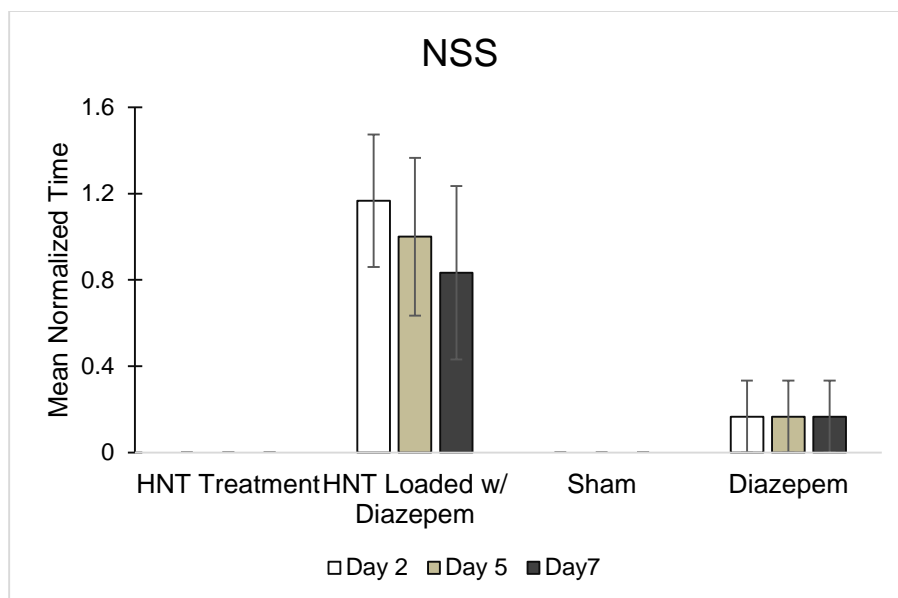


Figure 6-8: Modified neurological severity scores on day 2, 5 and 7. The mice were treated with vehicle (sham), HNTs only, diazepam, and HNT-diazepam for 6 days. Mice were divided into four treatment groups: sham (n=6), HNT (n=6), diazepam (n=6) and HNT-diazepam (n=6). Using pairwise comparison and Bonferroni correction, a T-test statistical analysis was performed. The data revealed a statistically significant difference between SHAM, HNT, and HNT-diazepam, but no difference between placebo and HNT ($p = 1.0$)

Under the influence of xylazine, mice treated with HNT-xylazine demonstrated greater neurological severity on days 2 to 5 compared to mice treated with xylazine alone. On day 7, however, there is little difference between the two groups.

6.7 Discussion

Halloysites (HNTs) are emerging as potential carrier molecules due to their wide availability, sustained drug release capabilities and ability to transport a variety of molecules [110]. These nanotubes were modified and demonstrated their effectiveness in targeted therapy [111-112] Additionally, HNTs are evaluated as topical applications, which also exhibited remarkable benefits [113]. Despite efforts to test their abilities across a broad spectrum of drug delivery, they were not evaluated for their ability to

bypass the BBB. There is a paucity of research on HNTs in terms of toxicity and behavioral changes associated with halloysites administration to the brain and BBB permeability. We examined the ability of HNTs to penetrate the brain and their distribution in the brain. When administered intranasally (noninvasive route) and intraperitoneally, our findings revealed that HNTs not only permeate the BBB, but also transport the drugs across the barrier and distribute them throughout the brain.

Our findings demonstrated that administration of nanotubules did not result in any behavioral, psychological, or neurological deficits. In addition, they have successfully transported the TRITC dye, xylazine and diazepam molecules, as confirmed by biodistribution and behavioral analysis data. After 48 hours, there was little fluorescence in the samples, and by the seventh day, there was no fluorescence observed. The absence of fluorescence may be due to the removal of HNTs and RITC from the brain, or the RITC released by HNTs may have been washed away. Intranasal administration has demonstrated a higher fluorescence intensity compared to intraperitoneal administration. Furthermore, intranasal administration of HNTs has shown punctate staining in the forebrain because of HNTs taken up by the cells. While intraperitoneal administration or RITC alone has not shown punctate staining.

Diazepam is an anxiolytic drug, and upon administration of higher dosages, would cause sedation and affect locomotor abilities [114]. We anticipated that administration of HNTs-diazepam and HNT-xylazine would elicit long-term sedation and reduced locomotor abilities in mice with a slow release of the drugs, compared to the controls. Due to the potential effects of diazepam, both diazepam and HNT-diazepam lowered test performance in mice till day 5. However, HNT-diazepam has not completely

induced locomotor deficits or anxiolytic effects in the mice as expected. This may be because, as demonstrated by Padua-Reis et al, greater dosages of diazepam have an anxiogenic effect, causing mice to explore the open arms less [114]. Alternatively, it could have been because the diazepam was not available in enough high doses to produce the physiological effect, as the release profile of HNT shows that 80% of the drug is released in the first 24 hours in the cells [75]. Furthermore, as the released drug is metabolized and the peak effects of diazepam are seen in the first hour [115], the overall amount of drug may not have been adequate to elicit locomotor deficits.

Similarly, HNT-xylazine-treated mice have also been shown to be drowsy but not enough to impair locomotion. Due to its short half-life, xylazine is rapidly metabolized and removed from the body [116]. The xylazine had no discernible influence on the mice's performance on the rotarod, despite their drowsiness due to their training on the rotarod. However, when the untrained mice administered with HNT-xylazine were placed on the rotarod to train or stabilize on the rod, all the mice had trouble learning the new skill. This was attributed to the cumulative effect of slow releasing xylazine from the HNTs, while xylazine alone had no influence on the mice's ability to acquire new skills.

6.8 Conclusion

In conclusion, HNT's successfully passed through the blood-brain barrier intranasally without causing any behavioral changes. The use of sedative and anxiolytic drugs such as xylazine and diazepam were utilized to visualize if halloysite could carry these drugs which are commonly used in in vivo mice studies to the brain effectively. Behavioral tests such as open field, rotarod, novel object recognition, and neurological severity scores were performed. The results are promising but not entirely conclusive

when tests were done with the drugs. Further tests need to be conducted optimizing the dose of drug given to the mice to induce effects for longer periods of time. Additionally, further studies need to be conducted to study the fate of HNTs once they enter the brain and the effects of long-term administration of HNTs. The positive results of this preliminary test could be utilized to expand the study and conduct additional research. If these molecules are not eliminated, HNTs could be used as a single-dose emergency treatment when the patient is uncooperative because they can be administered non-invasively, particularly for conditions such as traumatic brain injury where prompt treatment can prevent secondary injury.

CHAPTER 7

CONCLUSIONS

We sorted out halloysite clay nanotubes into two types: small halloysite with diameter of 50 nm and length of 0.7 μm which was used by researcher earlier and invented a new larger halloysite tube with diameter 85 nm and length of 1.5 μm . We recommended selective small/large clay nanotubes for usage as a drug carrier to penetrate, correspondingly, weaker cell membranes and stronger barriers like animal and human skin. In both cases this nanocarriers work as nano-torpedo, with penetration efficiently determined by their smaller cross-section of tens nanometers. This invented larger clay nanotubes allowed for the first time a dark-field microscopy visualization of halloysite in aqueous colloids demonstrating its perfect water dispersibility and Brownian motion kinetics (movie).

Experiments utilizing the new “larger” halloysite for potential skin applications by encapsulating vitamin B-12 in the larger clay nanotubes at 7 % wt which is known to have beneficial effects for overall skin health. The development of a formulation involving generic skin cream mixed with a total 5 % wt. of the nanotubes. The cream mixture is then massaged onto the samples of pig skin to determine halloysite penetration at 1mm with the larger tubes. The results were promising displaying no halloysites on the surface of the skin after the massage was complete; all loaded lay nanotubes penetrated the skin. These methods and results were not further developed due to the lack of

equipment/resources in addition to a proprietary claim by collaborating with Northstar Mine LLC.

Development of the studies of halloysite's ability to pass through the model blood-brain barrier were conducted utilizing the "smaller" traditional halloysite of 50 nm diameter. These experiments were performed in collaboration with N. Prajapati, Dr. M. DeCoster lab. First, loading RITC dye (ca. 5 % wt) into the nanotubes was made to track their movement when introduced with brain microvascular endothelial cells. Once initial penetration and binding was successful the development of a nano formulation was developed involving an antibiotic named ionomycin which has been previously used to combat cancer cells. After the drug was successfully encapsulated in halloysite (ca. 6 % wt), real-time calcium imaging was conducted to measure the fluorescence response of endothelial cells treated with ionomycin drug formulation. Furthermore, a two-cell membrane was designed utilizing transwell assays to approach a more realistic model brain barrier and halloysites ability as a "nano-torpedo". The nanotube loaded with rhodamine dye and ionomycin drug successfully passed these membranes concluding that they have penetrated through the major blood brain barrier cells without causing any toxic effects and inducing a proper fluorescence response from the cells.

For the first time, in collaboration with Y. Yanamadala, Dr. T. Murray lab, we performed in vivo (nasal and peritoneal) drug delivery to the brains of mice with new halloysite nanotube formulations. We administered HNTs or HNTs loaded with drug intranasally to mice for six days and evaluated their behavioral changes using a variety of behavioral analysis techniques, including the rotarod, neurological severity score, novel object recognition, and open field tests. There were 3 drugs utilized in this study for

behavioral analysis and as a tracker for the halloysite. Xylazine and Diazepam are both drugs that have been found to alter behavior by reducing anxiety or sedating the mice. RITC was encapsulated within the halloysite to display the movement and coverage of the nanotubes over areas such as the olfactory bulb and cortex of the brain. Overall, the HNT's successfully delivered the payload of multiple drugs to the brains of the mice, passing the blood-brain barrier without causing any negative behavioral changes when alone. These nanocarriers are not biodegradable which means they could be used as a single-dose emergency treatment.

REFERENCES

- [1] Lvov YM, DeVilliers MM, Fakhrullin RF. The application of halloysite tubule nanoclay in drug delivery. *Expert Opin Drug Deliv.* 2016 Jul; 13(7):977–986.
- [2] Y. Lvov, W. Wang, L. Zhang, R. Fakhrullin, *Adv. Mater.*, v.28, 1227–1250, 2016, “Halloysite Clay Nanotubes for Loading and Sustained Release of Functional Compounds.”
- [3] A.Glotov, A. Vutolkina, Y. Lvov, *Chem Soc. Rev*, v.50, 9240–9277, 2021, “Clay nanotube-metal core/shell catalysts”.
- [4] Santos, A., Pereira, I., Veiga, F., Reis, S., Saleh, M., and Lvov, Y. (2019). Biomedical potential of clay nanotube formulations and their toxicity assessment. *Expert Opin. Drug Deliv.* 16, 1169–1182.
- [5] Takechi R., Fakhoury M., Al-Salami H. Drug Permeation across the Blood-Brain Barrier: Applications of Nanotechnology. *Br. J. Med. Med. Res.* 2015;6:547–556. [Google Scholar].
- [6] Barnabas: W. Drug targeting strategies into the brain for treating neurological diseases. *J. Neurosci. Methods.* 2018;311:133–146. doi: 10.1016/j.jneumeth.2018.10.015.
- [7] Alexander J.J. Blood-brain barrier (bbb) and the complement landscape. *Mol. Immunol.* 2018;102:26–31. doi: 10.1016/j.molimm.2018.06.267.
- [8] Çetin M., Aytekin E., Yavuz B., Bozdağ-Pehlivan S. Chapter 7—Nanoscience in targeted brain drug delivery. In: Gürsoy-Özdemir Y., Bozdağ-Pehlivan S., Sekerdag E., editors. *Nanotechnology Methods for Neurological Diseases and Brain Tumors.* Academic Press; Cambridge, MA, USA: 2017. pp. 117–147.
- [9] Teleanu DM, Chircov C, Grumezescu AM, Volceanov A, Teleanu RI. Blood-Brain Delivery Methods Using Nanotechnology. *Pharmaceutics.* 2018 Dec 11;10(4):269. doi: 10.3390/pharmaceutics10040269. PMID: 30544966; PMCID: PMC6321434.
- [10] Abbott NJ, Rönnbäck L, Hansson E (January 2006). "Astrocyte-endothelial interactions at the blood-brain barrier". *Nature Reviews. Neuroscience.* 7(1): 41–53. doi:10.1038/nrn1824.

- [11] Hamilton RD, Foss AJ, Leach L (December 2007). "Establishment of a human in vitro model of the outer blood-retinal barrier". *Journal of Anatomy*. **211** (6): 707–16. [doi:10.1111/j.1469-580.2007.00812.x](https://doi.org/10.1111/j.1469-580.2007.00812.x).
- [12] Santos AC, Ferreira C, Veiga F, et al. Halloysite clay nanotubes for life sciences applications: from drug encapsulation to bioscaffold. *Adv Colloid Interface Sci*. 2018;257:58–70.
- [13] Tully J, Yendluri R, Lvov Y. Halloysite clay nanotubes for enzyme immobilization. *Biomacromolecules*. 2016 Feb 8;17(2):615–621.
- [14] Price RR, Gaber BP, Lvov Y. In-vitro release characteristics of tetracycline HCl, khellin and nicotinamide adenine dinucleotide from halloysite; a cylindrical mineral. *J Microencapsul*. 2001 Nov-Dec;18 (6):713–722.
- [15] Veerabadran P, Sasnur P, Subramanian S, et al. Pancreatic tuberculosis-abdominal tuberculosis presenting as pancreatic abscesses and colonic perforation. *World J Gastroenterol*. 2007 Jan 21;13(3):478–479.
- [16] Wei WB, Minullina R, Abdullayev E, et al. Enhanced efficiency of antiseptics with sustained release from clay nanotubes. *Rsc Adv*. 2014;4(1):488–494.
- [17] Veerabadran P, Sasnur P, Subramanian S, et al. Pancreatic tuberculosis-abdominal tuberculosis presenting as pancreatic abscesses and colonic perforation. *World J Gastroenterol*. 2007 Jan 21;13(3):478–479.
- [18] Vergaro V, Lvov YM, Leporatti S. Halloysite clay nanotubes for resveratrol delivery to cancer cells. *Macromol Biosci*. 2012 Sep;12 (9):1265–1271.
- [19] Rawtani D, Pandey G, Tharmavaram M, et al. Development of a novel 'nanocarrier' system based on halloysite nanotubes to overcome the complexation of ciprofloxacin with iron: an in vitro approach. *Appl Clay Sci*. 2017 Dec 15;150:293–302.
- [20] Panchal A, Fakhrullina G, Fakhrullin R, et al. Self-assembly of clay nanotubes on hair surface for medical and cosmetic formulations. *Nanoscale*. 2018 Oct 4;10(38):18205–18216.
- [21] Cavallaro G, Lazzara G, Milioto S, et al. Nanohydrogel formation within the Halloysite Lumen for triggered and sustained release. *ACS Appl Mater Interfaces*. 2018 Mar 7;10(9):8265–8273.
- [22] Lazzara G, Cavallaro G, Panchal A, et al. An assembly of organic-inorganic composites using halloysite clay nanotubes. *Curr Opin Colloid Interface Sci*. 2018 May 01;35:42–50.
- [23] Kruif JK, Ledergerber G, Garofalo C, et al. On prilled nanotubes-inmicrogel oral systems for protein delivery. *Eur J Pharm Biopharm*. 2016;101:90–102.

- [24] Carazo E, Sandri G, Cerezo P, et al. Halloysite nanotubes as tools to improve the actual challenge of fixed doses combinations in tuberculosis treatment. *J Biomed Mater Res A*. 2019 Jul;107(7):1513–1521.
- [25] Yendluri R, Lvov Y, de Villiers MM, et al. Paclitaxel encapsulated in halloysite clay nanotubes for intestinal and intracellular delivery. *J Pharm Sci*. 2017 Oct;106(10):3131–3139.
- [26] Lisuzzo L, Cavallaro G, Pasbakhsh P, et al. Why does vacuum drive to the loading of halloysite nanotubes? The key role of water confinement. *J Colloid Interface Sci*. 2019 July 01;547:361–369.
- [27] Garcia-Garcia D, Ferri JM, Ripoll L, et al. Characterization of selectively etched halloysite nanotubes by acid treatment. *Appl Surf Sci*. 2017 Nov;15(422):616–625.
- [28] Abdullayev, E., Joshi, A., Wei, W., Zhao, Y., & Lvov, Y.M. (2012). Enlargement of halloysite clay nanotube lumen by selective etching of aluminum oxide. *ACS nano*, 6 8, 7216-26.
- [29] Yah WO, Xu H, Soejima H, et al. Biomimetic dopamine derivative for selective polymer modification of halloysite nanotube lumen. *J Am Chem Soc*. 2012 July 25;134(29):12134–1213.
- [30] Shi YF, Tian Z, Zhang Y, et al. Functionalized halloysite nanotube-based carrier for intracellular delivery of antisense oligonucleotides. *Nanoscale Res Lett*. 2011 Nov 28;6(1):608.
- [31] Lun HL, Ouyang J, Yang HM. Natural halloysite nanotubes modified as an aspirin carrier. *Rsc Adv*. 2014;4(83):44197–44202.
- [32] Rapacz-Kmita A, Foster K, Mikołajczyk M, et al. Functionalized halloysite nanotubes as a novel efficient carrier for gentamicin. *Mater Lett*. 2019 May 15;243:13–16.
- [33] Ghaderi-Ghahfarrokhi M, Haddadi-Asl V, Zargarian SS. Fabrication and characterization of polymer-ceramic nanocomposites containing drug loaded modified halloysite nanotubes. *J Biomed Mater Res A*. 2018 May;106(5):1276–1287.
- [34] Kurczewska J, Cegłowski M, Messyasz B, et al. Dendrimer-functionalized halloysite nanotubes for effective drug delivery. *Appl Clay Sci*. 2018 Mar 01;153:134–143.
- [35] Li H, Zhu X, Zhou H, et al. Functionalization of halloysite nanotubes by enlargement and hydrophobicity for sustained release of analgesic. *Colloids Surf A Physicochem Eng Asp*. 2015 Dec 20;487:154–161.

- [36] Rouster P, Dondelinger M, Galleni M, et al. Layer-by-layer assembly of enzyme-loaded halloysite nanotubes for the fabrication of highly active coatings. *Colloids Surf B Biointerfaces*. 2019 Mar; 21(178):508–514.
- [37] Veerabadran NG, Mongayt D, Torchilin V, et al. Organized shells on clay nanotubes for controlled release of macromolecules. *Macromol Rapid Commun*. 2009 Jan 16;30(2):99–103.
- [38] Jang SH, Jang SR, Lee GM, et al. Halloysite nanocapsules containing thyme essential oil: preparation, characterization, and application in packaging materials. *J Food Sci*. 2017 Sep; 82(9):2113–2120.
- [39] Dzamukova MR, Naumenko EA, Lvov YM, et al. Enzyme-activated intracellular drug delivery with tubule clay nanof ormulation. *Sci Rep*. 2015 May;15(5):10560.
- [40] Hu Y, Chen J, Li X, et al. Multifunctional halloysite nanotubes for targeted delivery and controlled release of doxorubicin in-vitro and in-vivo studies. *Nanotechnology*. 2017 Sep 15;28(37):375101.
- [41] Zhang J, Luo X, Wu YP, et al. Rod in tube: a novel nanoplatform for highly effective chemo-photothermal combination therapy toward breast Cancer. *ACS Appl Mater Interfaces*. 2019 Jan 30;11 (4):3690–3703.
- [42] Yamina AM, Fizir M, Itatahine A, et al. Preparation of multifunctional PEG-graft-Halloysite nanotubes for controlled drug release, tumor cell targeting, and bio-imaging. *Colloids Surf B Biointerfaces*. 2018 Oct;1(170):322–329.
- [43] Massaro M, Amorati R, Cavallaro G, et al. Direct chemical grafted curcumin on halloysite nanotubes as dual-responsive prodrug for pharmacological applications. *Colloids Surf B Biointerfaces*. 2016 Apr 01;140:505–513.
- [44] Naumenko EA, Guryanov ID, Yendluri R, et al. Clay nanotube– biopolymer composite scaffolds for tissue engineering. *Nanoscale*. 2016;8(13):7257–7271.
- [45] Xue J, Niu Y, Gong M, et al. Electrospun microfiber membranes embedded with drug-loaded clay nanotubes for sustained antimicrobial protection. *ACS Nano*. 2015;9(2):1600–1612.
- [46] Patel S, Jammalamadaka U, Sun L, et al. Sustained release of antibacterial agents from doped halloysite nanotubes. *Bioengineering*. 2015 Dec 23;3(1):1–14.
- [47] Jia L, Zhou T, Xu J, et al. Visible light-induced lanthanide polymer nanocomposites based on clays for bioimaging applications. *J Mater Sci*. 2016;51(3):1324–1332.
- [48] Zhou T, Jia L, Luo Y-F, et al. Multifunctional nanocomposite based on halloysite nanotubes for efficient luminescent bioimaging and magnetic resonance imaging. *Int J Nanomed*. 2016;11:4765–4776.

- [49] Micó-Vicent B, Martínez-Verdú FM, Novikov A, et al. Stabilized dye– pigment formulations with platy and tubular nanoclays. *Adv Funct Mater.* 2018;28(27):1703553.
- [50] Stavitskaya AV, Novikov AA, Kotelev MS, et al. Fluorescence and cytotoxicity of cadmium sulfide quantum dots stabilized on clay nanotubes. *Nanomaterials.* 2018;8(6):391–402.
- [51] Li LY, Zhou YM, Gao RY, et al. Naturally occurring nanotube with surface modification as biocompatible, target-specific nanocarrier for cancer phototherapy. *Biomaterials.* 2019;190-191:86–96.
- [52] Li K, Zhang Y, Chen M, et al. Enhanced antitumor efficacy of doxorubicin-encapsulated halloysite nanotubes. *Int J Nanomedicine.* 2018;13:19–30.
- [53] Dramou P, Fizir M, Taleb A, et al. Folic acid-conjugated chitosan oligosaccharide-magnetic halloysite nanotubes as a delivery system for camptothecin. *Carbohydr Polym.* 2018;197:117–1.
- [54] Ganguly S, Das TK, Mondal S, et al. Synthesis of polydopamine-coated halloysite nanotube-based hydrogel for controlled release of a calcium channel blocker. *Rsc Adv.* 2016;6(107):105350–105362.
- [55] Yendluri R, Otto DP, De Villiers MM, et al. Application of halloysite clay nanotubes as a pharmaceutical excipient. *Int J Pharm.* 2017 Apr 15;521(1–2):267–273.
- [56] Kim M, Jee SC, Sung J-S, et al. Anti-proliferative applications of laccase immobilized on super-magnetic chitosan-functionalized halloysite nanotubes. *Int J Biol Macromol.* 2018;118:228–237.
- [57] Khodzhaeva V, Makeeva A, Ulyanova V, et al. Binase immobilized on halloysite nanotubes exerts enhanced cytotoxicity toward human colon adenocarcinoma cells. *Front Pharmacol.* 2017;8:631–641.
- [58] Massaro M, Cavallaro G, Colletti CG, et al. Halloysite nanotubes for efficient loading, stabilization and controlled release of insulin. *J Colloid Interface Sci.* 2018;524:156–164.
- [59] Lee Y, Jung G-E, Cho SJ, et al. Cellular interactions of doxorubicin-loaded DNA-modified halloysite nanotubes. *Nanoscale.* 2013;5(18):8577–8585.
- [60] Wu H, Shi Y, Huang C, et al. Multifunctional nanocarrier based on clay nanotubes for efficient intracellular siRNA delivery and gene silencing. *J Biomater Appl.* 2014;28(8):1180–1189.
- [61] Long Z, Zhang J, Shen Y, et al. Polyethyleneimine grafted short halloysite nanotubes for gene delivery. *Mater Sci Eng C Mater Biol Appl.* 2017;81:224–235.

- [62] Long Z, Wu Y-P, Gao H-Y, et al. Functionalization of halloysite nanotubes via grafting of dendrimer for efficient intracellular delivery of siRNA. *Bioconjugate Chem.* 2015.
- [63] Cavallaro G, Lazzara G, Massaro M, et al. Biocompatible poly (N-isopropylacrylamide)-halloysite nanotubes for thermoresponsive curcumin release. *J Phys Chem C.* 2015 Apr 23;119(16):8944–8951.
- [64] Rao KM, Kumar A, Suneetha M, et al. pH and near-infrared active; chitosan-coated halloysite nanotubes loaded with curcumin-Au hybrid nanoparticles for cancer drug delivery. *Int J Biol Macromol.* 2018;112:119–125.
- [65] Kerdsakundee N, Li W, Martins JP, et al. Multifunctional Nanotube-Mucoadhesive Poly(methyl vinyl ether-co-maleic acid) @hydroxypropyl methylcellulose acetate succinate composite for site-specific oral drug delivery. *Adv Healthc Mater.* 2017;6:20.
- [66] Shemesh R, Krepker M, Natan M, et al. Novel LDPE/halloysite nanotube films with sustained carvacrol release for broad-spectrum antimicrobial activity. *Rsc Adv.* 2015;5 (106):87108–87117.
- [67] Vergaro V, Abdullayev E, Lvov YM, et al. Cytocompatibility and uptake of halloysite clay nanotubes. *Biomacromolecules.* 2010 Mar 08;11(3):820–826.
- [68] Long Z, Wu Y-P, Gao H-Y, et al. In vitro and in vivo toxicity evaluation of halloysite nanotubes. *J Mater Chem B.* 2018;6(44):7204–7216.
- [69] Tarasova E, Naumenko E, Rozhina E, et al. Cytocompatibility and uptake of polycations-modified halloysite clay nanotubes. *Appl Clay Sci.* 2019 Mar 01;169:21–30.
- [70] Wu K, Feng R, Jiao Y, et al. Effect of halloysite nanotubes on the structure and function of important multiple blood components. *Mater Sci Eng C Mater Biol Appl.* 2017 June 01;75:72–78.
- [71] Rong R, Zhang Y, Zhang Y, et al. Inhibition of inhaled halloysite nanotube toxicity by trehalose through enhanced autophagic clearance of p62. *Nanotoxicology.* 2019;1:1–15.
- [72] Wang X, Gong J, Rong R, et al. Halloysite nanotubes-induced Al accumulation and fibrotic response in lung of mice after 30-day repeated oral administration. *J Agric Food Chem.* 2018 Mar 21;66 (11):2925–2933.
- [73] Fakhrullina GI, Akhatova FS, Lvov YM, et al. Toxicity of halloysite clay nanotubes in vivo: a *Caenorhabditis elegans* study. *Environ Sci.* 2015;2(1):54–59.

- [74] Kryuchkova M, Danilushkina A, Lvov Y, et al. Evaluation of toxicity of nanoclays and graphene oxide in vivo: a *Paramecium caudatum* study. *Environ Sci.* 2016;3(2):442–452.
- [75] Saleh, M. Y., Prajapati, N., DeCoster, M. A., and Lvov, Y. (2020). Tagged Halloysite Nanotubes as a Carrier for Intercellular Delivery in Brain Microvascular Endothelium. *Front. Bioeng. Biotechnol.* 8. doi:10.3389/fbioe.2020.00451.
- [76] Saleh, M., Prajapati, N., Karan, A. et al. Halloysite Nanotube Vehicles for Drug Delivery Through a Model Blood–Brain Barrier. *Clays Clay Miner.* (2022).
- [77] Silva, G. (2008). Nanotechnology approaches to crossing the blood-brain barrier and drug delivery to the CNS. *BMC Neurosci.* 9:S4. doi: 10.1186/1471-2202-9-S3-S4.
- [78] Bennewitz, M., and Saltzman, W. (2009). Nanotechnology for delivery of drugs to the brain for epilepsy. *Neurotherapeutics* 6, 323–336. doi: 10.1016/j.nurt.2009.01.018.
- [79] Bozdağ Pehlivan, S. (2013). Nanotechnology-based drug delivery systems for targeting imaging and diagnosis of neurodegenerative diseases. *Pharmaceutical Research*, 30(10), 2499–2511. <https://doi.org/10.1007/s11095-013-1156-7>.
- [80] World Health Organization [WHO] (2020). Epilepsy. Geneva: World Health Organization. Available online at: <https://www.who.int/news-room/fact-sheets/detail/epilepsy>.
- [81] Mahringer, A., Ott, M., and Fricker, G. (2013). “The blood–brain barrier: an introduction to its structure and function,” in *The Blood Brain Barrier*, Vol. 10, eds G. Fricker, M. Ott, and A. Mahringer (Berlin: Springer), 1–20. doi: 10.1177/0333102418786261.
- [82] Morgan, A. J., and Jacob, R. (1994). Ionomycin enhances Ca²⁺ influx by stimulating store-regulated cation entry and not by a direct action at the plasma membrane. *Biochem. J.* 300, 665–672. doi: 10.1042/bj3000665.
- [83] Wu, Y.-P., Yang, J., Gao, H.-Y., Shen, Y., Jiang, L., Zhou, C., et al. (2018). Folate-conjugated halloysite nanotubes, an efficient drug carrier, deliver doxorubicin for targeted therapy of breast cancer. *ACS Appl. Nano Mater.* 1, 595–608.
- [84] Kaushik, V., Yakisich, J., Kumar, A., Azad, N., and Iyer, A. (2018). Ionophores: potential use as anticancer drugs and chemosensitizers. *Cancers* 10:360. doi: 10.3390/cancers10100360.
- [85] Liu, M., Fakhrullin, R., Novikov, A., Vinokurov, V., Panchal, A., Fu, Y., et al. (2019). Tubule nanoclay-organic heterostructures for biomedical applications. *Macromol. Biosci.* 19:1800419. doi: 10.1002/mabi.201800419.

- [86] Prajapati, N., & DeCoster, M. (2020). Nitric oxide modulation and calcium dysregulation in brain endothelial and astrocyte cell co-cultures during inflammation. *Biomedical Sciences Instrumentation*, 56, 24–27.
- [87] Prajapati, N., Karan, A., Khezerlou, E., & DeCoster, M. A. (2021). The immunomodulatory potential of copper and silver based self-assembled metal organic biohybrids nanomaterials in cancer theranostics. *Frontiers in Chemistry*, 8, 1296. <https://doi.org/10.3389/fchem.2020.629835>.
- [88] Rodrigues, J. P., Prajapati, N., DeCoster, M. A., Poh, S., & Murray, T. A. (2021). Efficient LRP1-mediated uptake and low cytotoxicity of peptide L57 in vitro shows its promise as CNS drug delivery vector. *Journal of Pharmaceutical Sciences*, 110(2), 824–832. <https://doi.org/10.1016/j.xphs.2020.09.019>.
- [89] Vivès, E., Schmidt, J., & Pèlegri, A. (2008). Cell-penetrating and cell-targeting peptides in drug delivery. *Biochimica et Biophysica Acta (BBA) - Reviews on Cancer*, 1786(2), 126–138. <https://doi.org/10.1016/j.bbcan.2008.03.001>.
- [90] Artursson, P. (1991). Cell cultures as models for drug absorption across the intestinal mucosa. *Critical Reviews in Therapeutic Drug Carrier Systems*, 8(4), 305–330.
- [91] Artursson, P., Palm, K., & Luthman, K. (2001). Caco-2 monolayers in experimental and theoretical predictions of drug transport. *Advanced Drug Delivery Reviews*, 46(1–3), 27–43. 10.1016/S0169-409X(00)00128-9 (The article was published originally in *Advanced Drug Delivery Reviews*, 22, (1996), 67–84.).
- [92] Hubatsch, I., Ragnarsson, E., & Artursson, P. (2007). Determination of drug permeability and prediction of drug absorption in Caco-2 monolayers. *Nature Protocols*, 2, 2111–2119. <https://doi.org/10.1038/nprot.2007.303>.
- [93] Stenberg, P., Norinder, U., Luthman, K., & Artursson, P. (2001). Experimental and computational screening models for the prediction of intestinal drug absorption. *Journal of Medicinal Chemistry*, 44(12), 1927–1937. <https://doi.org/10.1021/jm001101a>.
- [94] Thiel, V., and Audus, K. (2001). Nitric oxide and blood–brain barrier integrity. *Antioxid. Redox Signal.* 3, 273–278.
- [95] Wang, G., Qian, P., Xu, Z., Zhang, J., Wang, Y., Cheng, S., et al. (2012). Regulatory effects of the JAK3/STAT1 pathway on the release of secreted phospholipase A2-IIA in microvascular endothelial cells of the injured brain. *J. Neuroinflammation* 9:170. doi: 10.1186/1742-2094-9-170.
- [96] Mbagwu, S., and Filgueira, L. (2020). Differential expression of CD31 and von willebrand factor on endothelial cells in different regions of the human brain: potential implications for cerebral malaria pathogenesis. *Brain Sci.* 10:31. doi: 10.3390/brainsci10010031.

- [97] Yamamoto, K., Furuya, K., Nakamura, M., Kobatake, E., Sokabe, M., and Ando, J. (2011). Visualization of flow-induced ATP release and triggering of Ca²⁺ waves at caveolae in vascular endothelial cells. *J. Cell Sci.* 124, 3477–3483. doi: 10.1242/jcs.087221.
- [98] Vivès, E., Brodin, P., & Lebleu, B. (1997). A truncated HIV-1 tat protein basic domain rapidly translocates through the plasma membrane and accumulates in the cell nucleus. *Journal of Biological Chemistry*, 272(25), 16010–16017. <https://doi.org/10.1074/jbc.272.25.16010>.
- [99] Park, C., Hahm, E., Lee, J., Jung, K., Rhee, H., Yang, C., et al. (2005). Ionomycin downregulates β -catenin/Tcf signaling in colon cancer cell line. *Carcinogenesis* 26, 1929–1933. doi: 10.1093/carcin/bgi145.
- [100] MacLean, J., and Yuste, R. (2009). Imaging action potentials with calcium indicators. *Cold Spring Harb. Protoc.* 2009:pdb.prot5316. doi: 10.1101/pdb.prot5650.
- [101] THan, S., Tie, X., Meng, L., Wang, Y., and Wu, A. (2013). PMA and ionomycin induce glioblastoma cell death: activation-induced cell-death-like phenomena occur in glioma cells. *PLoS One* 8:e76717. doi: 10.1371/journal.pone.0076717.
- [102] Formica, M. L. *et al.* On a highway to the brain: A review on nose-to-brain drug delivery using nanoparticles. *Appl. Mater. Today* **29**, 101631 (2022).
- [103] Persano, F. *et al.* Recent advances in the design of inorganic and nano-clay particles for the treatment of brain disorders. *J. Mater. Chem. B* **9**, 2756–2784 (2021).
- [104] Agrawal, M. *et al.* Recent strategies and advances in the fabrication of nano lipid carriers and their application towards brain targeting. *J. Control. Release* **321**, 372–415 (2020).
- [105] Jitendra, Sharma, P. K., Bansal, S. & Banik, A. Noninvasive Routes of Proteins and Peptides Drug Delivery. *Indian J. Pharm. Sci.* **73**, 367 (2011).
- [106] Turner, P. V, Brabb, T., Pekow, C. & Vasbinder, M. A. Administration of Substances to Laboratory Animals: Routes of Administration and Factors to Consider.
- [107] Dhuria, S. V., Hanson, L. R. & Frey, W. H. Intranasal delivery to the central nervous system: mechanisms and experimental considerations. *J. Pharm. Sci.* **99**, 1654–1673 (2010)v.
- [108] Erdő, F., Bors, L. A., Farkas, D., Bajza, Á. & Gizurarson, S. Evaluation of intranasal delivery route of drug administration for brain targeting. *Brain Res. Bull.* **143**, 155–170 (2018).

- [109] Maggio, E. T. Intravital: highly effective intranasal delivery of peptide and protein drugs. *Expert Opin. Drug Deliv.* **3**, 529–539 (2006).
- [110] Yang, J. *et al.* Enhanced Therapeutic Efficacy of Doxorubicin for Breast Cancer Using Chitosan Oligosaccharide-Modified Halloysite Nanotubes. *ACS Appl. Mater. Interfaces* **8**, 26578–26590 (2016).
- [111] Wen, J., Huang, Y., Crowe, T. P. & Hsu, W. H. Evaluation of Recent Intranasal Drug Delivery Systems to the Central Nervous System. *Pharm. 2022, Vol. 14, Page 629* **14**, 629 (2022).
- [112] Li, W. *et al.* Microfluidic assembly of a nano-in-micro dual drug delivery platform composed of halloysite nanotubes and a pH-responsive polymer for colon cancer therapy. *Acta Biomater.* **48**, 238–246 (2017).
- [113] Zhang, X. *et al.* Poly(l-lactide)/halloysite nanotube electrospun mats as dual-drug delivery systems and their therapeutic efficacy in infected full-thickness burns. <http://dx.doi.org/10.1177/0885328215593837> **30**, 512–525 (2015).
- [114] Pádua-Reis, M., Nôga, D. A., Tort, A. B. L. & Blunder, M. Diazepam causes sedative rather than anxiolytic effects in C57BL/6J mice. *Sci. Rep.* **11**, 9335–9335 (2021).
- [115] Diazepam: 7 things you should know - *Drugs.com*.
<https://www.drugs.com/tips/diazepam-patient-tips>.
- [116] Ruiz-Colón, K., Chavez-Arias, C., Díaz-Alcalá, J. E. & Martínez, M. A. Xylazine intoxication in humans and its importance as an emerging adulterant in abused drugs: A comprehensive review of the literature. *Forensic Sci. Int.* **240**, 1–8 (2014).